MODELING AND CONTROL OF A THERMALLY DRIVEN MEMS ACTUATOR FOR RF APPLICATIONS

by

Shahabeddin Vamegh Estahbanati

A Thesis Presented to the Faculty of the
American University of Sharjah
College of Engineering
in Partial Fulfillment
of the Requirements
for the Degree of

Master of Science in
Electrical Engineering

Sharjah, United Arab Emirates

May 2017

Approval Signatures

We, the undersigned, approve the Master's Thesis of Shahabeddin Vamegh Estahbanati.

Thesis Title: Modeling and Control of a Thermally Driven MEMS Actuator for RF Applications.

Signature	**Date of Signature** (dd/mm/yyyy)
_____	_____
Dr. Rached Dhaouadi Professor, Department of Electrical Engineering Thesis Advisor	
_____	_____
Dr. Maher Bakri-Kassem Assistant Professor, Department of Electrical Engineering Thesis Co-Advisor	
_____	_____
Dr. Shayok Mukhopadhyay Assistant Professor, Department of Electrical Engineering Thesis Committee Member	
_____	_____
Dr. Jin-Hyuk Lee Assistant Professor, Department of Mechanical Engineering Thesis Committee Member	
_____	_____
Dr. Nasser Qaddoumi Head, Department of Electrical Engineering	
_____	_____
Dr. Ghaleb Husseini Associate Dean for Graduate Affairs and Research, College of Engineering	
_____	_____
Dr. Richard Schoephoerster Dean, College of Engineering	
_____	_____
Dr. Mohamed El-Tarhuni Vice Provost for Graduate Studies	

Acknowledgements

First of all, I would like to thank Allah for blessing me with this opportunity to do my Master's degree. I take this opportunity to thank my family for their ongoing support and prayers.

I would also like to express my gratitude to my thesis advisors, Prof. Rached Dhaouadi and Dr. Maher Bakri-Kassem, for their guidance and support to complete this thesis. Furthermore, it is an honor to thank the College of Engineering at the American University of Sharjah, and the Head of Department of Electrical Engineering, Prof. Nasser Qaddoumi, for granting me the graduate assistantship to pursue my Master's degree.

Finally, I would like to extend sincere thanks to my older sister, Monirosharieh, who granted me access to research resources that enriched my thesis and paved the way for better research results.

And I start this thesis in the name of Allah, the Gracious, the Merciful...

...يَا أَيُّهَا الْعَزِيزُ

مَسَّنَا وَأَهْلَنَا الضُّرُّ وَجِئْنَا بِبِضَاعَةٍ مُزْجَاةٍ فَأَوْفِ لَنَا الْكَيْلَ وَتَصَدَّقْ عَلَيْنَا إِنَّ اللَّهَ يَجْزِي الْمُتَصَدِّقِينَ

يُوسُف ٨٨

…O exalted one! Distress has seized us and our family: we have brought but scanty capital: so pay us full measure, and treat it as charity to us: for Allah doth reward the charitable.

Surah Yusuf (Joseph) Verse# 88

Abstract

Thermally driven V-shaped microelectromechanical systems (MEMS) actuators have been used extensively in different fields of MEMS including RF MEMS applications. For this reason, developing a dynamic model is of importance for understanding the MEMS actuator dynamic behavior and for improving its transient response. Obtaining such a model is challenging as multi-physics phenomena are involved in the actuation mechanism. The complexities involved in modeling can be reduced by using macro-modeling approaches. As such, a new mixed-level nonlinear electro-thermo-mechanical dynamic macromodel for a thermally driven V-shaped MEMS actuator is proposed. The proposed reduced-order macromodel is composed of a nonlinear circuit-level electro-thermal macromodel and a nonlinear system-level thermo-mechanical macromodel obtained by the application of the Galerkin method. The system dynamic behavior is successfully reproduced using the proposed macromodel. The results obtained by the macromodels are in good agreement with the finite element ANSYS simulations and are computationally less expensive by far. Furthermore, the experimental static tip displacements of the actuator for different actuation voltages are in very good agreement with steady-state values of the actuator's tip displacements obtained by the proposed macromodel, and the maximum error obtained is less than 9%. Furthermore, a first-order dynamic model, based on the ANSYS input voltage and output displacement data, is developed in order to describe the displacement transient response of the MEMS actuator. The results obtained from the first-order and the ANSYS models are in very good agreement. The electro-thermo-mechanical macromodel and the first-order model are then used in closed-loop form with conventional and adaptive proportional-integral-derivative (PID) algorithms to speed up the displacement transient response of the thermal MEMS actuator. Using SIMULINK, it is shown that the adaptive PID controller outperforms the conventional PID controller by meeting all the design requirements.

Keywords: ***MEMS actuators; macromodeling; Galerkin method; adaptive control.***

Table of Contents

List of Figures

List of Tables

Chapter 1: Introduction and Literature Review

Microelectromechanical Systems (MEMS) have the potential to benefit different fields of technology including communications, unmanned aerial vehicles (UAVs), and biomedicine. The key for having a smart MEMS technology is the ability to control these microsystems which enhances their performance and reliability. Therefore, accurate modeling of components in MEMS is of importance in order to achieve success in control. However, the modeling process of MEMS components is challenging as it is associated with multi-physics phenomena. This study attempts to employ different modeling techniques and simulations to develop a dynamic model for a thermally driven V-shaped MEMS actuator used in RF applications. The dynamic model is then used to improve the displacement transient response of the actuator.

The accurate modeling of thermal MEMS actuators (including the electrical, thermal, and mechanical mechanisms) presents a difficult problem. Numerous models have been proposed in the literature to represent either the general system dynamics or some aspects of nonlinear thermal and mechanical effects. For V-shaped thermal MEMS actuators, the majority of the reported electro-thermal models are static [1]. On the other hand, the proposed dynamic models are computationally expensive [2]. Furthermore, they do not take into account the temperature-dependency of the material properties [3]. Additionally, heat convection has been ignored in the majority of the proposed static and dynamic models for the V-shaped MEMS actuators. As for thermo-mechanical modeling, quasi-static models have been proposed for U-shaped and V- and Z-shaped thermal MEMS actuators. The proposed models are cascaded with dynamic electro-thermal models to find the dynamic displacement of the actuators [3, 4]. Moreover, system identification techniques, based on finite element simulation of asymmetric thermal MEMS actuators, have been investigated for determining a dynamic model [5], and an analytical static model has been developed for V-shaped thermal MEMS actuators [1].

Time-dependent finite element methods are usually computationally very intensive, especially if multi-physics phenomena are involved in a system. Hence, it is desirable to employ efficient methods for developing accurate reduced-order dynam-

ical models which can capture the same information contained in the original partial differential equations (PDE) yet in a form that can be employed for fast dynamical simulations in the context of a circuit- or system-level simulation environment. These reduced-order models are often referred to as macromodels [6, 7]. Macromodeling has been used to model the response of a pressure sensor through measuring the pull-in time of an electrostatically actuated microbeam by applying the Galerkin method [6]. The model takes into consideration the effects of nonlinear squeeze-film damping for different conditions. Furthermore, macromodeling of a fixed- fixed beam MEMS structure has been reported using the Karhunen-Loeve/Galerkin method for nonlinear structural dynamics and fluidic damping effect. On the other hand, the Arnoldi algorithm was implemented for linear electro-thermal effect [8]. Additionally, a Krylov subspace-based algorithm has been used to extract a reduced second-order model from the finite element model of a one-dimensional electrothermally actuated micromirror device [9] .

Another approach in macromodeling is lumped modeling with circuit elements. In this method, a small set of electric circuit elements are chosen to represent the behavior of devices. Actual devices, exist in a three-dimensional physical continuum, and their behavior is governed by multi-physics laws. However, through analysis, simplified device representations which are readily expressible with equivalent electric circuits can be extracted. Moreover, circuit analogies allow efficient modeling of the interaction between the electronic and the non-electronic components of MEMS [10]. Lumped modeling with circuit elements technique has been used to model the thermal response and the static tip angular rotation of bimorph thermal MEMS actuators [9, 11]. Further, the method has been used for dynamic modeling of the displacement exhibited by V-shaped thermal MEMS actuators [12–14].

The last part of this thesis focuses on improving the transient response of the thermal MEMS actuator. Employing feedback control for improving the transient response of thermally driven MEMS actuators has been studied in the literature [12, 14–16]. In particular, a lead controller as well as a proportional controller have been used to improve the transient response of a thermal MEMS actuator using piezoresistive sensing [12]. As reported, the MEMS actuator response time to step inputs was reduced from 800 μs to 230 μs with proportional control alone, and the system bandwidth was

increased from 500 Hz to 4 kHz. In addition, using the same sensing mechanism, an integral-lead controller has been used in order to achieve zero steady-state error in response to a constant input command [15]. Finally, a proportional-integral controller has been used with a thermal MEMS actuator actuating a positioner stage in a nanopositioner, and a high degree of positioning accuracy with good robustness with this type of controller has been reported [16].

This research, however, attempts to apply adaptive control techniques for the purpose of improving the thermal MEMS actuator's transient response. There are different varieties of adaptive control techniques, including but not limited to, model reference adaptive control (MRAC) [17–19], adaptive neural control [20–22], adaptive fuzzy control [23, 24], and adaptive PID control [19, 25, 26]. Among these techniques, self-tuning of PID controllers by adaptive interaction is simple and effective. It also does not require knowledge of the plant to be controlled [25, 26].

1.1. Contributions

This research makes the following contributions related to modeling and control of thermally driven V-shaped MEMS actuators:

- It uses lumped modeling with circuit elements technique to model the thermal transient behavior of V-shaped thermal MEMS actuators. The lumped model presented includes temperature-dependent material properties leading to a nonlinear electro-thermal model. In addition, the new model accounts for convection and conduction losses to have a better representation of the thermal dissipation mechanism.
- It applies the Galerkin method to obtain a reduced order macromodel for the transversal displacement of V-shaped thermal MEMS actuators which are originally described by a nonlinear fourth order PDE. As a result, the PDE is reduced to a system of nonlinear second order ordinary differential equations.
- It combines the nonlinear electro-thermal and the nonlinear thermo-mechanical macromodels to obtain a hybrid model for the transversal displacement of thermally driven MEMS actuators which accounts for electrical, thermal, and me-

chanical effects. The resulting dynamic model for thermal MEMS actuators is developed for the first time to the author's best of knowledge.

- It develops a first-order ordinary differential equation based on the dynamic voltage-displacement data obtained from ANSYS, to model the displacement transient response of the MEMS actuator.
- It employs conventional PID and adaptive PID controllers in order to improve the transient response of the thermal MEMS actuator through simulation using SIMULINK.

1.2. Thesis Organization

In chapter 2, basic concepts related to MEMS actuators are presented. Specifically, different actuation mechanism in MEMS and in RF MEMS switches are discussed. In addition, various geometries of thermal MEMS actuators are presented and compared. Finally, a static model for V-shaped thermal MEMS actuators is presented along with the theory of adaptive interaction. Chapter 3 illustrates the structure and characterization of the thermal MEMS actuator. Chapter 4 discusses the finite element model developed in ANSYS and the macromodeling approach. In chapter 5, the lumped-element electro-thermal macromodel is presented. Chapter 6 is devoted to the development of the thermo-mechanical macromodel. The first-order model, derivation and stability proof of the adaptive PID controller as well as the controller design are discussed in chapters 7, 8, and 9, respectively. A conclusion follows these chapters that ties the chapters together, summarizes the major contributions, and suggests further work.

Chapter 2: Background

2.1. Comparison of Actuation Mechanisms in MEMS

MEMS actuators have become a vital part of microelectromechanical systems. For instance, micromirror arrays employ mechanical motion to modulate the light intensity; accelerometers use electrostatic actuation for self-test, and in-package microaligners use thermal actuation to align optical fibers to semiconductor lasers [1, 27, 28]. As the need for different actuation mechanisms has grown, different types of MEMS actuators, including but not limited to electrostatic [29], electrothermal [30], and piezoelectric [31] have been designed, fabricated, and studied over the last years. Although electrostatic actuators are typically energy efficient, they often require high voltages to operate in air [32]. Moreover, it is difficult to build electrostatic actuators with both high force and large displacement [33]. On the other hand, thermal MEMS actuators operate at low voltages and exert large forces [27]. The drawbacks of thermal actuators, however, are the slow response time limited by the heating and cooling time constants and large power consumption [27]. Piezoelectric actuators also require large voltages to generate significant displacements, although they do not consume DC power [27].

2.1.1. Actuation mechanisms in RF MEMS switches. RF MEMS switches can be classified based on the actuation mechanisms implemented in such switches. These actuation mechanisms include electrostatic, thermal, and piezoelectric actuations. Easier implementation of the electrostatic actuation over its piezoelectric counterpart makes the former a better candidate. Electrostatic actuators exhibit good RF performance and are of compact size; however, they handle low RF power and suffer from self actuation. In contrast, thermally actuated RF MEMS switches handle higher RF power with no self actuation and can be fabricated using thick layers as opposed to the electrostatic switches which make them less sensitive toward thermal conditions imposed from surrounding environment [34].

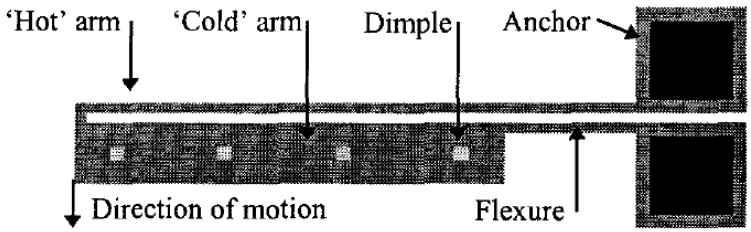

Figure 1: Asymmetric Thermal Micro-Actuator, (Courtesy of [30]).

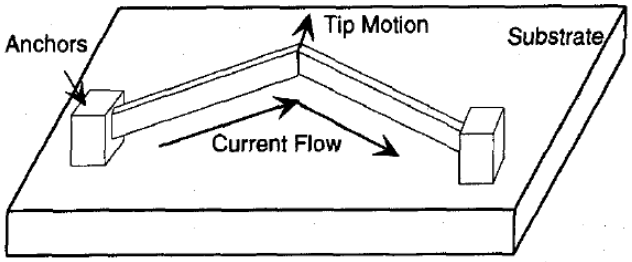

Figure 2: V-shaped Thermal Micro-Actuator, (Courtesy of [35]).

2.1.2. Geometries of thermal MEMS actuators. The following geometries for thermal MEMS actuators have been reported in the literature [27].

2.1.2.1. Asymmetric actuators. In this type of MEMS actuator shown in Fig. (1), current is passed through the actuator through the anchors. As the hot arm is narrower in comparison with the cold arm, higher current density is generated in the hot arm. As a result, it expands more than the wider cold arm [30].

2.1.2.2. V-shaped/chevron shaped actuators. Fig. (2) shows that when an electric current is passed through a V-shaped beam anchored at the two ends, joule heating results in thermal expansion of the beams, pushing the apex outward. The displacement of the apex is a function of the beam slope and dimensions. In addition, the force produced at the apex is linearly proportional to the displacement [35]. In this type of MEMS actuators, connecting the beams in a V-shaped structure leads to the amplification of the displacement [27].

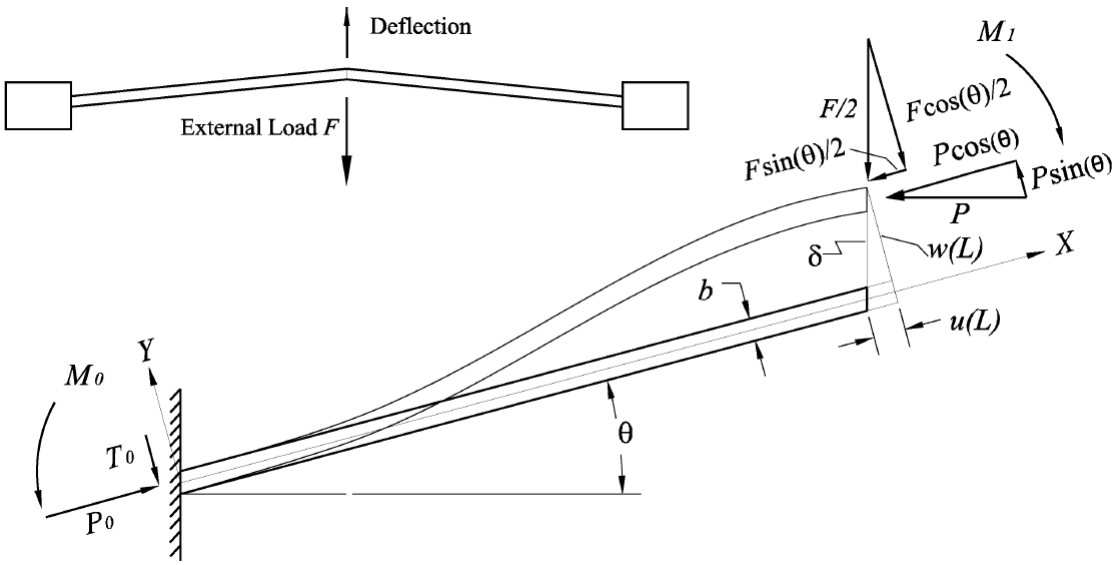

Figure 3: Geometry for half-span of a V-shaped MEMS actuator, (Courtesy of [1]).

2.1.2.3. Bi-morph actuators. Two materials of different thermal expansion coefficients are used which leads to bending of the structure upon heating [27]. This geometry has been reported in [36].

2.1.3. Comparison of geometries of thermal MEMS actuators. V-shaped MEMS actuators have distinguished advantages over other geometries in that they exhibit rectilinear motion and allow stacking [1].

2.2. Static Model for V-Shaped Thermal MEMS Actuators

The static model proposed in [1] uses the beam-column theory to model the transversal displacement of V-shaped thermal MEMS actuators. Fig. (3) depicts the geometry for half-span of a V-shaped MEMS actuator. As shown in the figure, the reaction forces replace the action of the missing half. Using geometric symmetry, force, and moment equilibrium conditions, the reaction forces acting at the anchor of the beam can be expressed as

$$\begin{aligned} P_0 &= P cos\theta + \frac{F}{2} sin\theta \\ T_0 &= P sin\theta + \frac{F}{2} cos\theta \\ M_0 &= M_1 - w(L)P_0 - LT_0 \end{aligned} \tag{1}$$

where F is the vertical load applied to the actuator, P and M_1 are the horizontal force and moment, respectively, transmitted from the missing half of the actuator.

The initial angle of the beam is θ, its half-length is L , and the transversal deflection of the mid cross section is $w(L)$. Assuming that the deformed shape of the beam can be described by a longitudinal displacement and transversal displacement , the average strain is given by

$$\varepsilon_x^0 = \frac{du}{dx} + \frac{1}{2}\left(\frac{dw}{dx}\right)^2 \tag{2}$$

Applying the beam-column theory with the addition of the thermal strain results in the following set of differential equations for $u(x)$ and $w(x)$

$$EA(\varepsilon_x^0 - \alpha(T(x) - T_0)) = -P_0 \tag{3}$$

$$EI\frac{d^2w}{dx^2} + P_0 w = -T_0 x - M_0 \tag{4}$$

where E is the Young's modulus, A is the cross-sectional area, α is the coefficient of thermal expansion, $T(x)$ is the local temperature, T_0 is the substrate temperature, and I is the second-order moment. Eqs. (3) and (4) require three boundary conditions. Since the internal force P and the reaction moment M_0 are not known, two additional boundary conditions are required for solving the problem. The boundary conditions are given as

$$w(0) = 0 \tag{5}$$

$$\frac{dw}{dx} = 0 \tag{6}$$

$$\frac{dw}{dx}(L) = 0 \tag{7}$$

$$u(0) = 0 \tag{8}$$

$$u(L) = \omega(L)\tan\theta \tag{9}$$

Integrating Eq. (3) along L and applying boundary conditions (8)-(9) gives

$$w(L)\tan\theta + \frac{1}{2}\int_0^L \left(\frac{dw}{dx}\right)^2 \mathrm{d}x - \alpha\bar{T}L = -\frac{P_0 L}{EA} \tag{10}$$

where $\bar{T} = \frac{1}{L}\int_0^L (T(x) - T_0)\,\mathrm{d}x$ is the average temperature increase of the beam.
Solving Eq. (4) with (5)-(6) gives

$$w(x) = \left(\tan\theta - \frac{F}{2k^2 EI\cos\theta}\right)\left[\frac{1}{k}\sin(kx) + \frac{(\cos(kL)-1)(\cos(kx)-1)}{k\sin(kL)} - x\right] \quad (11)$$

where $k = \sqrt{P_0/EI}$.
Upon substituting (11) into (10) and evaluating the integration, a transcendental equation containing F, $\bar{T}$, and the unknown eigenvalue k is obtained

$$c(k, F, \bar{T}) = 0 \quad (12)$$

where

$$\begin{aligned} c(k,F,\bar{T}) = \frac{ILk^2}{A} - \alpha L\bar{T} - \frac{\sin(kL)(-2EI\sin(\theta)k^2+F)^2}{2E^2I^2k^5\cos^2(\theta)(\cos(kL)+1)} \\ + \frac{(-2EI\sin(\theta)k^2+F)^2(\sin(kL)+2kL+kL\cos(kL)}{16E^2I^2k^5\cos^2(kL/2)\cos^2(\theta)} \\ + \frac{\tan(\theta)(-2EI\sin(\theta)k^2+F)(2\cos(kL)+kL\sin(kL)-2)}{2EIk^3\sin(kL)\cos(\theta)} \end{aligned} \quad (13)$$

Thus, for each value of F and $\bar{T}$, Eq. (12) is used to solve for k numerically. The obtained value of k is then used to find the tip displacement δ as follows:

$$\delta = \frac{w(L)}{\cos\theta} = \frac{(-2EI\sin(\theta)k^2+F)(2\cos(kL)+kL\sin(kL)-2)}{2EIk^3\sin(kL)\cos^2\theta}. \quad (14)$$

2.3. Theory of Adaptive Interaction

The theory of adaptive interaction is based on the assumption that a complex system is composed of several subsystems called devices [25,37]. Let pre_c be the device whose output is conveyed by connection c and $post_c$ the device whose input depends on the signal conveyed by connection c, the sets of input and ouput interactions for the n^{th} device are given by $\mathscr{I}_n = \{c : pre_c = n\}$ and $\mathscr{O}_n = \{c : post_c = n\}$, respectively. A system composed of three devices is shown in Fig. (4). In the figure, for example, the set of input interactions of Device 3 is $\mathscr{I}_3 = \{c_1, c_3\}$ and the set of output interactions

is $\mathscr{O}_3 = \{c_4\}$. In addition, c_1 connects Device 1 to Device 3. Thus, $pre_{c_1} = 1$ and $post_{c_1} = 3$.

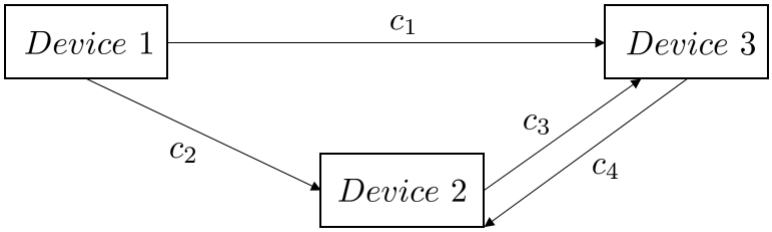

Figure 4: Illustration of devices and interactions.

The dynamics of each device (indexed by $n \in \mathscr{N} := \{1,2,\ldots,\mathscr{N}\}$) are given by a functional, which is a transformation from a vector space X into the space of real (or complex) scalars [38]. The functional for device n is denoted by $F_n : x_n \longrightarrow y_n$, $n \in \mathscr{N}$, where x_n and y_n denote the input and output spaces, respectively. In other words, the output of each device is a function of each input, which is in turn related to the outputs of other devices. Furthermore, it is assumed that the input to a device is a linear combination of the output of the other devices via connections in $\mathscr{I}_n$ and possibly an external signal $u_n(t)$ described by $x_n(t) = u_n(t) + \sum_{c\in\mathscr{I}_n} \eta_c y_{pre_c}(t)$, $n \in \mathscr{N}$, where y_{pre_c} is the output of another device whose output is conveyed by connection c, and η_c is a connection weight. With this linear interaction, the dynamics of the system can be described by $y_n(t) = \mathscr{F}_n[u_n(t) + \sum_{c\in\mathscr{I}_n} \eta_c y_{pre_c}(t)]$, $n \in \mathscr{N}$. The target is to find the correct η_c so that some performance index $\mathscr{E}(y_1,\ldots,y_n,u_1,\ldots,u_n)$ is minimized. The algorithm is given in the following theorem [25, 37].

Theorem 1 *Given the following dynamics for a system*

$$y_n(t) = \mathscr{F}_n[u_n(t) + \textstyle\sum_{c\in\mathscr{I}_n} \eta_c y_{pre_c}(t)], \quad n \in \mathscr{N}$$

if the connection weights η_c are adapted using

$$\frac{d\eta_c}{dt} = \left(\sum_{s\in\mathscr{O}_{post_c}} \eta_s \frac{d\eta_s}{dt} \frac{\frac{d\mathscr{E}}{dy_{post_s}} \circ \mathscr{F}'_{post_s}[x_{post_s}]}{\frac{d\mathscr{E}}{dy_{post_s}} \circ \mathscr{F}'_{post_s}[x_{post_s}] \circ y_{post_c}} - \sigma \frac{\partial \mathscr{E}}{\partial y_{post_c}} \right) \circ \mathscr{F}'_{post_c}[x_{post_c}] \circ y_{pre_c}, \; c \in \mathscr{C}$$

and the above equation has a unique solution, then the performance index $\mathscr{E}$ will decrease monotonically with time. In fact, the following is always satisfied

$$\frac{d\eta_c}{dt} = -\sigma \frac{d\mathscr{E}}{d\eta_c},\ c \in \mathscr{C}$$

where $\sigma > 0$ *is some adaptation coefficient.*

In addition, $\circ$ denotes composition, i.e.

$$y_n(t) = (\mathscr{F}_n \circ x_n)(t) = \mathscr{F}_n[x_n(t)],\ n \in \mathscr{N} \tag{15}$$

and the Fréchet derivative $\mathscr{F}_n'$ of $\mathscr{F}_n$ is defined as a functional such that

$$\lim_{||h||\to 0} \frac{||\mathscr{F}_n[x+h] - \mathscr{F}_n[x] - \mathscr{F}_n'[x] \circ h||}{||h||} = 0. \tag{16}$$

The theorem can be applied to a very general class of systems. For instance, the theorem has been applied to adaptive PID control systems as well as neural networks as reported in [25, 37].

Chapter 3: The Metal-Based V-Shaped Thermal MEMS Actuator

3.1. Structure

Fig. (5) shows a schematic diagram of the metal-based V-shaped thermal MEMS actuator used in this thesis. The actuator is composed of two arrays of Nickel beams anchored to the substrate at one end and connected to the Nickel shuttle at the other end. The heat generated in the shuttle stems from the voltage applied to the DC beams connected to a polysilicon layer under the shuttle. The polysilicon resistance is placed between two Silicon nitride layers for electrical isolation. Upon application of a voltage, heat is generated in the polysilicon resistance and is transferred to the array of Nickel beams through the shuttle, and as a result the actuator moves in response to the expansion of the beams.

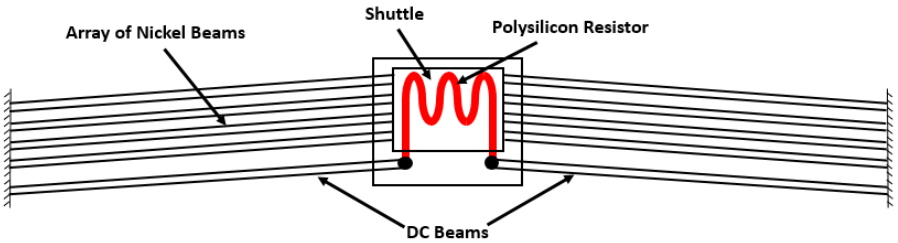

Figure 5: Schematic diagram of the MEMS actuator.

Fig. (6) shows the Scanning Electron Microscope (SEM) image of the metal-based V-Shaped thermal MEMS actuator used in our analysis. The MEMS actuator was fabricated using the MetalMUMPs process from MEMSCAP Inc. [34, 39, 40]. The comb structure is employed for visual position measurement. By applying 12 V, the actuator exhibits 35.7 μm displacement measured in standard ambient temperature and pressure (SATP).

3.2. Characterization

It is shown experimentally that Joule heating occurring across the polysilicon layer is a nonlinear phenomenon. In the first experiment, the equivalent resistance of

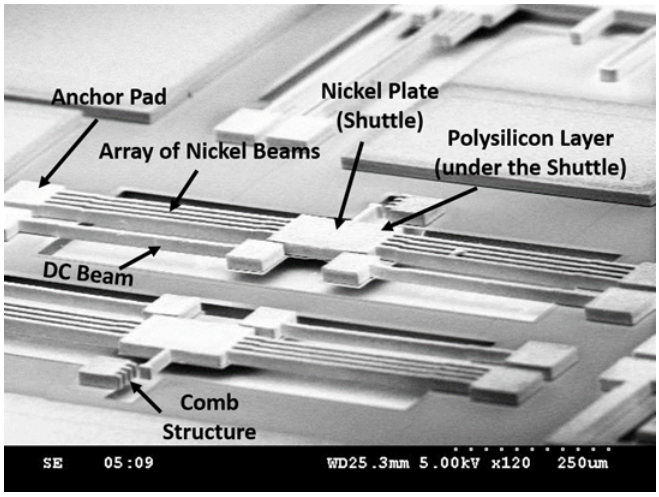

Figure 6: SEM image of two identical thermal V-shaped MEMS actuators.

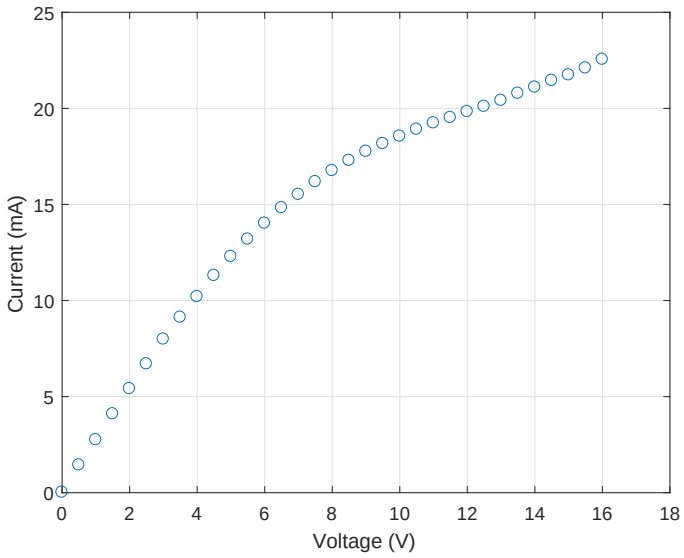

Figure 7: Experimental I-V data.

the polysilicon layer is found to be a function of temperature, resulting in a nonlinear current-voltage (I-V) characteristic as depicted in Fig. (7). The resistance of the polysilicon layer versus the actuation voltage is obtained from the data of Fig. (7). The obtained resistance-voltage data are plotted in Fig. (8). For modeling purposes, a fifth order polynomial is used to fit the resistance-voltage data:

$$R_p^e = 0.0009V^5 - 0.0473V^4 + 0.7846V^3 - 3.7937V^2 + 17.334V + 343.87 \qquad (17)$$

where V is the actuation voltage.

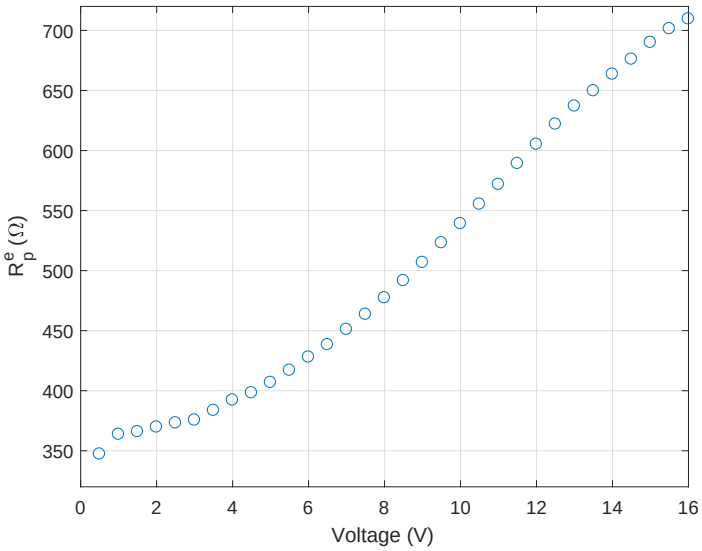

Figure 8: Polysilicon resistance as a function of voltage.

In the second experiment, the tip displacement of the actuator is measured in response to varying input voltages as shown in Fig. (9). As shown, the maximum tip displacement achieved corresponds to 16 V at which the actuator faced overheating destruction.

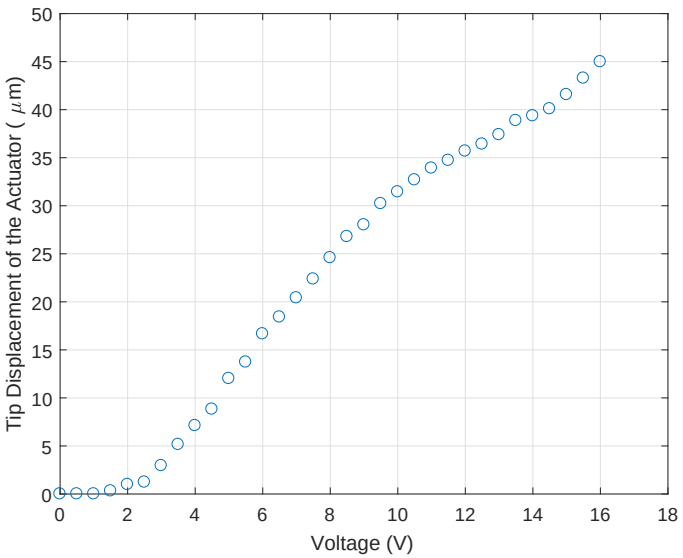

Figure 9: Measured tip displacement of the actuator for a varying input voltage.

In the third experiment, square wave signals of varying amplitudes, ranging from 1 V to 24 V, frequency of 10 Hz, and 50% duty cycle were applied to the MEMS

actuator. The overheating destruction occurred at 24 V. At this voltage, the maximum energy consumed by the MEMS actuator was 33.16 mJ, calculated from the product of the consumed power and the duration of the applied signal. The obtained value is the maximum energy that can be consumed by the MEMS actuator before overheating destruction occurs.

Chapter 4: Modeling the Thermally Driven V-Shaped MEMS Actuator

4.1. Finite Element Modeling Using ANSYS

A detailed finite element model (FEM) of the thermal MEMS actuator is developed using ANSYS Mechanical APDL with SOLID98 elements based on the structure given in Fig. (5). The model includes temperature-dependent data for the material properties as shown in Table 1. Additionally, the geometric nonlinearity option has been enabled and heat convection has been incorporated. The actuator model was then simulated in ANSYS. Simulations results showing the applied voltage, the obtained temperature, and the displacement solutions are illustrated in Figs. (10), (11), and (12), respectively. As seen in Fig. (10), the 12 V applied across the DC beams produces heat in the polysilicon layer under the shuttle. Fig. (11) depicts the temperature distribution in the actuator. It is evident that the shuttle which is placed on top of the polysilicon layer exhibits the highest temperature which is approximately 718 K. In addition, Fig. (12) represents the lateral displacement of the actuator shuttle from its initial position. The displacement obtained at the shuttle is 35.34 μm, which is within 1% of the experimental measurement.

Table 1: Temperature dependencies for material properties used in ANSYS.

Parameter	Symbol	Reference
Thermal Conductivity of Nickel	$\kappa_{Ni}(T)$	[41]
Thermal Conductivity of Air	$\kappa_{air}(T)$	[42]
Coefficient of Thermal Expansion of Nickel	$\alpha(T)$	[43]
Convection Coefficient of Air	$h(T)$	[44]

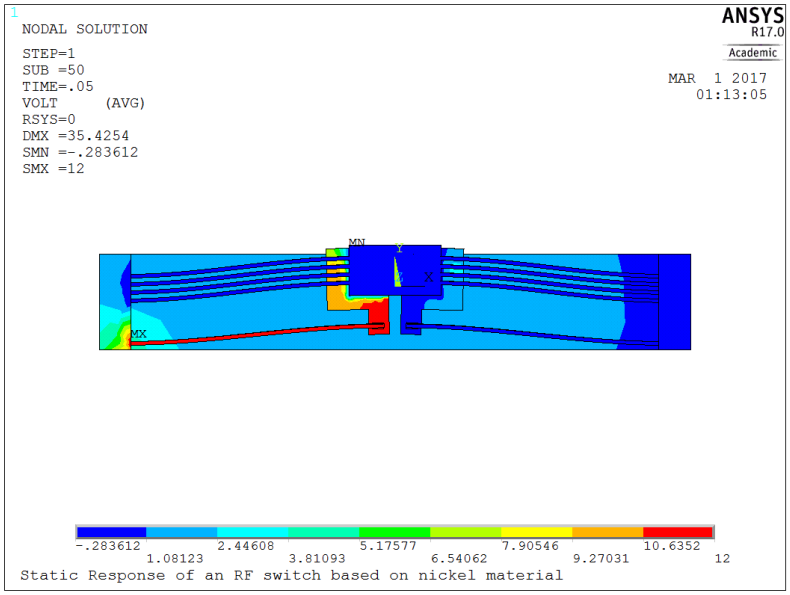

Figure 10: ANSYS simulation of voltage in the actuator.

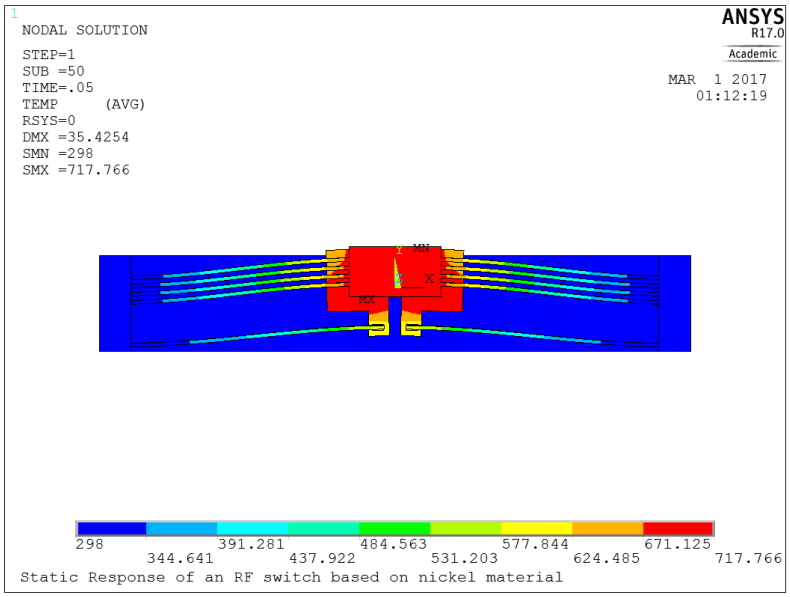

Figure 11: ANSYS Simulation of heat distribution in the actuator.

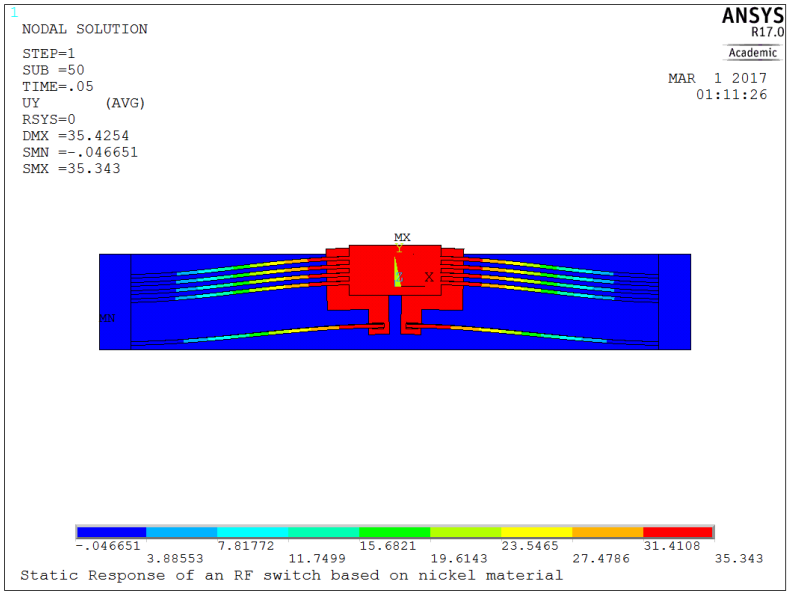

Figure 12: ANSYS simulation of actuator's displacement.

4.2. Macromodeling Approach

The macromodels are developed for the structure depicted in Fig. (5). The analysis is accomplished for a two-beam MEMS actuator first and then expanded to the eight-beam structure. The thermal MEMS actuator can be represented by an electro-thermal macromodel cascaded with a thermo-mechanical macromodel as shown in Fig. (13). The blocks are discussed in chapters 5 and 6, respectively.

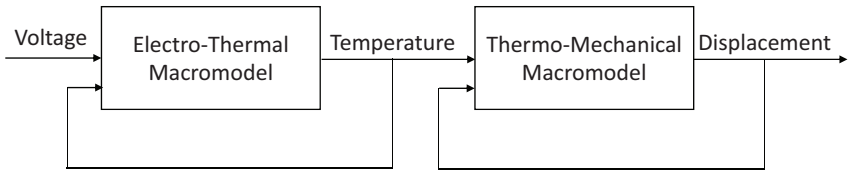

Figure 13: Electro-thermo-mechanical macromodel.

4.3. Black-Box Modeling Approach

In this approach, the displacement dynamic responses for different actuation voltages, obtained from the ANSYS model, are fed into the MATLAB System Identifi-

cation Toolbox in order to develop a dynamic model which relates the input voltage to the output displacement. The model's block diagram representation is depicted in Fig. (14). This approach is presented in chapter 7.

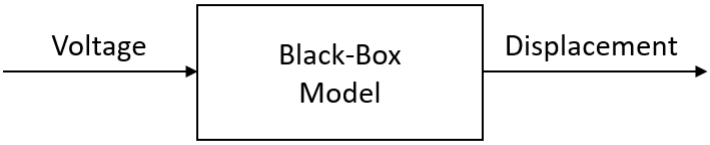

Figure 14: Black-box model.

Chapter 5: Electro-thermal modeling of V-Shaped Thermal MEMS Actuators

The electro-thermal macromodel is developed using an equivalent electric circuit with lumped elements. The temperature profiles in the shuttle and the beams can be obtained by dividing the actuator into three main volumes, namely the beams on the left of the shuttle, the beams on the right of the shuttle, and the shuttle. Each volume can then be represented by thermal capacitances, conduction thermal resistances, and convection thermal resistances [12, 13, 45]. In this research, each beam is divided into two segments by using four conduction resistances. Furthermore, the heat storage capability of the beams has been modeled using two heat capacitances. In addition, the heat losses to the substrate and to the air located on upper surface of the beams have been modeled using two conduction and two convection resistances, respectively. It is worth mentioning here that having more segments improves the accuracy of the model, but increases the model complexity. As for the shuttle, the heat losses have been modeled using one conduction and one convection resistances. Additionally, the heat generated in the shuttle is modeled using a current source, and the heat storage capability of the shuttle is represented by a thermal capacitance as reported in [13, 46]. It is important to note that the proposed model benefits from experimental data for the resistance of the polysilicon layer shown in Eq. (17), and employs temperature-dependent material properties for modeling the heat losses due to conduction and convection which leads to having nonlinear ordinary differential equations [46].

Fig. (15) shows the model proposed for a two-beam actuator. The electro-thermal circuit can be expanded to represent eight beams. It is worth noting that in all the equivalent circuit analysis, temperature is considered to be the across variable, and heat current is the through variable. Thus, the product between the through and across variables is not power, but a hybrid unit of Watt-Kelvins [10]. Moreover, it should be noted that in the proposed model, the heat conduction between adjacent beams of the same array has been ignored. The physical, thermal, and electrical parameters used for modeling are tabulated in Tables 2, 3, and 4 in which T denotes the temperature in the pertaining volume.

Table 2: Physical parameters.

Parameter	Symbol	Value	Reference	Units
Beam Length	l_b	480	-	μm
DC Beam Length	l_β	555	-	μm
Shuttle Length	l_s	200	-	μm
Nitride Length	l_N	324	-	μm
Beam Width	w_b	8	-	μm
DC Beam Width	w_β	8	-	μm
Shuttle Width	w_s	110	-	μm
Nitride Width	w_N	136	-	μm
Beam Thickness	t_b	20	-	μm
DC Beam Thickness	t_β	20	-	μm
Shuttle Thickness	t_s	20	-	μm
Nitride Thickness	t_N	0.35	-	μm
Trench Depth	g	25	-	μm
Nickel Density	ρ_{Ni}	8900	[41]	kg/m^3
Nitride Density	ρ_N	3440	[47]	kg/m^3

Table 3: Thermal parameters.

Parameter	Symbol	Value	Reference	Units
Ambient Temperature	T_0	298.15	-	K
Thermal Conductivity of Nickel	κ_{Ni}	Eq. (18)	-	$W/(m-K)$
Thermal Conductivity of Air	$\kappa_{air}(T)$	Eq. (19)	-	$W/(m-K)$
Specific Heat of Nickel	$c_{Ni}^{T_0}$	445	[41]	$J/(kg-K)$
Specific Heat of Nitride	$c_N^{T_0}$	170	[48]	$J/(kg-K)$
Convection Coefficient of Air	$h(T)$	Eq. (20)	-	$W/(m^2-K)$

Table 4: Electrical parameters.

Parameter	Symbol	Value/Expression	Units
DC Beams Resistance	R_β^e	0.2512	Ω
Polysilicon Resistance	$R_p^e(V)$	Eq. (17)	Ω
Actuation Voltage	V	Variable	Volts

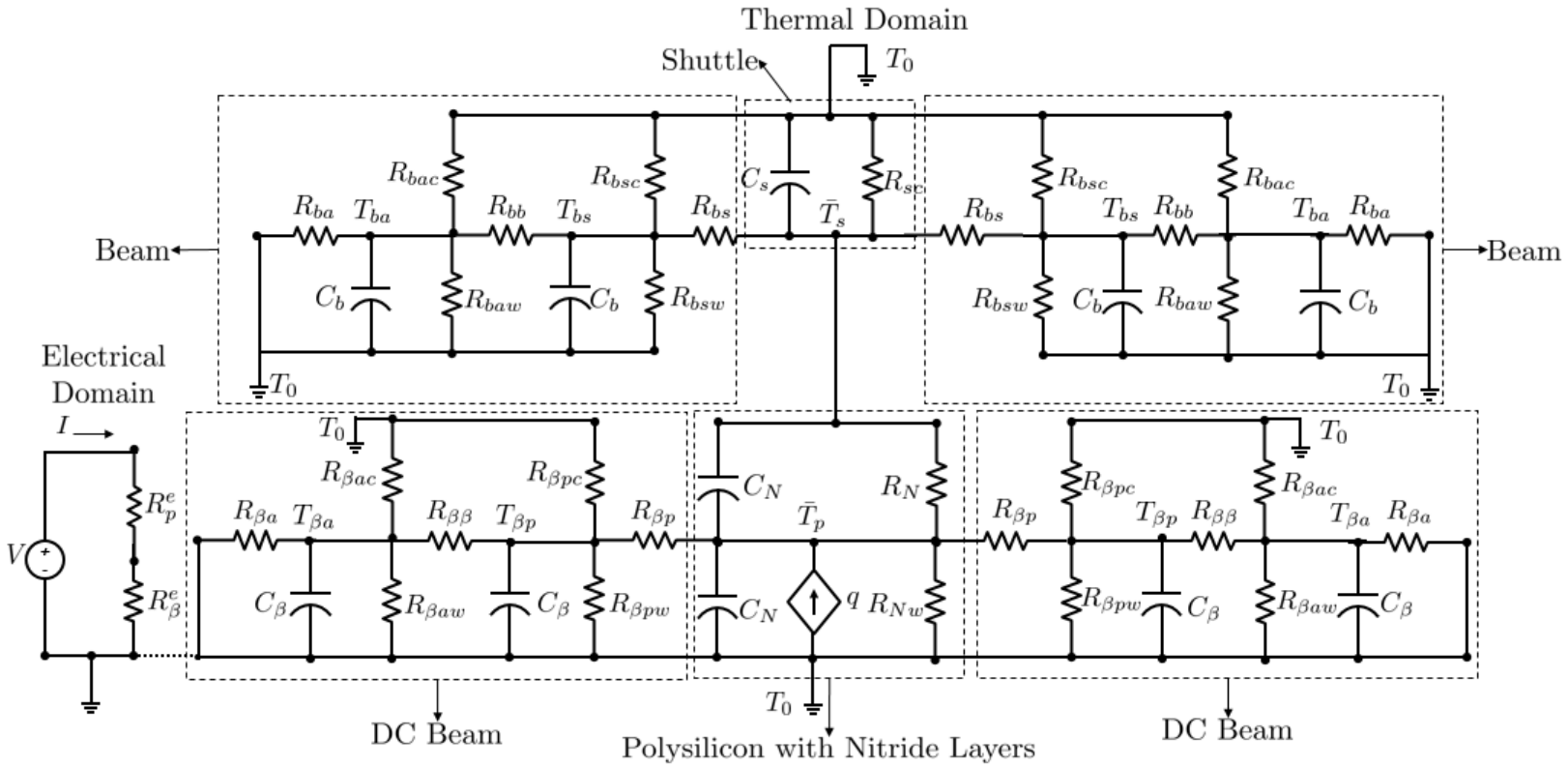

Figure 15: Proposed Electro-thermal lumped element model for a two-beam MEMS actuator.

As shown in Figs. (16), (17), and (18), κ_{Ni}, κ_{air}, and h vary with temperature. The data are fitted with appropriate polynomials in order to be used for improving the accuracy of the model. As such, the following polynomials were obtained:

$$\kappa_{Ni}(T) = 0.0001693T^2 - 0.2339T + 146.1 \tag{18}$$

$$\kappa_{air}(T) = -2 \times 10^{-8}T^2 + 8 \times 10^{-5}T + 0.004 \tag{19}$$

$$h(T) = 1.388T + 103.62 \tag{20}$$

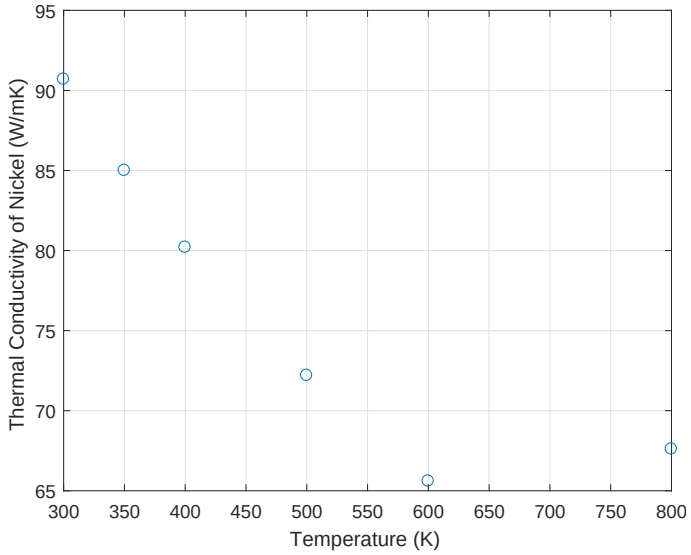

Figure 16: Thermal conductivity of Nickel as a function of temperature [41].

The model parameters are designed using Eqs. (21) through (45), and are listed in Table 5.

The following shape factors are used to approximate the heat transferred from the bottom and sides of the beams and the lower Nitride layer to their effective projected

area on the substrate [12]:

$$S_b = \left(\frac{t_b}{w_b}\right)\left(\frac{2g}{t_b}+1\right)+1 \tag{21}$$

$$S_\beta = \left(\frac{t_\beta}{w_\beta}\right)\left(\frac{2g}{t_\beta}+1\right)+1 \tag{22}$$

$$S_N = \left(\frac{t_N}{w_N}\right)\left(\frac{2g}{t_N}+1\right)+1. \tag{23}$$

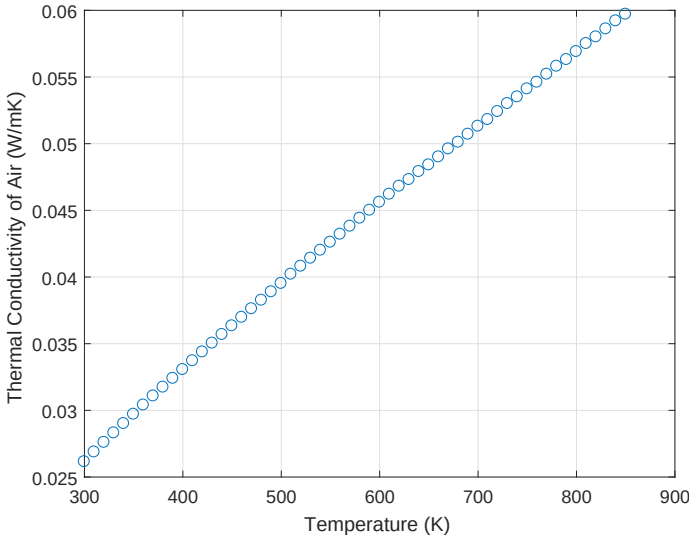

Figure 17: Thermal conductivity of air as a function of temperature [42].

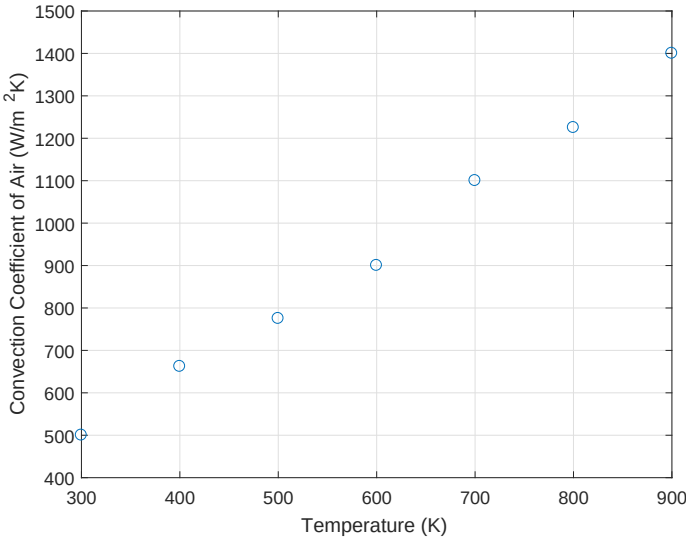

Figure 18: Convection Coefficient of air as a function of temperature [44].

Defining $l_{bh} = l_b/2$, the thermal resistances and capacitances of the beams are as follows:

$$R_{bs}(T) = \frac{l_{bh}}{2\kappa_{Ni}(T)w_b t_b} \tag{24}$$

$$R_{bb}(T) = R_{bs}(T) + R_{ba}(T) \tag{25}$$

$$R_{ba}(T) = \frac{l_{bh}}{2\kappa_{Ni}(T)w_b t_b} \tag{26}$$

$$R_{bsw}(T) = \frac{g}{\kappa_{air}(T)w_b l_{bh} S_b} \tag{27}$$

$$R_{baw}(T) = \frac{g}{\kappa_{air}(T)w_b l_{bh} S_b} \tag{28}$$

$$R_{bsc}(T) = \frac{1}{w_b l_{bh} h(T)} \tag{29}$$

$$R_{bac}(T) = \frac{1}{w_b l_{bh} h(T)} \tag{30}$$

$$C_b = w_b l_{bh} t_b \rho_{Ni} c_{Ni}. \tag{31}$$

Let $l_{\beta h} = l_\beta/2$, the thermal resistances and capacitances of the DC beams are defined by the following equations:

$$R_{\beta p}(T) = \frac{l_{\beta h}}{2\kappa_{Ni}(T)w_\beta t_\beta} \tag{32}$$

$$R_{\beta\beta}(T) = R_{\beta p}(T) + R_{\beta a}(T) \tag{33}$$

$$R_{\beta a}(T) = \frac{l_{\beta h}}{2\kappa_{Ni}(T)w_\beta t_\beta} \tag{34}$$

$$R_{\beta pw}(T) = \frac{g}{\kappa_{air}(T)w_\beta l_{\beta h} S_\beta} \tag{35}$$

$$R_{\beta aw}(T) = \frac{g}{\kappa_{air}(T)w_\beta l_{\beta h} S_\beta} \tag{36}$$

$$R_{\beta pc}(T) = \frac{1}{w_\beta l_{\beta h} h(T)} \tag{37}$$

$$R_{\beta ac}(T) = \frac{1}{w_\beta l_{\beta h} h(T)} \tag{38}$$

$$C_\beta = w_\beta l_{\beta h} t_\beta \rho_{Ni} c_{Ni}. \tag{39}$$

The thermal resistance and capacitance of the shuttle are defined by

$$R_{sc}(T) = \frac{1}{w_n l_n h(T)} \tag{40}$$

$$C_s = w_s l_s t_s \rho_{Ni} c_{Ni}. \tag{41}$$

The thermal resistances and capacitances of the Nitride layers are given by

$$R_N = \frac{t_N}{\kappa_N w_n l_n} \tag{42}$$

$$R_{Nw}(T) = R_N + \frac{g}{\kappa_{air}(T) w_n l_n S_N} \tag{43}$$

$$C_N = w_N l_N t_N \rho_N c_N. \tag{44}$$

Finally, the heat current (equivalent heat power) resulting from Joule heating is modeled as

$$q = \frac{V^2}{R_p^e(V) + R_\beta^e}. \tag{45}$$

As seen in Eq. (45), the heat current generated in the MEMS actuator is proportional to the voltage-squared. This implies that the polarity of the actuation voltage makes no difference in the heat generation process.

In what follows, the temperature dependency of the thermal resistances is not shown for simplicity.

Applying nodal analysis on the electro-thermal circuit of Fig. (15) gives the dynamic equations describing the temperature transients of the shuttle and the beams. The equations are generalized to account for N beams where N is the total number of

Table 5: Descriptions of the LEM parameters.

Volume Name	Parameter	Symbol
Beam-Shuttle	Average Temperature	$\bar{T}_{bs}$
	Half-Volume Conduction Thermal Resistance	R_{bs}
	Volume-Substrate Conduction Thermal Resistance	R_{bsw}
	Convection Thermal Resistance	R_{bsc}
	Thermal Capacitance	C_b
Beam-Anchor	Average Temperature	$\bar{T}_{ba}$
	Half-Volume Conduction Thermal Resistance	R_{ba}
	Volume-Substrate Conduction Thermal Resistance	R_{baw}
	Convection Thermal Resistance	R_{bac}
	Thermal Capacitance	C_b
DC Beam-Polysilicon	Average Temperature	$\bar{T}_{\beta s}$
	Half-Volume Conduction Thermal Resistance	$R_{\beta s}$
	Volume-Substrate Conduction Thermal Resistance	$R_{\beta sw}$
	Convection Thermal Resistance	$R_{\beta sc}$
	Thermal Capacitance	C_β
DC Beam-Anchor	Average Temperature	$\bar{T}_{\beta a}$
	Half-Volume Conduction Thermal Resistance	$R_{\beta a}$
	Volume-Substrate Conduction Thermal Resistance	$R_{\beta aw}$
	Convection Thermal Resistance	$R_{\beta ac}$
	Thermal Capacitance	C_β
Shuttle	Average Temperature	$\bar{T}_s$
	Convection Thermal Resistance	R_{sc}
	Thermal Capacitance	C_s
Silicon Nitride	Conduction Thermal Resistance	R_N
	Volume-Substrate Conduction Thermal Resistance	R_{Nw}
	Thermal Capacitance	C_N
Polysilicon	Average Temperature	$\bar{T}_p$
	Heat Current	q

beams in the actuator.

$$
\begin{aligned}
2C_N\frac{d\bar{T}_p}{dt} &= C_N\frac{d\bar{T}_s}{dt}+\left(\frac{1}{R_N}\right)\bar{T}_s+\left(\frac{2}{R_{\beta p}}\right)\bar{T}_{\beta p}-\left(\frac{2}{R_{\beta p}}+\frac{1}{R_{Nw}}+\frac{1}{R_N}\right)\bar{T}_p \\
&\quad+\left(\frac{1}{R_{Nw}}\right)T_0+q \\
C_\beta\frac{d\bar{T}_{\beta p}}{dt} &= \left(\frac{1}{R_{\beta\beta}}\right)\bar{T}_{\beta a}-\left(\frac{1}{R_{\beta\beta}}+\frac{1}{R_{\beta p}}+\frac{1}{R_{\beta pc}}+\frac{1}{R_{\beta pw}}\right)\bar{T}_{\beta p}+\left(\frac{1}{R_{\beta p}}\right)\bar{T}_p \\
&\quad+\left(\frac{1}{R_{\beta pc}}+\frac{1}{R_{\beta pw}}\right)T_0 \\
C_\beta\frac{d\bar{T}_{\beta a}}{dt} &= -\left(\frac{1}{R_{\beta\beta}}+\frac{1}{R_{\beta a}}+\frac{1}{R_{\beta ac}}+\frac{1}{R_{\beta aw}}\right)\bar{T}_{\beta a}+\left(\frac{1}{R_{\beta a}}+\frac{1}{R_{\beta ac}}+\frac{1}{R_{\beta aw}}\right)T_0 \\
&\quad+\left(\frac{1}{R_{\beta\beta}}\right)\bar{T}_{\beta p} \\
(C_s+C_N)\frac{d\bar{T}_s}{dt} &= C_N\frac{d\bar{T}_p}{dt}+\left(\frac{1}{R_N}\right)\bar{T}_p+\left(\frac{N}{R_{bs}}\right)\bar{T}_{bs}-\left(\frac{N}{R_{bs}}+\frac{1}{R_{sc}}+\frac{1}{R_N}\right)\bar{T}_s \\
&\quad+\left(\frac{1}{R_{sc}}\right)T_0 \\
C_b\frac{d\bar{T}_{bs}}{dt} &= \left(\frac{1}{R_{bb}}\right)\bar{T}_{ba}-\left(\frac{1}{R_{bb}}+\frac{1}{R_{bs}}+\frac{1}{R_{bsc}}+\frac{1}{R_{bsw}}\right)\bar{T}_{bs}+\left(\frac{1}{R_{bsc}}+\frac{1}{R_{bsw}}\right)T_0 \\
&\quad+\left(\frac{1}{R_{bs}}\right)\bar{T}_s \\
C_b\frac{d\bar{T}_{ba}}{dt} &= -\left(\frac{1}{R_{bb}}+\frac{1}{R_{ba}}+\frac{1}{R_{bac}}+\frac{1}{R_{baw}}\right)\bar{T}_{ba}+\left(\frac{1}{R_{ba}}+\frac{1}{R_{bac}}+\frac{1}{R_{baw}}\right)T_0 \\
&\quad+\left(\frac{1}{R_{bb}}\right)\bar{T}_{bs}
\end{aligned}
\tag{46}
$$

Eq. (46) describes the dynamics of the circuit where $\bar{T}_s$ represents the average shuttle temperature. Furthermore, since the beams are represented by four conduction resistances, $\bar{T}_{ba}$ and $\bar{T}_{bs}$ denote the temperatures at $l_b/4$ away from the anchor and the shuttle, respectively. Similarly, for the DC beams, $\bar{T}_{\beta a}$ and $\bar{T}_{\beta p}$ denote the temperatures at $l_b/4$ away from the anchor and the polysilicon, respectively. Assuming that the average temperature of the beams is located at the center of the beams, Eq. (47) can be used to find this average temperature as follows:

$$
\bar{T}_b = \frac{1}{2}(\bar{T}_{bs}+\bar{T}_{ba}). \tag{47}
$$

Eqs. (46)-(47) which form the lumped element model (LEM) are then modeled in SIMULINK to find the $\bar{T}_s(t)$ and $\bar{T}_b(t)$. The obtained variables are then compared with their counterparts obtained from the FEM. The simulation results obtained with the LEM and the FEM show the average temperatures in the shuttle $\bar{T}_s$ and the beams $\bar{T}_b$ for the eight-beam actuator for 50 milliseconds as depicted in Figs. (19a, 19b). As shown, the LEM exhibits a faster transient response in comparison with the FEM. At 12 V, the error is higher than at 6 V. We have investigated that by increasing the number of segments of the beams, the electro-thermal model becomes close to a distributed model rather than a lumped model, and therefore, the error associated with the transient response decreases. However, this is a trade-off between simplicity and accuracy of the LEM. Furthermore, the steady-state values of $\bar{T}_s$ and $\bar{T}_b$ obtained by the LEM and the FEM are tabulated in Tables 6 and 7, respectively. As seen, the maximum percentage difference for $\bar{T}_s$ and $\bar{T}_b$ is less than 9%. It is worth noting that the total time elapsed to run the ANSYS simulation was 90 minutes. However, the LEM simulation in SIMULINK was completed in less than 1 minute. Consequently, the obtained results show a very good agreement considering the difference in the computational cost incurred.

Finally, the plots of the thermal resistances as a function of time for 6 V and 12 V can be found in Appendix A.

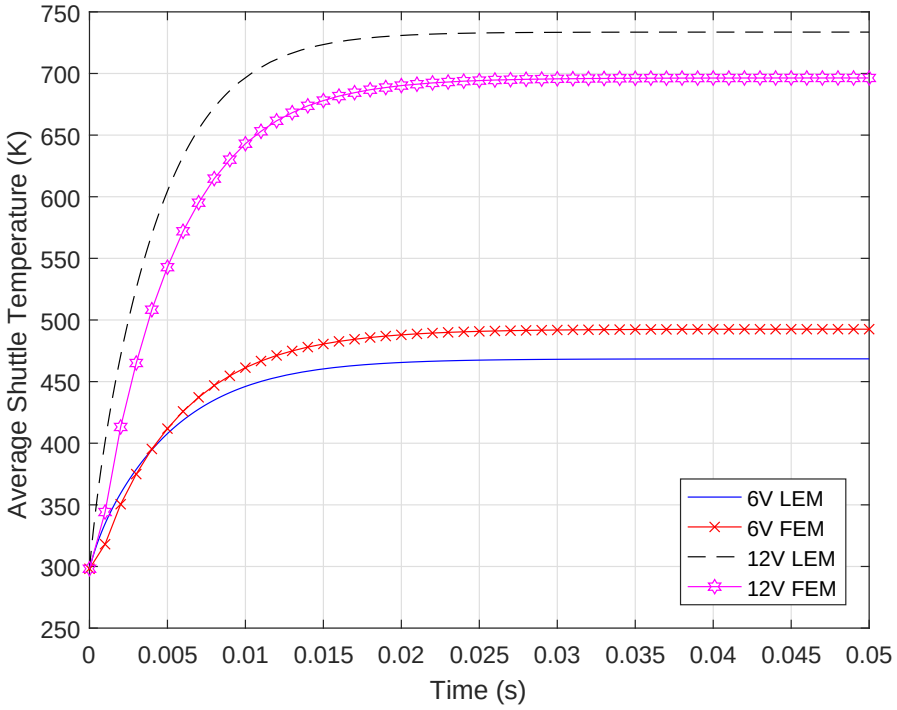

(a)

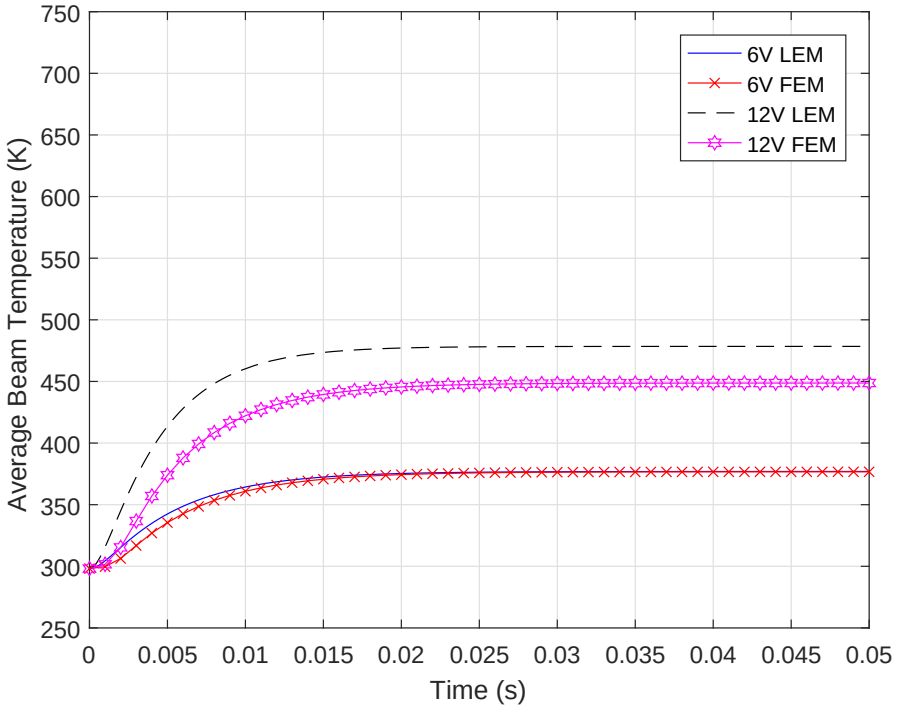

(b)

Figure 19: Simulated average temperatures of the eight-beam thermally driven MEMS Actuator for 6V and 12V input voltages in the (a) shuttle, (b) beams.

Table 6: Comparison of steady-state values of the average shuttle temperature for different actuation voltages.

Voltage (V)	LEM $\bar{T}_s$ (K)	FEM $\bar{T}_s$ (K)	Percent Difference (%)
6	468.46	492.54	5.01
8	559.63	577.30	3.11
10	647.92	648.99	0.17
12	733.59	696.38	5.20
14	821.37	755.59	8.34

Table 7: Comparison of steady-state values of the average beam temperature for different actuation voltages.

Voltage (V)	LEM $\bar{T}_b$ (K)	FEM $\bar{T}_b$ (K)	Percent Difference (%)
6	376.96	376.70	0.07
8	414.41	407.34	1.72
10	447.99	432.13	3.60
12	478.44	448.70	6.42
14	507.84	469.72	7.80

Chapter 6: Thermo-Mechanical Modeling of V-Shaped Thermal MEMS Actuators

In this chapter, we propose a dynamic model for the lateral displacement of a V-shaped thermal MEMS actuator. The authors in [1] have developed an analytical model for the static buckling of V-shaped thermal MEMS actuators with two beams. However, an analytical model for the dynamic buckling of V-shaped thermal actuators have not been studied in the literature. Therefore, we propose to use the Galerkin method to obtain a macromodel for the transversal displacement of thermally driven V-shaped MEMS actuators.

Fig. (20a) depicts the half-span of a V-shaped thermal actuator with lateral displacement $w(x,t)$ exhibited on the xy-coordinate and the beam and shuttle tip displacements denoted by $\delta_b(t)$ and $\delta_s(t)$ on the $\zeta\eta$-coordinate . The other half of the actuator is replaced by reaction forces [1]. Our approach is to divide the structure in Fig. (20a) into several beam elements as shown in Fig. (20b) and find the nodal displacements. Since the shuttle has a large mass in our actuator, it is required to be included in the model as it affects the mechanical transient considerably although the V-shaped MEMS actuators in the literature either do not have a shuttle or the shuttle has been ignored in the modeling process. In the following section, the dynamic formulation of the beam in Fig. (20a) is presented. The formulation is then used to model both the beam and the shuttle using two beam elements in Section 6.3.

6.1. Nonlinear Dynamic Buckling Model of V-Shaped MEMS Actuators with Thermal Strain

In order to develop a formulation for a general beam element in the next part, it is assumed that the half-span of the actuator has a uniform cross-section area (the shuttle does not exist). Therefore, the beam going under axial and lateral loading can be modeled using the Euler-Bernoulli beam approach given by Eq. (48) [46]

$$EI_b\frac{\partial^4 w(x,t)}{\partial x^4}+P(t)\frac{\partial^2 w(x,t)}{\partial x^2}+\rho_{Ni}A_b\frac{\partial^2 w(x,t)}{\partial t^2}=F(t)\in\mathbb{R} \tag{48}$$

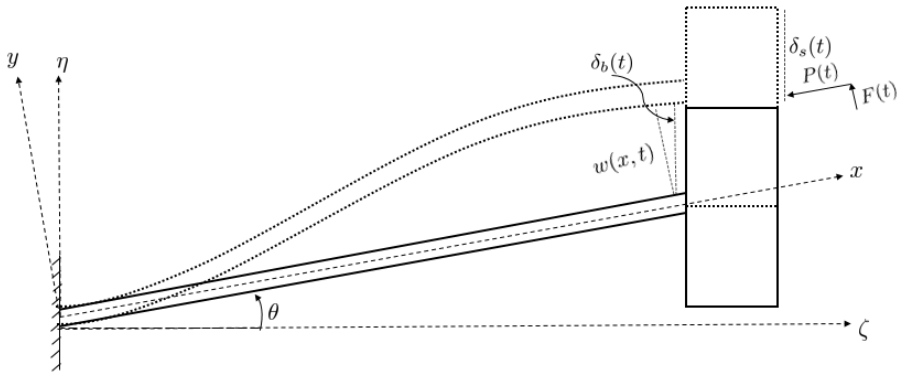

(a)

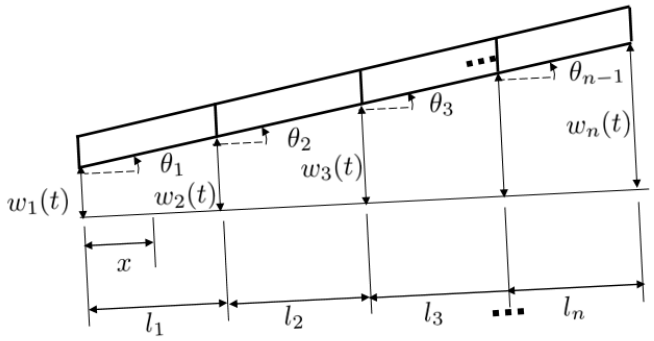

(b)

Figure 20: (a) Geometry of the beam and the shuttle in the MEMS actuator, (b) Discretized geometry with n beam elements.

where

$$F(t) = P(t)\tan\theta\,\delta(x-l_b), \tag{49}$$

E is the Young's modulus, I_b is the second-order moment of the beam, $P(t) \in \mathbb{R}$ is the axial force, A_b is the cross-section area of the beam, and $\delta(x-l_b)$ is the Dirac delta function used to show that $F(t)$ is a force at the tip of the beam [49] (i.e. $x = l_b$).
In addition, the total strain in the thermally induced beam can be obtained by summation of mechanical and thermal strains [49]. That is,

$$\varepsilon_{Total} = \varepsilon_{Mechanical} + \varepsilon_{Thermal} \tag{50}$$

Assuming that the deformed shape of the beam can be characterized by a lateral displacement $w(x,t)$ and a longitudinal displacement $u(x,t)$, the aggregate axial strain is

given by [1, 10]:

$$\varepsilon_{Total} = \frac{\partial u(x,t)}{\partial x} + \frac{1}{2}\left(\frac{\partial w(x,t)}{\partial x}\right)^2 \tag{51}$$

In addition, the thermal strain is given by

$$\varepsilon_{Thermal} = \alpha(T_b(x,t) - T_0). \tag{52}$$

where α is the coefficient of thermal expansion of Nickel, $T_b(x,t)$ is the temperature along the beam, and T_0 is the ambient temperature. Using Eqs. (50)-(52), the mechanical strain is obtained as

$$\varepsilon_{Mechanical} = \varepsilon_{Total} - \varepsilon_{Thermal} = \frac{\partial u(x,t)}{\partial x} + \frac{1}{2}\left(\frac{\partial w(x,t)}{\partial x}\right)^2 - \alpha(T_b(x,t) - T_0). \tag{53}$$

Eq. (53) is next multiplied by the coefficient EA_b to find the force caused by the strain

$$EA_b\left[\frac{\partial u(x,t)}{\partial x} + \frac{1}{2}\left(\frac{\partial w(x,t)}{\partial x}\right)^2 - \alpha(T_b(x,t) - T_0)\right] = -P(t). \tag{54}$$

Integrating both sides of Eq. (54) over the length of the beam l_b gives

$$\int_0^{l_b}\left[\frac{\partial u(x,t)}{\partial x} + \frac{1}{2}\left(\frac{\partial w(x,t)}{\partial x}\right)^2\right]dx - \int_0^{l_b}\left[\alpha(T_b(x,t) - T_0)\right]dx = -\frac{1}{EA_b}\int_0^{l_b} P(t)dx. \tag{55}$$

Evaluating the first integral gives

$$u(l_b,t) - u(0,t) + \frac{1}{2}\int_0^{l_b}\left(\frac{\partial w(x,t)}{\partial x}\right)^2 dx - \int_0^{l_b}\left[\alpha(T_b(x,t) - T_0)\right]dx = -\frac{1}{EA_b}\int_0^{l_b} P(t)dx \tag{56}$$

where

$$u(0,t) = 0 \tag{57}$$

and

$$u(l_b,t) = w(l_b,t)\tan\theta \tag{58}$$

are the boundary conditions and θ is the inclination angle of the beam [1]. Applying the boundary conditions of Eqs. (57,58) yields

$$w(l_b,t)\tan\theta+\frac{1}{2}\int_0^{l_b}\left(\frac{\partial w(x,t)}{\partial x}\right)^2 dx-\int_0^{l_b}[\alpha(T_b(x,t)-T_0)]\,dx=-\frac{1}{EA_b}\int_0^{l_b}P(t)dx. \tag{59}$$

Evaluating the integral on the right-hand side of Eq. (59) results in

$$w(l_b,t)\tan\theta+\frac{1}{2}\int_0^{l_b}\left(\frac{\partial w(x,t)}{\partial x}\right)^2 dx-\alpha l_b(\bar{T}_b(t)-T_0)=-\frac{l_b}{EA_b}P(t) \tag{60}$$

where $\bar{T}_b(t)-T_0=\frac{1}{l_b}\int_0^{l_b}(T_b(x,t)-T_0)dx$ is the average temperature increase in the beam which is obtained by the electro-thermal macromodel.

Expanding $F(t)$ using Eq. (60) gives

$$F(t)=C_1\left(w(l_b,t)\tan\theta+\frac{1}{2}\int_0^{l_b}\left(\frac{\partial w(x,t)}{\partial x}\right)^2 dx-\alpha l_b(\bar{T}_b(t)-T_0)\right)\delta(x-l_b) \tag{61}$$

where $C_1=-EA_b\tan\theta/l_b$.

Consequently, Eqs. (48), (60), and (61) represent the model for the dynamic buckling of beams in the actuator. Therefore, the PDE involves nonlinear terms. In order to reduce its complexity and develop a macromodel by converting the nonlinear PDE into a system of nonlinear ordinary differential equations, the Galerkin method [49, 50] is applied in the following section.

6.2. Formulation for One Beam Element

It is assumed that the solution of Eq. (48) is of the following form for one beam element [49–51]:

$$w(x,t)^{(e)}=[N(x)][\gamma(t)]^{(e)} \tag{62}$$

where $[N(x)] = [N_1(x)\ N_2(x)\ N_3(x)\ N_4(x)]$ is a row vector containing the interpolation functions

$$\begin{aligned} N_1(x) &= 1 - \frac{3x^2}{l_e^2} + \frac{2x^3}{l_e^3} \\ N_2(x) &= x - \frac{2x^2}{l_e} + \frac{x^3}{l_e^2} \\ N_3(x) &= \frac{3x^2}{l_e^2} - \frac{2x^3}{l_e^3} \\ N_4(x) &= -\frac{x^2}{l_e} + \frac{x^3}{l_e^2} \end{aligned} \tag{63}$$

which are known as *Hermite cubics* [51]. In addition, l_e is the element length, $[\gamma(t)]^{(e)} = [w_1(t)\ \theta_1(t)\ w_2(t)\ \theta_2(t)]^T$ is a column vector composed of nodal displacements for the beam element (e); $w_1(t)$ and $w_2(t)$ are nodal displacements, and $\theta_1(t)$ and $\theta_2(t)$ are nodal angular displacements. Replacing $w(x,t)^{(e)}$ for $w(x,t)$ in Eq. (48)

$$EI_e \frac{\partial^4 w(x,t)^{(e)}}{\partial x^4} + P(t)\frac{\partial^2 w(x,t)^{(e)}}{\partial x^2} + \rho_{Ni} A_e \frac{\partial^2 w(x,t)^{(e)}}{\partial t^2} - F(t) = R(x,t) \tag{64}$$

where I_e is the second-order moment of the element, A_e is the cross-section area of the element, and $R(x,t)$ is the residual term.

The Galerkin method along with the shape functions is applied in Eq. (64). The averaged weighted residual of Eq. (48) for a beam element of length l_e is:

$$\begin{aligned} &I = \int_0^{l_e} [N(x)]^T R(x,t)dx = \\ &\int_0^{l_e} [N(x)]^T \left(EI_e \frac{\partial^4 w(x,t)^{(e)}}{\partial x^4} + P(t)\frac{\partial^2 w(x,t)^{(e)}}{\partial x^2} + \rho_{Ni} A_e \frac{\partial^2 w(x,t)^{(e)}}{\partial t^2} - F(t) \right) dx = 0 \end{aligned} \tag{65}$$

Multiplying $[N(x)]^T$ through the parentheses results in

$$\begin{aligned} I = &\int_0^{l_e} [N(x)]^T EI_e \frac{\partial^4 w(x,t)^{(e)}}{\partial x^4} dx + \int_0^{l_e} [N(x)]^T P(t)\frac{\partial^2 w(x,t)^{(e)}}{\partial x^2} dx \\ &+ \int_0^{l_e} [N(x)]^T \rho_{Ni} A_e \frac{\partial^2 w(x,t)^{(e)}}{\partial t^2} dx - \int_0^{l_e} [N(x)]^T F(t)dx = 0 \end{aligned} \tag{66}$$

or

$$I = I_1 + I_2 + I_3 + I_4 = 0 \tag{67}$$

Integration by parts is applied twice on I_1 to reduce the order of the derivative term.

$$\begin{aligned} I_1 = EI_e \left([N(x)]^T \frac{\partial^3 w(x,t)^{(e)}}{\partial x^3} \right)_0^{l_e} - EI_e \left(\frac{d}{dx}[N(x)]^T \frac{\partial^2 w(x,t)^{(e)}}{\partial x^2} \right)_0^{l_e} \\ + EI_e \int_0^{l_e} \frac{d^2}{dx^2}[N(x)]^T \frac{\partial^2 w(x,t)^{(e)}}{\partial x^2} dx \end{aligned} \tag{68}$$

Evaluating the limits and keeping the integral term unchanged in Eq. (68) gives

$$\begin{aligned} I_1 = -\begin{bmatrix} 1 \\ 0 \\ 0 \\ 0 \end{bmatrix} S(0) + \begin{bmatrix} 0 \\ 0 \\ 1 \\ 0 \end{bmatrix} S(l_e) + \begin{bmatrix} 0 \\ 1 \\ 0 \\ 0 \end{bmatrix} M(0) - \begin{bmatrix} 0 \\ 0 \\ 0 \\ 1 \end{bmatrix} M(l_e) \\ + EI_e \int_0^{l_e} \frac{d^2}{dx^2}[N(x)]^T \frac{\partial^2 w(x,t)^{(e)}}{\partial x^2} dx \end{aligned} \tag{69}$$

where $S(0)$ and $S(l_e)$ denote the shear forces, and $M(0)$ and $M(l_e)$ are the bending moments at the two ends of the beam given as following

$$S(0) = EI_e \left(\frac{\partial^3 w(x,t)^{(e)}}{\partial x^3} \right)_{x=0} \tag{70}$$

$$S(l_e) = EI_e \left(\frac{\partial^3 w(x,t)^{(e)}}{\partial x^3} \right)_{x=l_e} \tag{71}$$

$$M(0) = EI_e \left(\frac{\partial^2 w(x,t)^{(e)}}{\partial x^2} \right)_{x=0} \tag{72}$$

$$M(l_e) = EI_e \left(\frac{\partial^2 w(x,t)^{(e)}}{\partial x^2} \right)_{x=l_e} \tag{73}$$

Let $S(0) = S_1$, $S(l_e) = S_2$, $M(0) = M_1$, and $M(l_e) = M_2$. Therefore, I_1 becomes

$$I_1 = EI_e \int_0^{l_e} \frac{d^2}{dx^2}[N(x)]^T \frac{\partial^2 w(x,t)^{(e)}}{\partial x^2} dx - [Q(t)]^{(e)} \tag{74}$$

where

$$[Q(t)]^{(e)} = \begin{bmatrix} S_1 \\ -M_1 \\ -S_2 \\ M_2 \end{bmatrix} \tag{75}$$

is the vector of shear forces (S_1, S_2) and bending moments (M_1, M_2) at the two ends of the beam element.

Afterwards, Eq. (62) is substituted for $w(x,t)^{(e)}$ in Eq. (74) which gives

$$I_1 = EI_e \int_0^{l_e} \frac{d^2}{dx^2}[N(x)]^T \frac{d^2}{dx^2}[N(x)]dx[\gamma(t)]^{(e)} - [Q(t)]^{(e)} = [K]^{(e)}[\gamma(t)]^{(e)} - [Q(t)]^{(e)} \tag{76}$$

where $[K]^{(e)}$ is the element stiffness matrix given by

$$[K]^{(e)} = \frac{EI_e}{l_e^3} \begin{bmatrix} 12 & 6l_e & -12 & 6l_e \\ 6l_e & 4l_e^2 & -6l_e & 2l_e^2 \\ -12 & -6l_e & 12 & -6l_e \\ 6l_e & 2l_e^2 & -6l_e & 4l_e^2 \end{bmatrix}. \tag{77}$$

Using Eqs. (60,62) and evaluating I_2 gives

$$\begin{aligned} I_2 &= \int_0^{l_e} [N(x)]^T [N(l_e)]\ [\gamma(t)]^{(e)} \tan\theta \frac{d^2}{dx^2}[N(x)]dx[\gamma(t)]^{(e)} \\ &+ \frac{1}{2}\int_0^{l_e} [N(x)]^T N_L \frac{d^2}{dx^2}[N(x)]dx[\gamma(t)]^{(e)} \\ &- \alpha l_e(\bar{T}_e(t) - T_0)\int_0^{l_e} [N(x)]^T \frac{d^2}{dx^2}[N(x)]dx[\gamma(t)]^{(e)} \\ &= -\frac{l_e}{EA_e}\int_0^{l_e} [N(x)]^T P(t) \frac{d^2}{dx^2}[N(x)]dx[\gamma(t)]^{(e)} \end{aligned} \tag{78}$$

where $\bar{T}_e(t) - T_0 = \int_0^{l_e}(T_e(x,t) - T_0)dx/l_e$ is the average temperature increase in the beam element. In addition,

$$[N(l_e)]\ = [0\ \ 0\ \ 1\ \ 0] \tag{79}$$

and

$$\begin{aligned} N_L = {} & (6/5l_e)w_1^2(t) + (2l_e/15)\theta_1^2(t) + (6/5l_e)w_2^2(t) + (2l_e/15)\theta_2^2(t) \\ & + 2((1/10)w_1(t)\theta_1(t) - (6/5l_e)w_1(t)w_2(t) + (1/10)w_1(t)\theta_2(t) \\ & - (1/10)\theta_1(t)w_2(t) - (l_e/30)\theta_1(t)\theta_2(t) - (1/10)w_2(t)\theta_2(t)). \end{aligned} \tag{80}$$

Furthermore,

$$[K_N]^{(e)} = \int_0^{l_e} [N(x)]^T \frac{d^2}{dx^2}[N(x)]dx = \begin{bmatrix} -6/5l_e & -11/10 & 6/5l_e & -1/10 \\ -1/10 & -2l_e/15 & 1/10 & l_e/30 \\ 6/5l_e & 1/10 & -6/5l_e & 11/10 \\ -1/10 & l_e/30 & 1/10 & -2l_e/15 \end{bmatrix} \tag{81}$$

is the geometric stiffness matrix. Using Eqs. (79,80,81), Eq. (78) can be written as

$$\begin{aligned} I_2 &= -\frac{l_e}{EA_e} P(t)[K_N][\gamma(t)]^{(e)} \\ &= \tan\theta [K_N] w_2(t)[\gamma(t)]^{(e)} + 1/2[K_N]N_L[\gamma(t)]^{(e)} - \alpha l_e(\bar{T}_e(t) - T_0)[K_N][\gamma(t)]^{(e)}. \end{aligned} \tag{82}$$

Using Eq. (62) and evaluating I_3 results in

$$I_3 = \rho_{Ni} A_e \int_0^{l_e} [N(x)]^T [N(x)]dx \frac{d^2}{dt^2}[\gamma(t)]^{(e)} \tag{83}$$

The matrix $[M]^{(e)}$ is the element mass matrix given by

$$[M]^{(e)} = \rho_{Ni} A_e \int_0^{l_e} [N(x)]^T [N(x)]dx = \frac{\rho_{Ni} A_e l_e}{420} \begin{bmatrix} 156 & 22l_e & 54 & -13l_e \\ 22l_e & 4l_e^2 & 13l_e & -3l_e^2 \\ 54 & 13l_e & 156 & -22l_e \\ -13l_e & -3l_e^2 & -22l_e & 4l_e^2 \end{bmatrix} \tag{84}$$

Expanding I_4 using Eq. (49) gives

$$I_4 = -\int_0^{l_e} [N(x)]^T P(t) \tan\theta \, \delta(x - l_e) \tag{85}$$

Evaluating the integral simplifies Eq. (85) to

$$I_4 = -[0 \;\; 0 \;\; P(t)\tan\theta \;\; 0]^T \tag{86}$$

Using Eqs. (77, 81, 84) , and adding I_1, I_2, I_3, and I_4, the equation of motion of the beam element can be written as

$$[M]^{(e)}\frac{d^2}{dt^2}[\gamma(t)]^{(e)}+[K]^{(e)}[\gamma(t)]^{(e)}+P(t)[K_N]^{(e)}[\gamma(t)]^{(e)}=[Q(t)]^{(e)}+[\Phi(t)]^{(e)} \quad (87)$$

where $[\Phi(t)]^{(e)}=[0\ \ 0\ \ P(t)\tan\theta\ \ 0]^T$.

6.3. Model Formulation of the Actuator

In this part, the formulation derived in Section 6.2 is used to obtain the dynamics of the actuator considering one beam and half of the shuttle using two beam elements. The shuttle is included to improve the accuracy of the model. The vector of nodal displacements for two beam elements is given as

$$[\gamma(t)]_0^{(b)+(s)}=\begin{bmatrix} w_1(t)\\ \theta_1(t)\\ w_2(t)\\ \theta_2(t)\\ w_3(t)\\ \theta_3(t)\end{bmatrix} \quad (88)$$

where $w_i(t)$ and $\theta_i(t)$ denote the lateral displacement and slope at the i^{th} node for $i=1,2,3$, and the subscript in $[\gamma(t)]_0$ is used to show that the boundary conditions are not yet applied. Furthermore, the superscripts (b) and (s) denote the elements for the beam and the shuttle.

Let I_b and I_{sh} be the second-order moments of the beam and of half of the shuttle, respectively. In addition, defining $l_{sh}=l_s/2$, the stiffness matrix for the beam is given

by

$$[K]^{(b)} = \frac{EI_b}{l_b^3}\begin{bmatrix} 12 & 6l_b & -12 & 6l_b & 0 & 0 \\ 6l_b & 4l_b^2 & -6l_b & 2l_b^2 & 0 & 0 \\ -12 & -6l_b & 12 & -6l_b & 0 & 0 \\ 6l_b & 2l_b^2 & -6l_b & 4l_b^2 & 0 & 0 \\ 0 & 0 & 0 & 0 & 0 & 0 \\ 0 & 0 & 0 & 0 & 0 & 0 \end{bmatrix}. \tag{89}$$

The stiffness matrix for half of the shuttle is given as

$$[K]^{(s)} = \frac{EI_{sh}}{l_{sh}^3}\begin{bmatrix} 0 & 0 & 0 & 0 & 0 & 0 \\ 0 & 0 & 0 & 0 & 0 & 0 \\ 0 & 0 & 12 & 6l_{sh} & -12 & 6l_{sh} \\ 0 & 0 & 6l_{sh} & 4l_{sh}^2 & -6l_{sh} & 2l_{sh}^2 \\ 0 & 0 & -12 & -6l_{sh} & 12 & -6l_{sh} \\ 0 & 0 & 6l_{sh} & 2l_{sh}^2 & -6l_{sh} & 4l_{sh}^2 \end{bmatrix}. \tag{90}$$

Moreover, the geometric stiffness matrices for the two elements are obtained as

$$[K_N]^{(b)} = \begin{bmatrix} -6/5l_b & -11/10 & 6/5l_b & -1/10 & 0 & 0 \\ -1/10 & -2l_b/15 & 1/10 & l_b/30 & 0 & 0 \\ 6/5l_b & 1/10 & -6/5l_b & 11/10 & 0 & 0 \\ -1/10 & l_b/30 & 1/10 & -2l_b/15 & 0 & 0 \\ 0 & 0 & 0 & 0 & 0 & 0 \\ 0 & 0 & 0 & 0 & 0 & 0 \end{bmatrix} \tag{91}$$

$$[K_N]^{(s)} = \begin{bmatrix} 0 & 0 & 0 & 0 & 0 & 0 \\ 0 & 0 & 0 & 0 & 0 & 0 \\ 0 & 0 & -6/5l_{sh} & -11/10 & 6/5l_{sh} & -1/10 \\ 0 & 0 & -1/10 & -2l_{sh}/15 & 1/10 & l_{sh}/30 \\ 0 & 0 & 6/5l_{sh} & 1/10 & -6/5l_{sh} & 11/10 \\ 0 & 0 & -1/10 & l_{sh}/30 & 1/10 & -2l_{sh}/15 \end{bmatrix}. \tag{92}$$

Let A_b and A_{sh} be the cross-section areas of the beam and the shuttle, respectively. Eqs. (93) and (94) describe the mass matrices for the two elements.

$$[M]^{(b)} = \frac{2\rho_{Ni}A_b l_b}{420}\begin{bmatrix} 156 & 22l_b & 54 & -13l_b & 0 & 0 \\ 22l_b & 4l_b^2 & 13l_b & -3l_b^2 & 0 & 0 \\ 54 & 13l_b & 156 & -22l_b & 0 & 0 \\ -13l_b & -3l_b^2 & -22l_b & 4l_b^2 & 0 & 0 \\ 0 & 0 & 0 & 0 & 0 & 0 \\ 0 & 0 & 0 & 0 & 0 & 0 \end{bmatrix} \tag{93}$$

$$[M]^{(s)} = \frac{2\rho_{Ni}A_{sh}l_{sh}}{420}\begin{bmatrix} 0 & 0 & 0 & 0 & 0 & 0 \\ 0 & 0 & 0 & 0 & 0 & 0 \\ 0 & 0 & 156 & 22l_{sh} & 54 & -13l_{sh} \\ 0 & 0 & 22l_{sh} & 4l_{sh}^2 & 13l_{sh} & -3l_{sh}^2 \\ 0 & 0 & 54 & 13l_{sh} & 156 & -22l_{sh} \\ 0 & 0 & -13l_{sh} & -3l_{sh}^2 & -22l_{sh} & 4l_{sh}^2 \end{bmatrix} \tag{94}$$

It should be noted that the mass matrices in Eqs. (93) and (94) were multiplied by two to account for the masses of the missing halves of the beam and the shuttle.

The following boundary conditions for the structure of Fig. (20a) are applied:

$$w(0,t) = 0 \tag{95}$$

$$\frac{\partial w(0,t)}{\partial x} = 0 \tag{96}$$

$$\frac{\partial w(l_b,t)}{\partial x} = 0 \tag{97}$$

$$\frac{\partial w(l_b+l_{sh},t)}{\partial x} = 0 \tag{98}$$

These boundary conditions reduce $[\gamma(t)]_0$ to the following as shown in Fig. (21):

$$[\gamma(t)]^{(b)+(s)} = \begin{bmatrix} w_2(t) \\ w_3(t) \end{bmatrix} \tag{99}$$

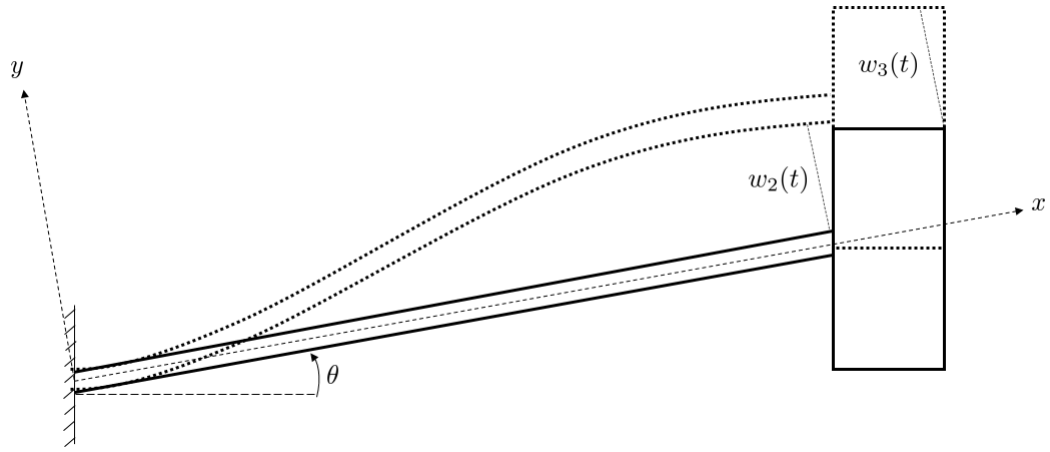

Figure 21: Geometry of buckled model of the half-span of the actuator along with the nodal parameters.

Therefore, all the entries of the matrices that are placed on the rows and the columns corresponding to the i^{th} rows and the j^{th} columns for $i, j = 1, 2, 4, 6$ are crossed out. These entries correspond to the nodal parameters which were equated to zero. The resulting columns and rows elimination reduces the size of the matrices to 2×2.

Let

$$a = \frac{EI_b}{l_b^3}$$
$$c = \frac{EI_{sh}}{l_{sh}^3}$$
$$d = \frac{2\rho_{Ni}A_b l_b}{420}$$
$$f = \frac{2\rho_{Ni}A_{sh} l_{sh}}{420}$$

the stiffness, geometric stiffness, and mass matrices for the actuator after applying the boundary conditions and adding the matrices for the two elements are given as

$$[K]^{(b)+(s)} = \begin{bmatrix} 12(a+c) & -12c \\ -12c & 12c \end{bmatrix} \tag{100}$$

$$[K_N]^{(b)+(s)} = \begin{bmatrix} (-6/5)(1/l_b + 1/l_{sh}) & 6/5l_{sh} \\ 6/5l_{sh} & -6/5l_{sh} \end{bmatrix} \tag{101}$$

$$[M]^{(b)+(s)} = \begin{bmatrix} 156(d+f) & 54f \\ 54f & 156f \end{bmatrix}. \tag{102}$$

Moreover, the axial force and the force at the tip of the actuator take the following forms:

$$\begin{aligned} P(t)^{(b)+(s)} = &- \frac{EA_b}{l_b}(w_2(t)\tan\theta + \frac{3}{5l_b}w_2^2(t) - \alpha l_b(\bar{T}_b(t) - T_0)) \\ &- \frac{EA_{sh}}{l_{sh}}(w_3(t)\tan\theta + \frac{3}{5l_{sh}}w_2^2(t) + \frac{3}{5l_{sh}}w_3^2(t) \\ &- \frac{6}{5l_{sh}}w_2(t)w_3(t) - \alpha l_{sh}(\bar{T}_s(t) - T_0)). \end{aligned} \tag{103}$$

$$[\Phi(t)]^{(b)+(s)} = \begin{bmatrix} 0 \\ P(t)\tan\theta \end{bmatrix} \tag{104}$$

Finally, $[Q(t)]^e$ in Eq. (87) was assumed to be zero.

Using Eqs. (87,100,101,102,103,104), the equation of motion for a two-beam thermally driven MEMS actuator can be written as [46]

$$\begin{aligned} [M]^{(b)+(s)}\frac{d^2}{dt^2}[\gamma(t)]^{(b)+(s)} + [K]^{(b)+(s)}[\gamma(t)]^{(b)+(s)} + P(t)^{(b)+(s)}[K_N]^{(b)+(s)}[\gamma(t)]^{(b)+(s)} \\ = [\Phi(t)]^{(b)+(s)} \end{aligned} \tag{105}$$

Solution of Eq. (105) yields the lateral displacement of the actuator. The tip displacements of the beam $\delta_b(t)$ and of the shuttle $\delta_s(t)$ shown in Fig. (20a) can be obtained by the following equations [1]:

$$\delta_b(t) = \frac{w_2(t)}{\cos\theta} \tag{106}$$

$$\delta_s(t) = \frac{w_3(t)}{\cos\theta} \tag{107}$$

In order to develop a more accurate macromodel for the eight-beam actuator, the thermomechanical macromodel for the two-beam actuator is modified by increasing the in-plane thickness of the beam w_b fourfold. In other words, the four beams are combined to have one beam. However, the second-order moment is remained unchanged.

6.4. Simulation Results

The electro-thermal macromodel developed in Section 5 is fed into the thermo-mechanical macromodel developed for eight-beam actuators to obtain the dynamic tip displacement $\delta_s(t)$ of the eight-beam thermally driven MEMS actuator. It is important to note that since the inclination angle θ of the actuator used in our analysis is small (0.8°), the lateral and tip displacements are almost identical. The data tabulated in Table 8 are used to simulate the actuator's tip displacement using the electro-thermo-mechanical macromodel in SIMULINK.

Table 8: Nickel material properties.

Parameter	Symbol	Value	Reference	Units
Young's Modulus	E^{T_0}	205	[52]	GPa
Coefficient of Thermal Expansion	α^{T_0}	13.4×10^{-6}	[41]	$1/K$

Static measurements of the actuator's tip displacement for several actuation voltages are compared with the steady-state values obtained by the macromodel and the FEM as shown in Table 9. A very good agreement is observed in the steady-state tip displacements obtained by the macromodel, the FEM, and the experimental measurements. For the macromodel, the maximum error occurs at 14 V which is within 7% of the measurement. For the FEM, the maximum error is observed at 14 V and is within 5% of the measurement. Therefore, the proposed macromodel is reasonably accurate and efficient for predicting the actuator's tip displacements.

In addition, SIMULINK and ANSYS dynamic simulations of the actuator's tip displacement are shown for actuation voltages of 6 V and 12 V. The tip displacements are plotted versus time in Fig. (22). As it is shown, the macromodel exhibits a faster transient response in comparison with the FEM. At 12 V, the error is higher than at 6 V. We have investigated that by increasing the number of segments of the beams in the LEM, the electro-thermal model becomes close to a distributed model rather than a lumped model, and therefore, the error associated with the transient response decreases. However, this is a trade-off between simplicity and accuracy of the macromodel.

Table 9: Comparison of steady-state values of the actuator's tip displacements.

	Experimental	Macromodel		FEM	
Voltage (V)	δ_s (μm)	δ_s (μm)	% Error (%)	δ_s (μm)	% Error (%)
6	16.7	15.70	5.99	16.71	0.06
8	24.6	23.36	5.04	24.32	1.14
10	31.4	30.30	3.50	30.85	1.75
12	35.7	36.66	2.69	35.34	1.01
14	39.4	42.84	8.73	41.12	4.37

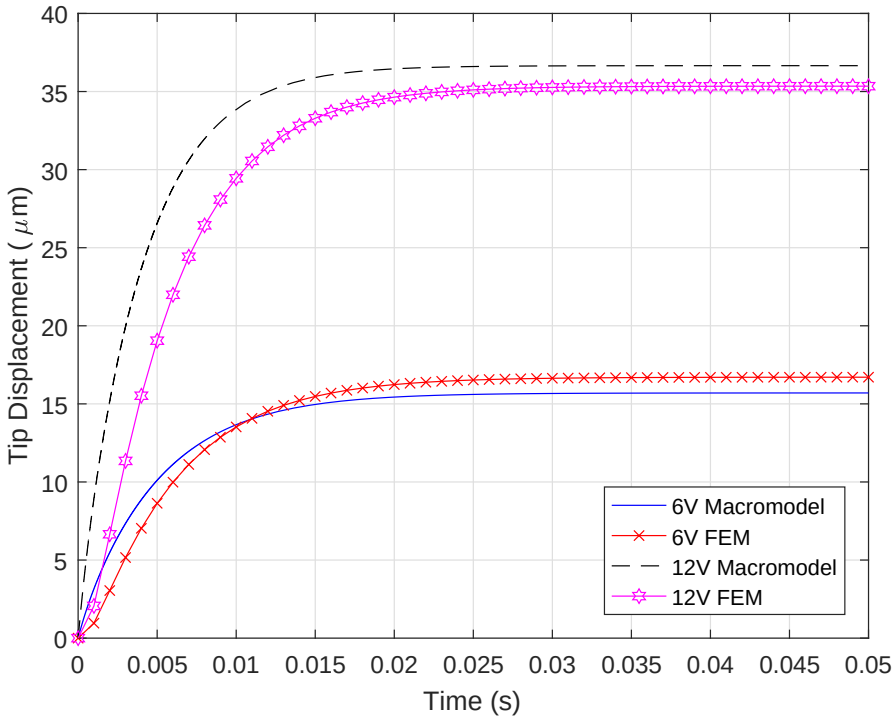

Figure 22: SIMULINK and ANSYS simulations of the actuator's tip displacement for 6V and 12V.

Chapter 7: Black-Box Modeling of the V-Shaped Thermal MEMS Actuator

In contrast to the white-box modeling approach employed in the macromodeling process discussed in chapters 5 and 6, no physical insight of the system exists in the black-box modeling approach, and a model from a set of standard models is used to obtain an input-output relation. Using this approach, we propose a first-order ordinary differential equation that relates the input voltage to the output displacement of the MEMS actuator, which was modeled in ANSYS. The model is based on the displacement data corresponding to different input voltages obtained through the ANSYS transient dynamic analysis. The data are then fed into the MATLAB System Identification Toolbox to find a transfer function for each input voltage. In the following sections, the process of obtaining the dynamic model is presented.

7.1. Transfer Function Model Estimation Using MATLAB System Identification Toolbox

After feeding the voltage-displacement data into the MATLAB System Identification Toolbox, different transfer function models based on the number of the zeros and the poles were estimated. The transfer functions with one pole showed very good reproductions of the displacement data in response to the given input voltages. Therefore, the black-box model discussed in chapter 4, which was illustrated by Fig. (14), can be represented by the equivalent system shown in Fig. (23). In the figure, $u(t)$ is the input voltage applied to the MEMS actuator, and $y(t)$ is the MEMS actuator's tip displacement.

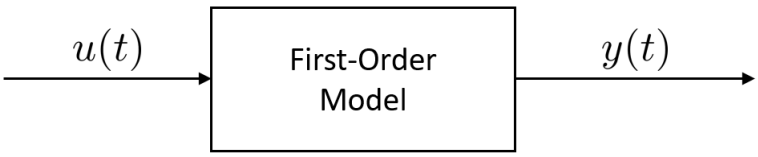

Figure 23: Equivalent first-order model for the thermal MEMS actuator.

For a given voltage, the transfer functions can be described by

$$G(s) = \frac{Y(s)}{U(s)} = \frac{b}{s+a} \tag{108}$$

where $Y(s)$ and $U(s)$ are the Laplace transforms of the MEMS actuator's tip displacement $y(t)$, and the input voltage $u(t)$.

The obtained first-order transfer functions for different input voltages are shown in Table 10. As can be seen, the tabulated Goodness of Fits obtained from MATLAB indicate that the estimated first-order transfer functions reproduce the displacement data sufficiently accurate.

Table 10: Estimated transfer function models using MATLAB System Identification Toolbox.

Voltage (V)	Transfer Function $G(s)$	Goodness of Fit (%)
2	$\frac{93.57}{s+171}$	98.34
4	$\frac{318.6}{s+173.1}$	98.07
6	$\frac{493.7}{s+176.7}$	97.63
8	$\frac{557.7}{s+182.9}$	97.27
10	$\frac{579.9}{s+187.3}$	97.16
12	$\frac{561.4}{s+190}$	97.04
14	$\frac{571.6}{s+193.9}$	96.81

7.2. Dynamic Modeling Based on the Estimated Transfer Functions

As can be seen, the gains and the poles of the transfer functions tabulated in Table (10) are different for different input voltages. Figs. (24a) and (24b) depict the variations of the poles and the gains for the varying input voltages.

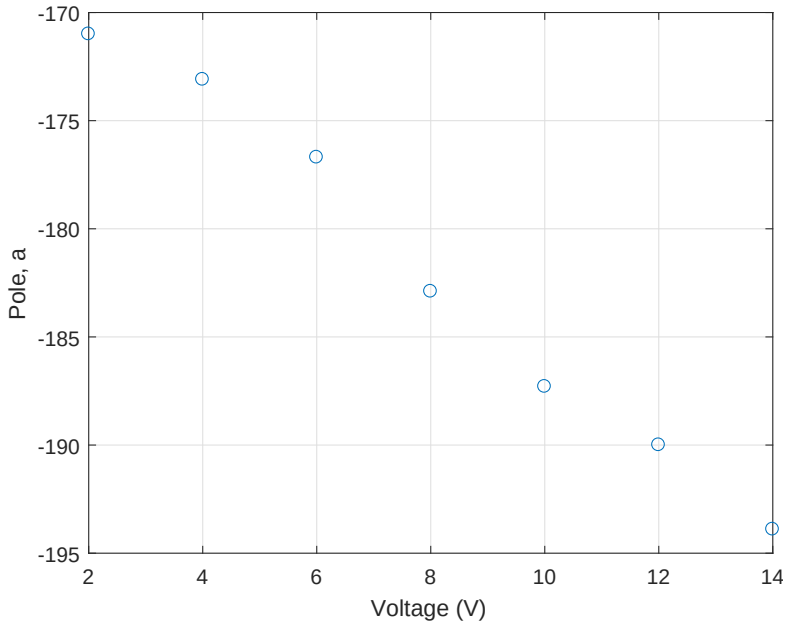

(a)

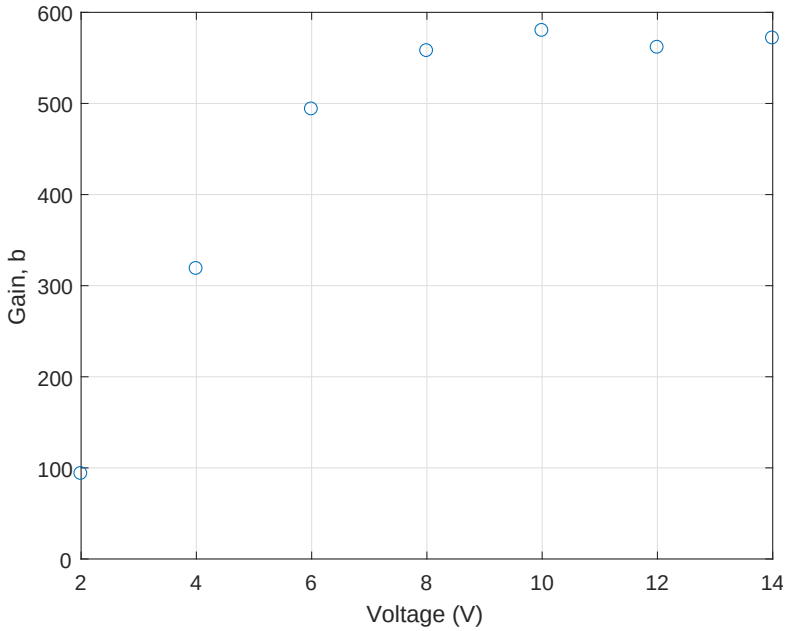

(b)

Figure 24: Plots of the transfer functions' poles and gains for different input voltages (a) poles as a function of voltage (b) gains as a function of voltage.

The pole-voltage and the gain-voltage data are next fitted with the following polynomials:

$$a(u) = 0.016u^3 - 0.386u^2 + 0.6427u - 170.7 \tag{109}$$

$$b(u) = 0.5175u^3 - 18.746u^2 + 221.91u - 285.48 \tag{110}$$

Therefore, the dynamic model of the MEMS actuator can be expressed by

$$\frac{dy(t)}{dt} = -a(u)y(t) + b(u)u(t) \tag{111}$$

where the poles and the gains are nonlinear functions of the input voltage. Fig. (25) shows Eq. (111) in the block diagram form.

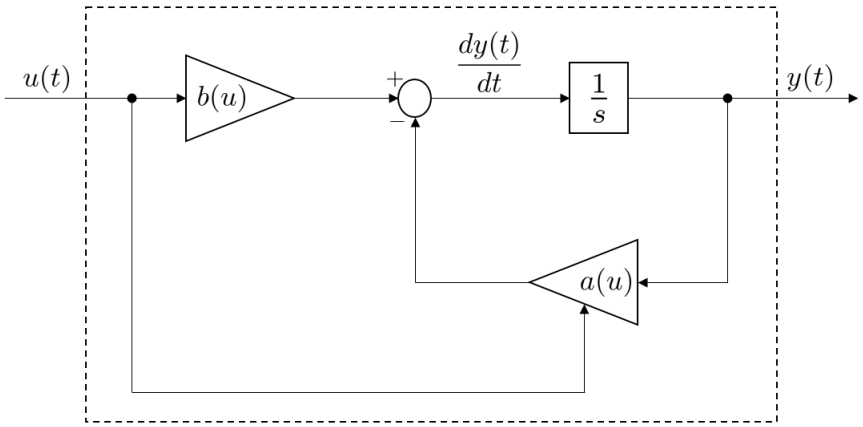

Figure 25: Block diagram representation of the first-order model.

7.3. Simulation Results

The first-order model was simulated in SIMULINK and was compared with the FEM results for actuation voltages of 6 V and 12 V. Fig. (26) depicts the results. As can be seen, the results are in very good agreement.

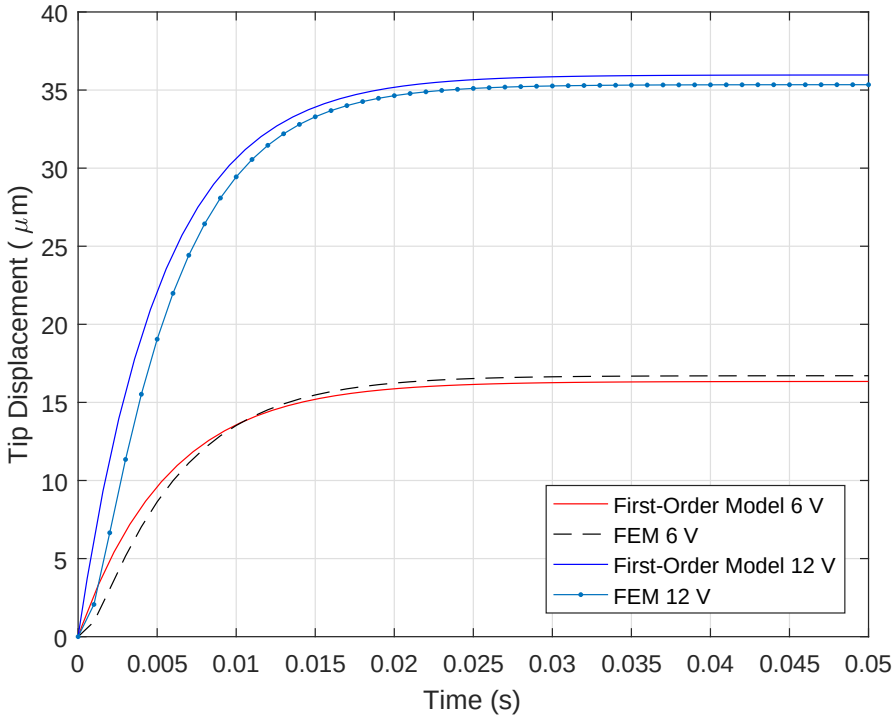

Figure 26: Comparison of the tip displacements obtained by the first-order model and the FEM.

Chapter 8: Self-Tuning of PID Controllers by Adaptive Interaction

8.1. Introduction

The self-tuning or adaptation algorithm for PID controllers was proposed based on the theory of adaptive interaction [25]. The algorithm is robust to changes in the plant as it does not require any knowledge of the plant to be controlled. In addition, the algorithm can be applied universally to linear and nonlinear plants. The proposed self-tuning PID controller is a nonlinear controller as the PID parameters change continuously based on nonlinear adaptation dynamics. Because of its simplicity and effectiveness, the algorithm shall be used to improve the transient response of the thermally driven V-shaped MEMS actuator.

8.2. Control Algorithm

A PID control system is broken down into four devices as reported in [25]. Device 1 is the proportional part, Device 2 is the integral action, Device 3 is the derivative action, and Device 4 is the plant. In some implementations, the derivative action is preceded by a low-pass filter; the algorithm applies equally well under this modification. In any case, there are three adaptive connections: $\eta_c = K_P,\ K_I,\ K_D$. For these connections, the adaptive algorithm presented in Theorem 1 (chapter 2) becomes

$$\frac{d\eta_c}{dt} = -\sigma \frac{\partial \mathscr{E}}{\partial y_{post_c}} \circ \mathscr{F}'_{post_c}[x_{post_c}] \circ y_{pre_c} \tag{112}$$

where $post_c = 4$, $pre_c = 1,2,3$ depending on the adaptive connection, $\circ$ denotes composition, i.e.

$$y_n(t) = (\mathscr{F}_n \circ x_n)(t) = \mathscr{F}_n[x_n(t)],\ n \in \mathscr{N}$$

and the Fréchet derivative $\mathscr{F}'_n$ of $\mathscr{F}_n$ is defined as a functional such that

$$\lim_{||h||\to 0} \frac{||\mathscr{F}_n[x+h] - \mathscr{F}_n[x] - \mathscr{F}'_n[x] \circ h||}{||h||} = 0.$$

In [25], the error squared is minimized as the performance index

$$\mathscr{E} = e^2 = (r - y_4)^2. \tag{113}$$

Substituting Eq. (113) in Eq. (112), the following tuning algorithm is obtained:

$$\begin{aligned} \frac{dK_P}{dt} &= 2\sigma e \mathscr{F}_4'[x_4] \circ y_1 \\ \frac{dK_I}{dt} &= 2\sigma e \mathscr{F}_4'[x_4] \circ y_2 \\ \frac{dK_D}{dt} &= 2\sigma e \mathscr{F}_4'[x_4] \circ y_3. \end{aligned} \tag{114}$$

Afterwards, the Fréchet derivative is approximated by $\mathscr{F}'[x] \circ h = \nu h$, with ν being a constant. This approximation has been verified by simulation as reported in [25]. Using this approximation, the following set of modified tuning algorithm is obtained:

$$\begin{aligned} \frac{dK_P}{dt} &= \sigma e y_1 \\ \frac{dK_I}{dt} &= \sigma e y_2 \\ \frac{dK_D}{dt} &= \sigma e y_3 \end{aligned} \tag{115}$$

where 2ν has been incorporated in the adaptation coefficient σ. As observed, the modified tuning algorithm is simple and independent of the plant model. As reported in [25], the modified tuning algorithm can be applied to both linear and nonlinear plants with different noise and time delay conditions. Fig. (27) shows the block diagram representation of the adaptive control system where the derivative action is preceded by a low-pass filter with the filter coefficient N.

8.3. Stability Proof of the Modified Tuning Algorithm

In Eq. (108), it was shown that the displacement response of the MEMS actuator can be modeled by a first-order transfer function. Therefore, for a given operating point, the open-loop displacement response of the MEMS actuator can be approximated by the

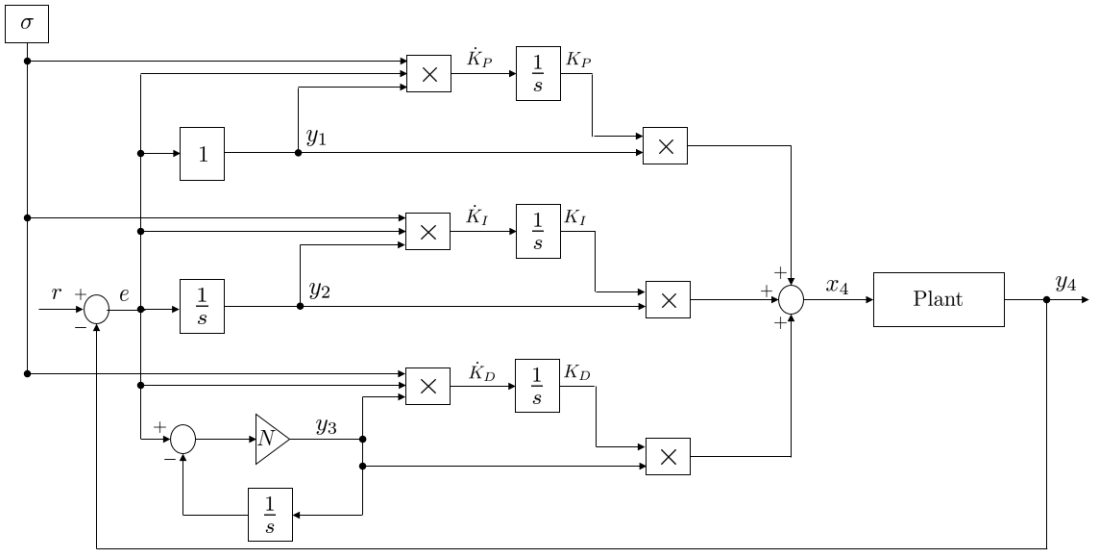

Figure 27: Illustration of the self-tuning PID controller.

following first-order system

$$\frac{dy_4(t)}{dt} = -ay_4(t) + bx_4(t), \;\; a > 0, \; b > 0 \tag{116}$$

where $x_4(t)$ is the control signal, and $y_4(t)$ is the output which is the displacement. To simplify the notation, in the rest of the section, we will eliminate when appropriate, the explicit reference to time t. Assuming that the PID parameters converge to K_P^*, K_I^*, and K_D^*, the control signal x_4 can be written as

$$x_4 = K_P^* e + K_I^* \int e dt + K_D^* \frac{de}{dt} + \tilde{K}_P e + \tilde{K}_I \int e dt + \tilde{K}_D \frac{de}{dt} \tag{117}$$

where

$$\begin{aligned} \tilde{K}_P &= K_P - K_P^* \\ \tilde{K}_I &= K_I - K_I^* \\ \tilde{K}_D &= K_D - K_D^* \end{aligned} \tag{118}$$

Since K_P^* , K_I^*, and K_D^* are constant, we have

$$\begin{aligned}\frac{d\tilde{K}_P}{dt} &= \frac{dK_P}{dt} \\ \frac{d\tilde{K}_I}{dt} &= \frac{dK_I}{dt} \\ \frac{d\tilde{K}_D}{dt} &= \frac{dK_D}{dt}.\end{aligned} \tag{119}$$

Using the modified tuning algorithm (Eq. (115)) in Eq. (119) and ignoring the low-pass filter in the derivative term for simplicity yield

$$\begin{aligned}\frac{d\tilde{K}_P}{dt} &= \sigma e^2 \\ \frac{d\tilde{K}_I}{dt} &= \sigma e \int e dt \\ \frac{d\tilde{K}_D}{dt} &= \sigma e \frac{de}{dt}.\end{aligned} \tag{120}$$

Using $e = r - y_4$ and Eq. (116), the error dynamics can be written as

$$\begin{aligned}\frac{de}{dt} &= \frac{dr}{dt} - \frac{dy_4}{dt} \\ &= 0 - \frac{dy_4}{dt} \\ &= ay_4 - bx_4 \\ &= -a(e-r) - bx_4\end{aligned} \tag{121}$$

for constant r.

Expanding Eq. (121) results in

$$\begin{aligned}\frac{de}{dt} &= -ae + ar - bx_4 \\ &= -ae - bx_4^* - b\tilde{x}_4\end{aligned} \tag{122}$$

where [26]

$$x_4^* = -\frac{a}{b}r + K_I^* \int e dt \tag{123}$$

$$\tilde{x}_4 = K_P^* e + K_D^* \frac{de}{dt} + \tilde{K}_P e + \tilde{K}_I \int e dt + \tilde{K}_D \frac{de}{dt}. \tag{124}$$

Let us introduce the following candidate Lyapunov function

$$V = \frac{1}{2}e^2 + \frac{b}{2\sigma}(K_P)^2 + \frac{b}{2\sigma}(\tilde{K}_I)^2 + \frac{b}{2\sigma}(K_D)^2 + \frac{b}{2K_I^*}(x_4^*)^2 \tag{125}$$

where V is positive definite and continuously differentiable.
Using Eq. (118) in Eq. (125) gives

$$V = \frac{1}{2}e^2 + \frac{b}{2\sigma}(\tilde{K}_P + K_P^*)^2 + \frac{b}{2\sigma}(\tilde{K}_I)^2 + \frac{b}{2\sigma}(\tilde{K}_D + K_D^*)^2 + \frac{b}{2K_I^*}(x_4^*)^2. \tag{126}$$

Taking the derivative of V with respect to t yields

$$\frac{dV}{dt} = e\frac{de}{dt} + \frac{b}{\sigma}(\tilde{K}_P + K_P^*)\frac{d\tilde{K}_P}{dt} + \frac{b}{\sigma}\tilde{K}_I\frac{d\tilde{K}_I}{dt} + \frac{b}{\sigma}(\tilde{K}_D + K_D^*)\frac{d\tilde{K}_D}{dt} + \frac{b}{K_I^*}(x_4^*)\frac{dx_4^*}{dt}. \tag{127}$$

Differentiating Eq. (123) with respect to t results in

$$\frac{dx_4^*}{dt} = K_I^* e. \tag{128}$$

By substituting Eqs. (120,122,128) in Eq. (127), the following expression is obtained

$$\begin{aligned}\frac{dV}{dt} = {} & e(-ae - bx_4^* - b\tilde{x}_4) + \frac{b}{\sigma}(\tilde{K}_P + K_P^*)\sigma e^2 + \frac{b}{\sigma}\tilde{K}_I\sigma e\int e dt + \frac{b}{\sigma}(\tilde{K}_D + K_D^*)\sigma e\frac{de}{dt} \\ & + \frac{b}{K_I^*}x_4^* K_I^* e.\end{aligned} \tag{129}$$

Using Eq. (124) and simplifying Eq. (129), we get

$$\frac{dV}{dt} = -ae^2 - bex_4^* - be\tilde{x}_4 + be\tilde{x}_4 + bex_4^* \tag{130}$$

By canceling the common terms in Eq. (130), the following is obtained

$$\frac{dV}{dt} = -ae^2 \leq 0 \tag{131}$$

Since dV/dt is negative semidefinite, V is a Lyapunov function. Consequently, the system given by Eqs. (120, 122) is stable. However, we are interested in asymptotic stability. Since in Eq. (122) x_4 varies with time, the system is non-autonomous. There-

fore, we need to use Barbalat's Lemma to prove asymptotic stability.

Differentiating dV/dt with respect to t gives

$$\frac{d^2V}{dt^2} = -2ae\frac{de}{dt} \tag{132}$$

Since $dV/dt < 0$, we know that e is bounded. We need to show that de/dt is also bounded. Moreover, since $dV/dt < 0$, e, K_P, K_I, and K_D are bounded. By definition, $e = r - y_4$, and given that $|r| \leq r_{max}$, and since e is bounded, y_4 is also bounded. Therefore, we conclude that de/dt is bounded. Furthermore, since

$$\begin{aligned} V \neq 0 \quad &\forall \;\; e,\, K_P,\, \tilde{K}_I,\, K_D,\, x_4^* \neq 0 \;\; \& \\ V > 0 \quad &\forall \;\; e,\, K_P,\, \tilde{K}_I,\, K_D,\, x_4^* \neq 0 \end{aligned} \tag{133}$$

and $dV/dt < 0$, therefore, V converges to a finite value (has a finite limit).

In addition, we showed that d^2V/dt^2 is bounded. Thus, using Barbalat's Lemma we get

$$\lim_{t\to\infty} \frac{dV}{dt} \to 0 \tag{134}$$

This implies that $e \to 0$ as $t \to \infty$ or $y_4 \to r$ as $t \to \infty$. Consequently, we proved that the system is asymptotically stable [17].

Chapter 9: Controller Design

9.1. Introduction

As the thermally driven MEMS actuator is used to actuate RF MEMS switches, improving the displacement transient response of the MEMS actuator leads to the improvement in the switching time of the RF MEMS switches. Therefore, the objective is to speed up the transient response associated with the MEMS actuator's displacement using control techniques.

In this chapter, two approaches are presented for the controller design. In the first approach, a conventional proportional-integral-derivative (PID) controller as well as an adaptive PID controller are designed and simulated for the electro-thermo-mechanical macromodel developed in chapters 5 and 6. In the second approach, the same type of controllers are designed and simulated for the first-order model developed in chapter 7. These approaches are discussed in sections 9.3 and 9.4, respectively.

9.2. Design Specifications

In order to improve the displacement transient response, the following design specifications need to be taken into consideration in the process of designing the controllers:

- The rise time and the settling time in response to applying a step input are required to be reduced by at least 25%, with reasonable overshoot and steady-state error.
- An upper bound for the peak displacement is set to 38 μm so that the MEMS actuator does not go under a high tensile stress, given that the maximum displacement that the MEMS actuator can exhibit in response to a step voltage is 45 μm.
- The maximum energy produced in the MEMS actuator during the transient time must not exceed 33.16 mJ. This limitation ensures that the MEMS actuator works properly without facing overheating destruction. The limitation applies to the macromodel only.
- The resistance of the polysilicon layer in the macromodel was characterized for the maximum voltage of 16 V as was shown in Fig. (8). Therefore, the control

signal should not exceed this voltage. Beyond this voltage, the obtained resistance from the fitted polynomial might not be correct. This limitation does not apply to the first-order model.

In addition, since the designed controllers will be tested on the actual MEMS actuator in the future, two limitations are imposed by using a high voltage amplifier in the experimental setup. The high voltage amplifier introduces the following limitations:

- Voltage amplification is bounded by +150 V and -150 V with respect to ground.
- The slew rate of the amplifier is 2000 $V/\mu s$.

Since these limitations are relevant to the control signal generated by the designed controller, they need to be considered in the controller design process.

9.3. Controller Design for the Electro-Thermo-Mechanical Macromodel

In order to compare the results obtained by the closed-loop and the open-loop systems, the macromodel was first simulated in open-loop for the actuation voltage of 6 V. The open-loop system is shown in Fig. (28).

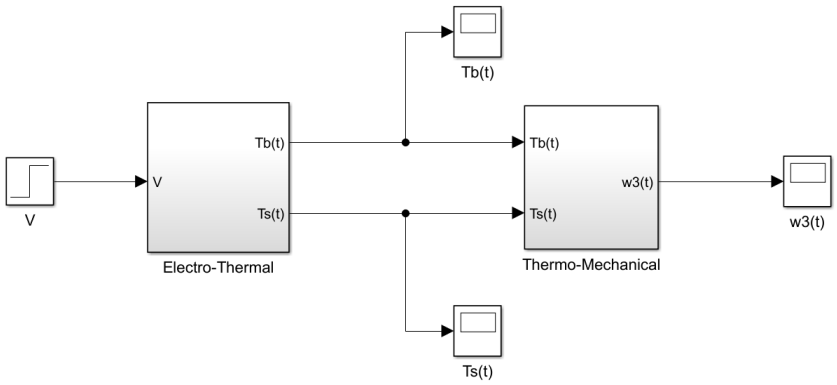

Figure 28: Open-loop system.

Based on the simulation results, the exhibited displacement upon applying 6 V is 15.7 μm. The obtained displacement is then used as the reference in the closed-loop systems. Furthermore, the PID gains were tuned in such a way that the control signals do not exceed 16 V, and the slew rates of the control signals remain within the limit of the amplifier.

9.3.1. Conventional PID controller. A conventional PID controller was designed for the closed-loop system shown in Fig. (29). The controller formula in s-domain is given by

$$K_p + K_i \frac{1}{s} + K_d \frac{N}{1 + N\frac{1}{s}} \tag{135}$$

where $K_P = 0.01$, $K_I = 215$, and $K_D = 2 \times 10^{-3}$. In addition, a low-pass filter with the coefficient $N = 50\ rad/s$ was used with the derivative action.

9.3.2. Adaptive PID controller. In order to study the feasibility of achieving the design requirements, the modified tuning algorithm presented in chapter 8 was employed. The adaptation coefficient was set to $\sigma = 0.00015$. Moreover, the initial PID gains were set to $K_P = 0.01$, $K_I = 215$, and $K_D = 2 \times 10^{-3}$ with $N = 50\ rad/s$, which are the gains used in the conventional PID controller. The SIMULINK model is depicted in Fig. (30).

9.3.3. Simulation results. The closed-loop systems shown in Figs. (29) and (30) were simulated in SIMULINK. The results consisting of the tip displacements, the error signals, the control signals, the consumed power, $\bar{T}_s$, and $\bar{T}_b$ are shown in Figs. (32a)-(34b). Furthermore, the adaptation of the PID gains with time are shown in Figs. (35a)-(36). The initial and the final values of the gains and the control signals are denoted by the subscripts i and f on the plots. Additionally, the subscripts max were used to show the peak values on the plot of the control signals.

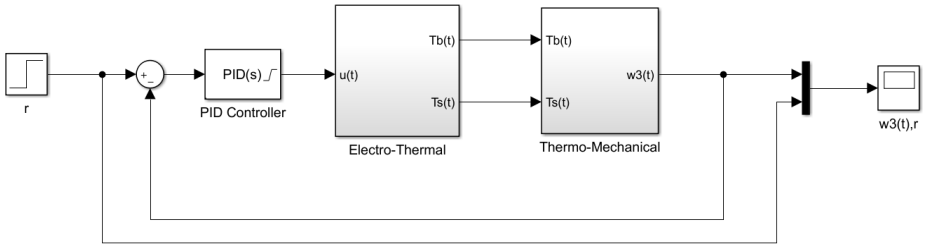

Figure 29: SIMULINK model with conventional PID controller.

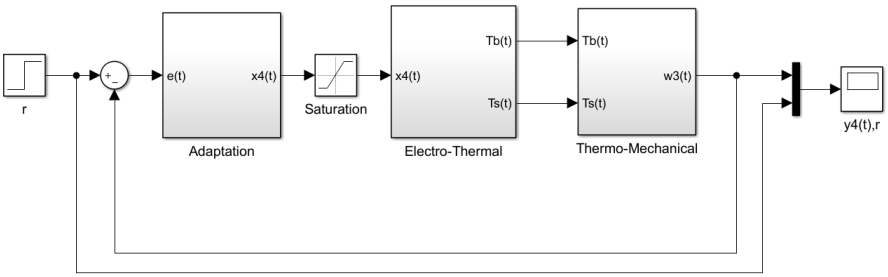

Figure 30: SIMULINK model with adaptive PID controller.

9.3.4. Comparison of the results obtained from the closed-loop and the open-loop systems. As seen in Fig. (32a) and in Table 11, the rise times associated with the displacement transient responses have been improved significantly after employing both controllers. In addition, the steady-state errors are negligible for both control systems. The settling time for the adaptive control system has been improved by 29%. However, the settling time obtained by the conventional PID control system is worse than the open-loop settling time. Moreover, the overshoot exhibited by the conventional PID control system is higher than that of the adaptive PID control system. The PID gains of both control systems can be re-tuned to get better transient responses, yet the limitation on the maximum voltage of 16 V will not be satisfied. On the other hand, the maximum energies during the transient time were found to be 2 mJ and 1.4 mJ for the conventional and the adaptive PID control systems, respectively which are less than the specified maximum energy. Furthermore, sum of squares of error, $\sum Error^2$, was calculated for the plots of Fig. (32b). As shown in Table 11, the adaptive PID control system results in a lower sum of squares of error compared to the conventional PID control system.

In sum, by using the conventional PID controller with the macromodel, the design requirements are not met. In contrast, the adaptive PID controller outperforms the conventional PID controller by meeting the design requirements.

Table 11: Comparison of the dynamic displacements for open-loop voltage of 6 V and closed-loop reference input of $r = 15.7\ \mu m$.

Characteristic	Units	Open-Loop	Conventional PID	Adapitve PID
Rise Time	ms	10.8	3.3	3.4
Settling Time	ms	19.2	20.2	13.7
Overshoot	$\%$	0	26.45	15.68
Steady-State Error	$\%$	-	0.01	0.05
Sum of Squares of Error	$(\mu m)^2$	-	5.72×10^5	5.05×10^5

9.4. Controller Design for the First-Order Model

In order to compare the results obtained by the closed-loop and the open-loop systems, the first-order model was first simulated in open-loop for the actuation voltages of 6 V and 12 V. The open-loop system is shown in Fig. (31).

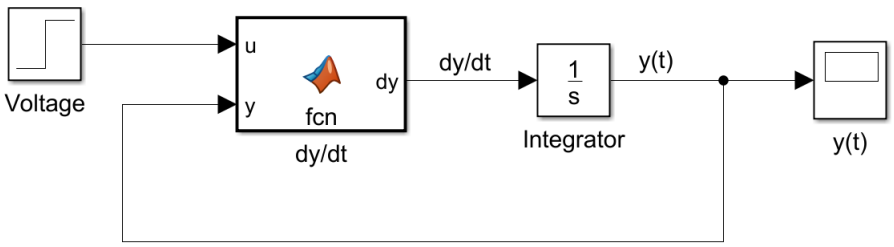

Figure 31: Open-loop system.

Based on the simulation results, the exhibited displacements upon applying 6 V and 12 V are 16.34 μm and 35.97 μm, respectively. The obtained displacements are then used as the reference inputs in the closed-loop systems. Moreover, the PID gains were tuned in such a way that the slew rates of the control signals remain within the limit of the amplifier.

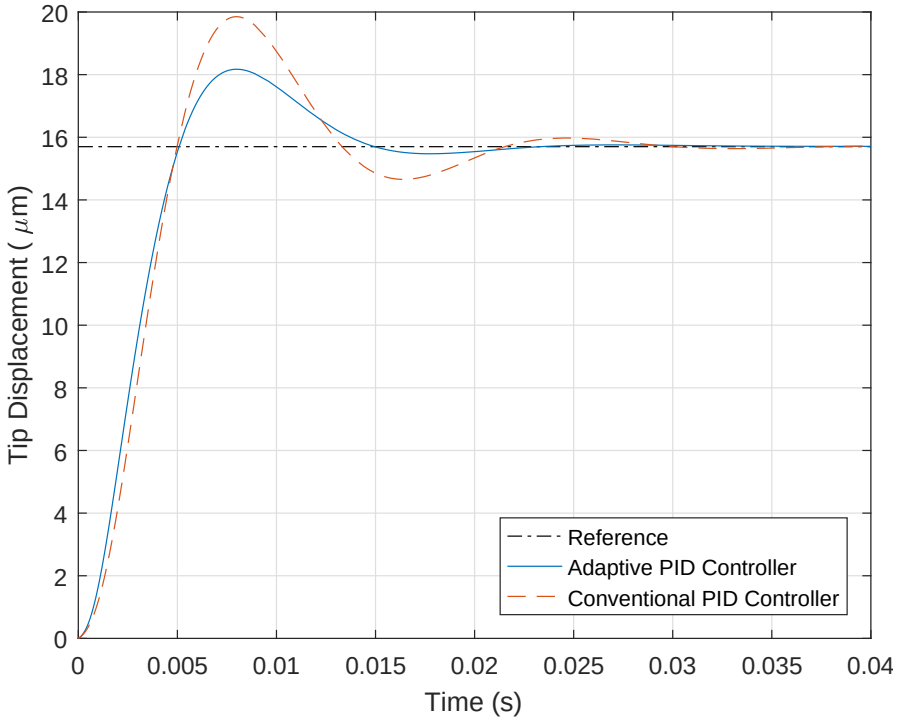

(a)

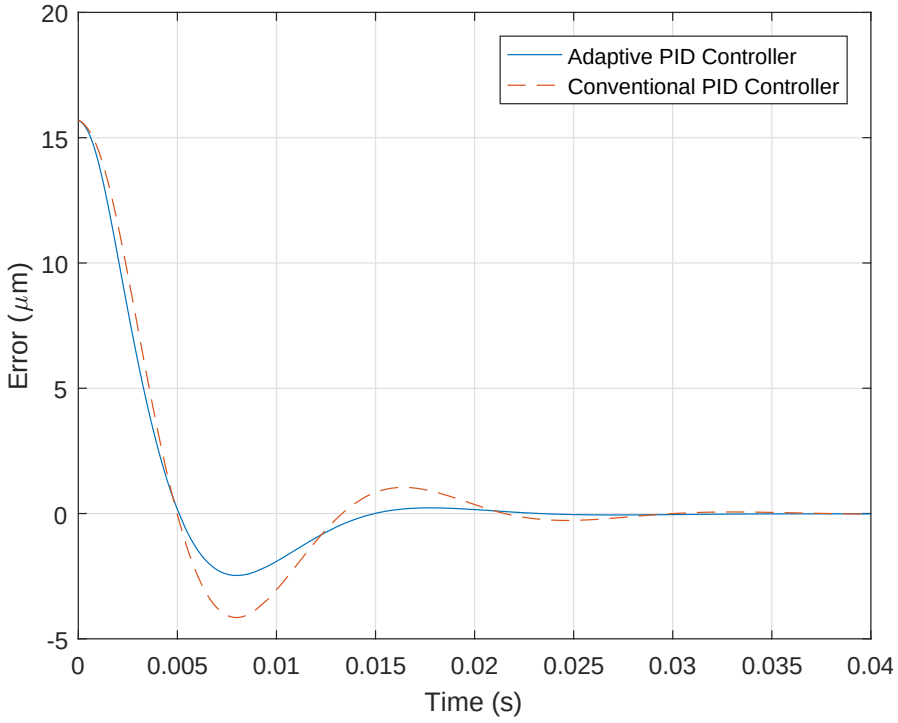

(b)

Figure 32: Simulation results obtained from the closed-loop system with the macro-model for $r = 15.7\ \mu m$ (a) actuator's tip displacement (b) error signal.

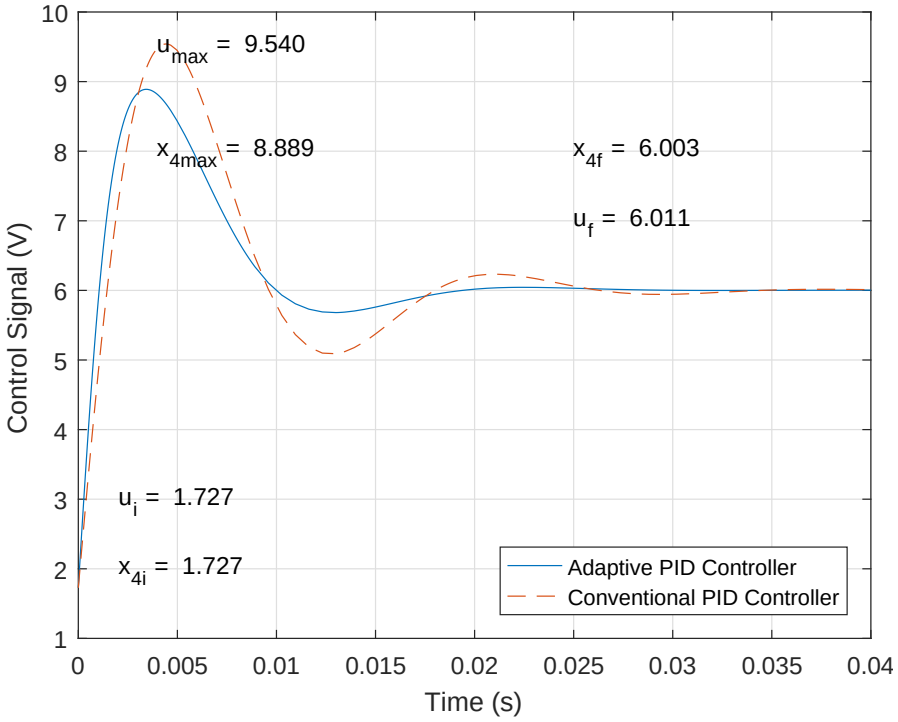

(a)

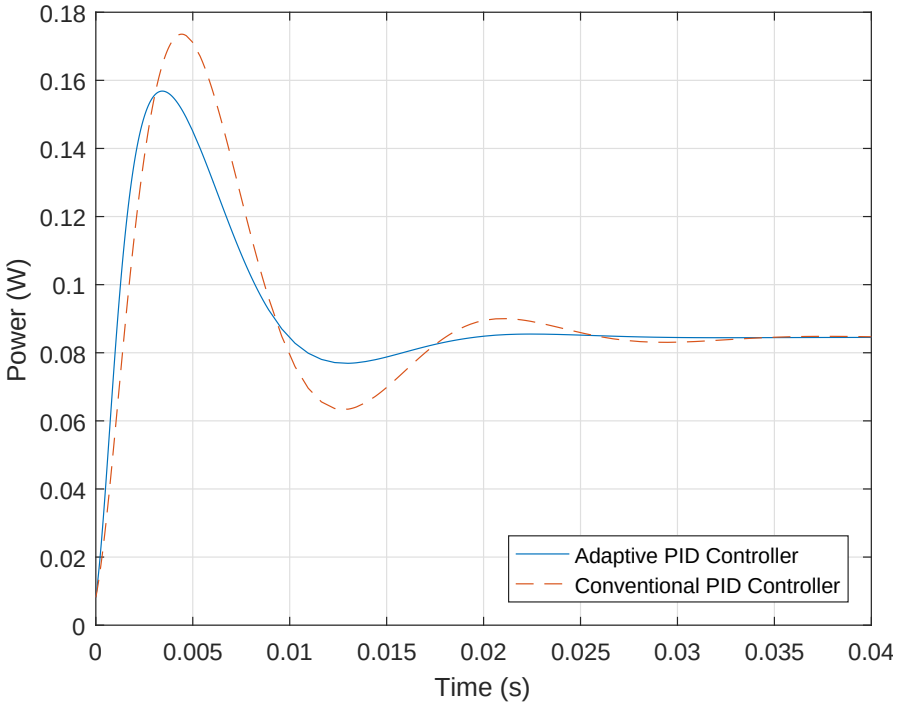

(b)

Figure 33: Simulation results obtained from the closed-loop system with the macro-model for $r = 15.7\ \mu m$ (a) control signal (b) consumed power.

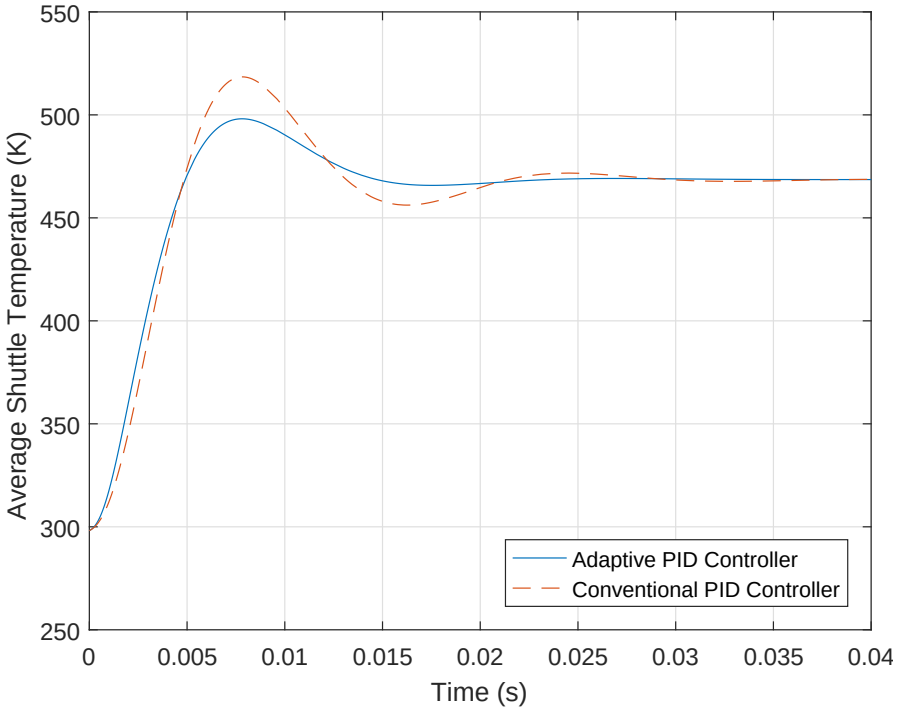

(a)

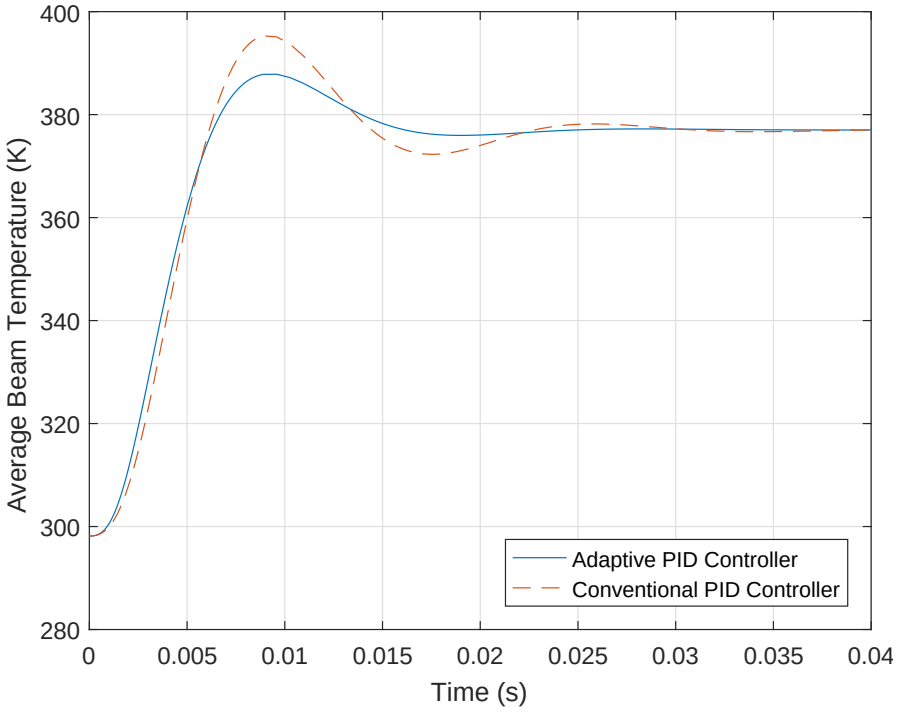

(b)

Figure 34: Simulation results obtained from the closed-loop system with the macro-model for $r = 15.7\ \mu m$ (a) average shuttle temperature (b) average beam temperature.

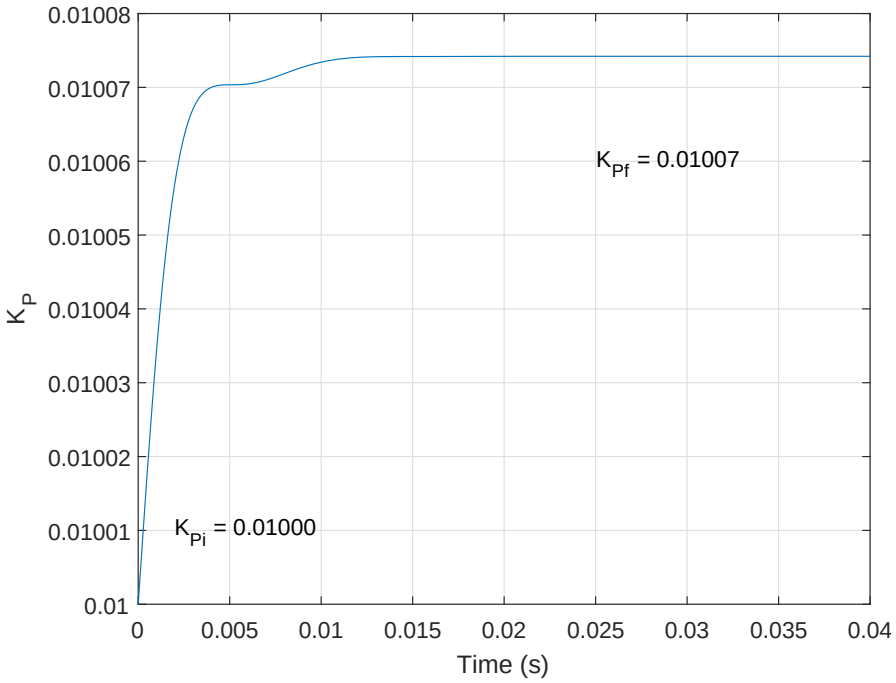

(a)

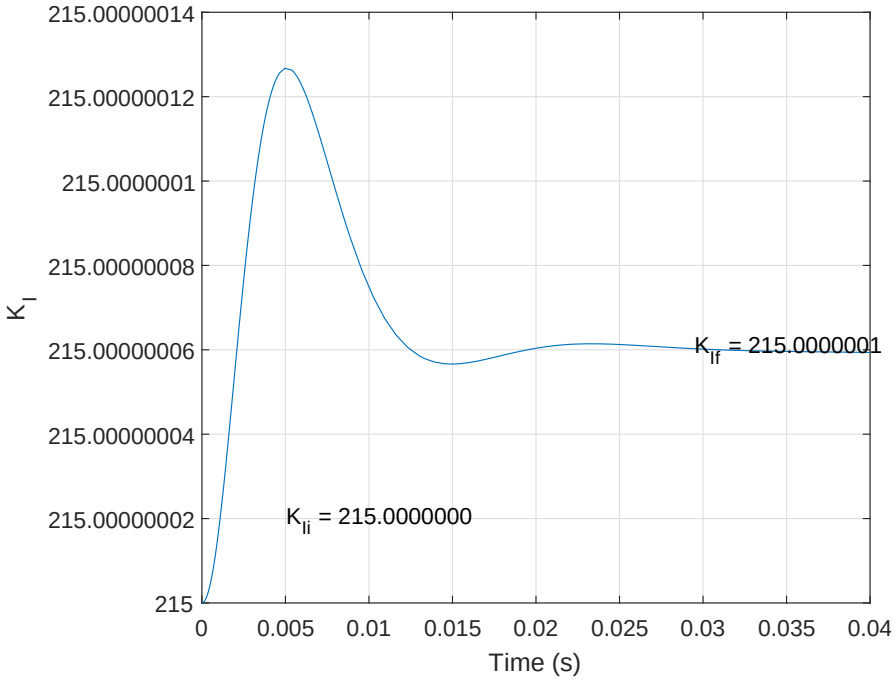

(b)

Figure 35: Adaptation of the gains obtained from the adaptive control system for $r = 15.7\ \mu m$ (a) K_P (b) K_I.

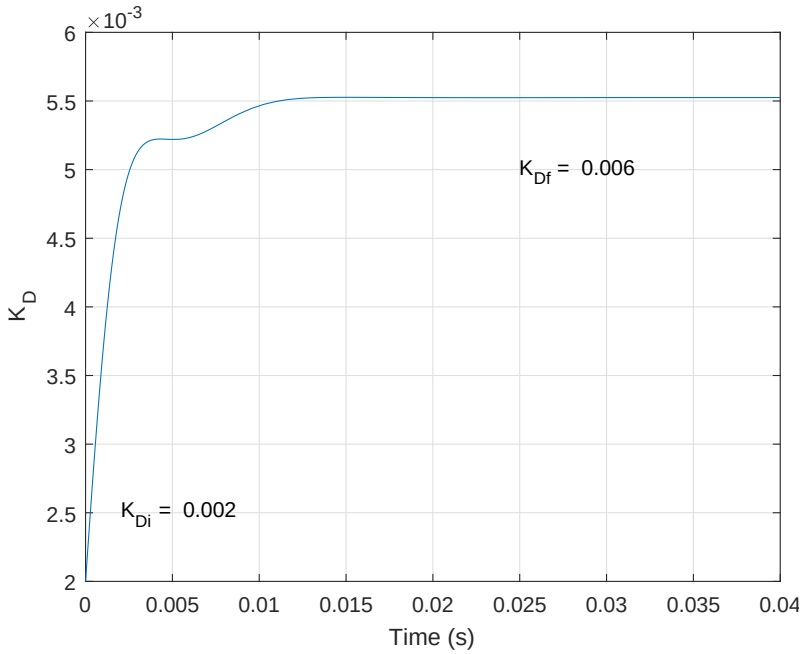

Figure 36: Adaptation of K_D obtained from the adaptive control system for $r = 15.7\ \mu m$

9.4.1. Conventional PID controller. A conventional PID controller was designed for the closed-loop system shown in Fig. (37) with the gains of $K_P = 0.8$, $K_I = 1000$, and $K_D = 3 \times 10^{-3}$. In addition, a low-pass filter with the coefficient $N = 50\ rad/s$ was used with the derivative action.

9.4.2. Adaptive PID controller. In order to investigate the feasibility of meeting the design requirements, the modified tuning algorithm presented in chapter 8 was employed. The adaptation coefficient was set to $\sigma = 3 \times 10^{-3}$. Moreover, the initial PID gains were set to $K_P = 0.8$, $K_I = 1000$, and $K_D = 3 \times 10^{-3}$ with $N = 50\ rad/s$, which are the gains used in the conventional PID controller. The SIMULINK model is depicted in Fig. (38).

9.4.3. Simulation results. The closed-loop systems shown in Figs. (37) and (38) were simulated in SIMULINK. The results consisting of the tip displacements, the control signals, and the error signals are shown in Fig. (39a)-(41b). In addition, the adaptations of the PID gains obtained from the adaptive control system are shown in Figs. (42a)-(44b). The initial and the final values of the gains and the control signals

are denoted by the subscripts i and f on the plots. Additionally, the subscripts max were used to show the peak values on the plots of the control signals.

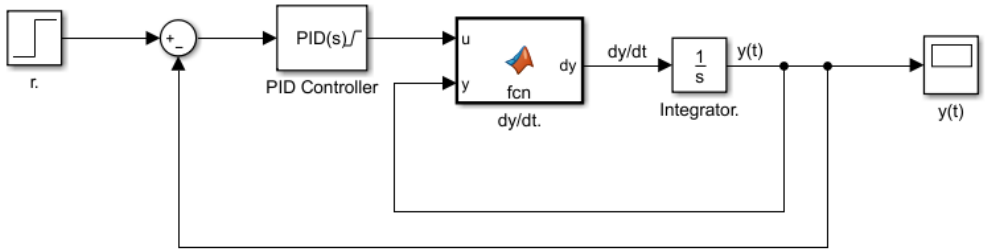

Figure 37: SIMULINK model with conventional PID controller.

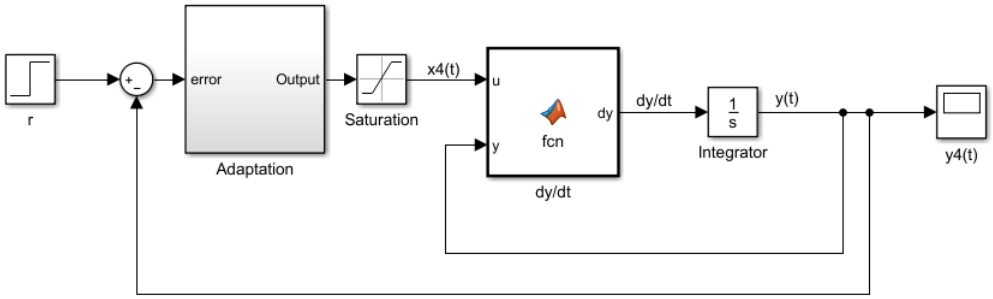

Figure 38: SIMULINK model with adaptive PID controller.

9.4.4. Comparison of the simulation results obtained from the closed-loop systems and the open-loop system. As seen in Figs. (39a) and (39b) and in Tables 12 and 13, the rise times associated with the displacement transient responses have been improved significantly after employing the conventional and the adaptive PID controllers. In addition, the steady-state errors are negligible for both reference inputs. The settling times for the adaptive control system have been improved by more than 70%. However, the settling times obtained by the conventional PID control system are higher than those obtained by the adaptive control system. In addition, the overshoots exhibited by the adaptive control system are lower than those of the conventional PID control system. The PID gains of both control systems can be re-tuned to get better transient responses, yet the limitation on the slew rate of the amplifier will not be satisfied. Fur-

thermore, sum of squares of error, $\sum Error^2$, was calculated for the plots of Figs. (41a) and (41b). As shown in Tables 12 and 13, the adaptive PID control system results in a lower sum of squares of error compared to the conventional PID control system.
In sum, by using the conventional and the adaptive PID controllers with the first-order model, the design requirements are met.

Table 12: Comparison of the displacement transient responses for open-loop input voltage of 6 V and closed-loop reference input of $r = 16.34\ \mu m$.

Characteristic	Units	Open-Loop	Conventional PID	Adaptive PID
Rise Time	ms	12.4	1.5	1.3
Settling Time	ms	22.0	9.0	6.2
Overshoot	$\%$	0	22.15	9.42
Steady-State Error	$\%$	-	0.00	0.03
Sum of Squares of Error	$(\mu m)^2$	-	2.69×10^3	2.49×10^3

Table 13: Comparison of the displacement transient responses for open-loop input voltage of 12 V and closed-loop reference input of $r = 35.97\ \mu m$.

Characteristic	Units	Open-Loop	Conventional PID	Adaptive PID
Rise Time	ms	11.5	1.3	1.1
Settling Time	ms	20.5	5.8	2.7
Overshoot	$\%$	0	5.22	0.47
Steady-State Error	$\%$	-	0.01	0.03
Sum of Squares of Error	$(\mu m)^2$	-	1.47×10^4	1.31×10^4

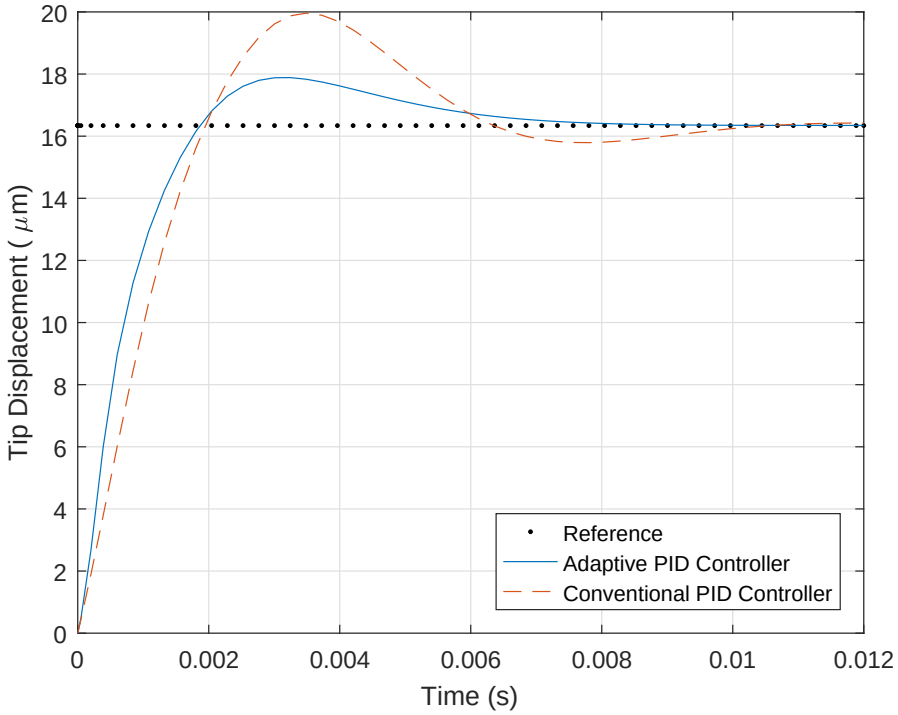

(a)

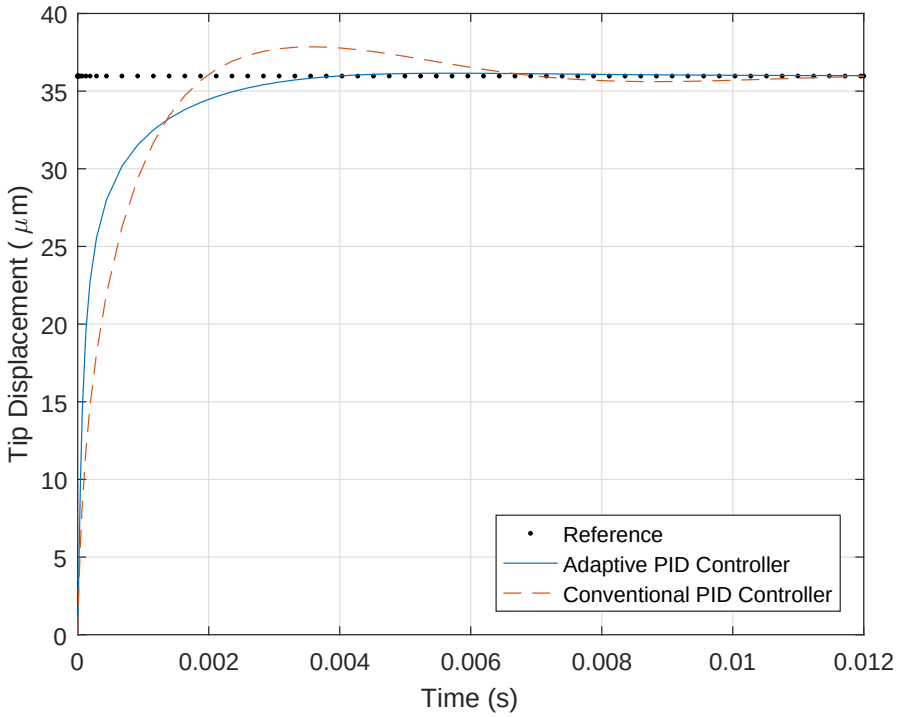

(b)

Figure 39: Closed-loop responses of the actuator's tip displacement obtained by conventional and adaptive PID controllers for (a) $r = 16.34\ \mu m$ (b) $r = 35.97\ \mu m$.

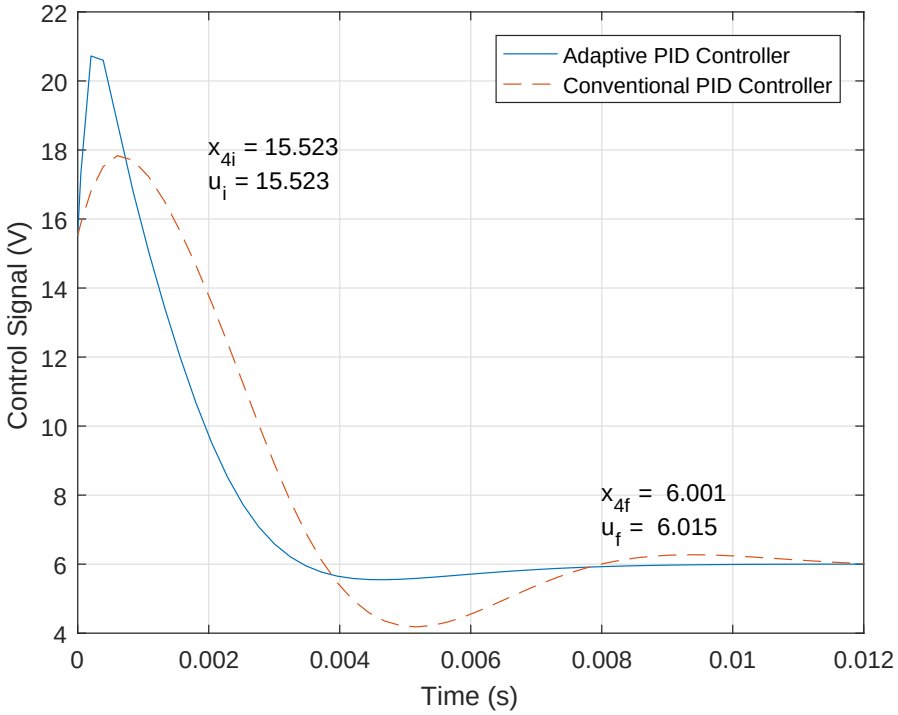

(a)

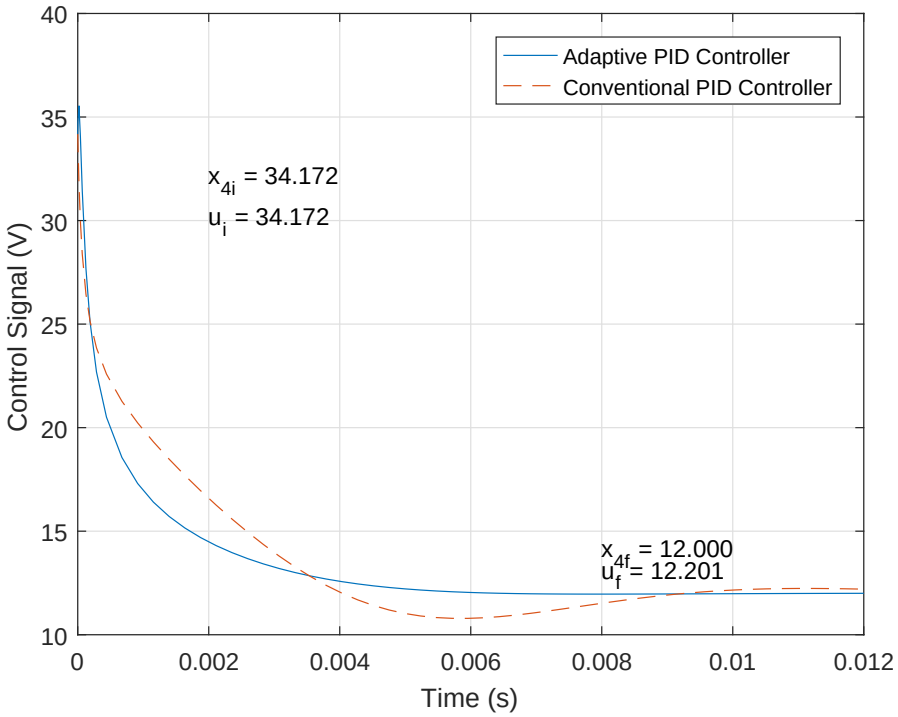

(b)

Figure 40: Control signals for (a) $r = 16.34\ \mu m$ (b) $r = 35.97\ \mu m$. In (b), both signals start at the same value, but the control signal corresponding to the adaptive PID controller reaches 35 V in a short period of time at the beginning.

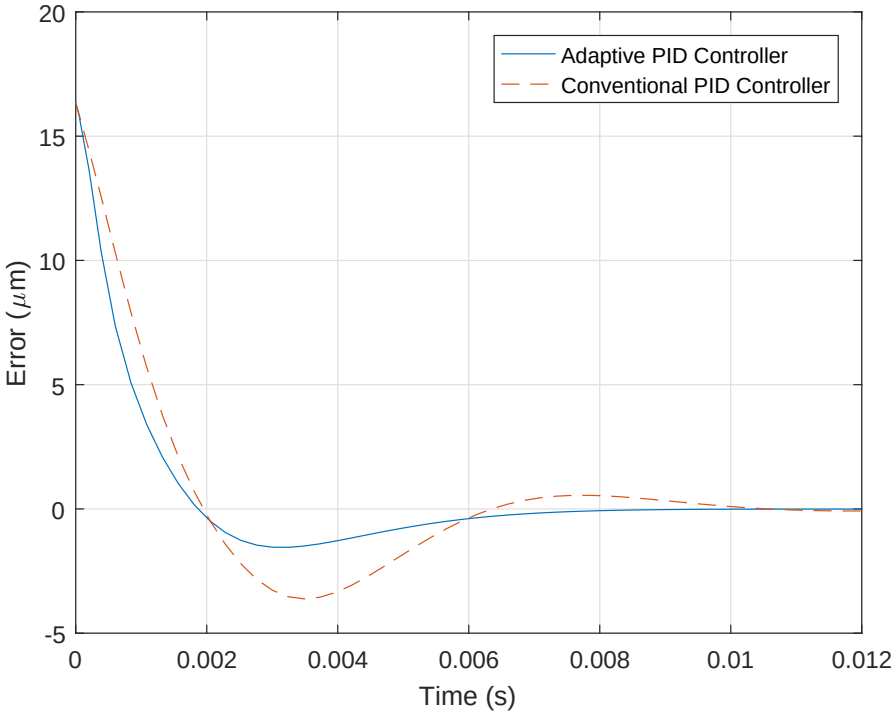

(a)

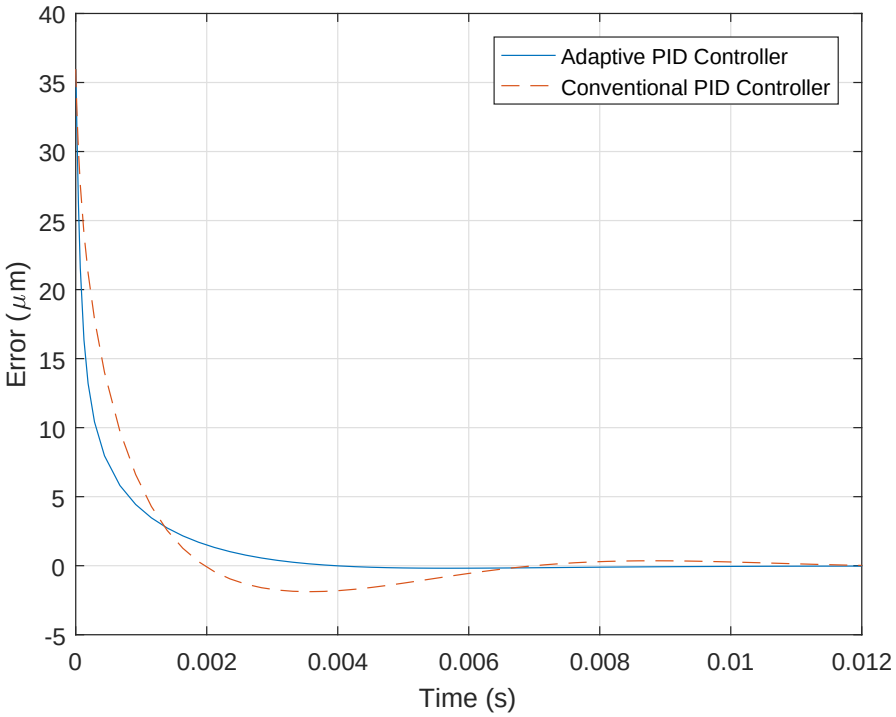

(b)

Figure 41: Error signals for (a) $r = 16.34\ \mu m$ (b) $r = 35.97\ \mu m$.

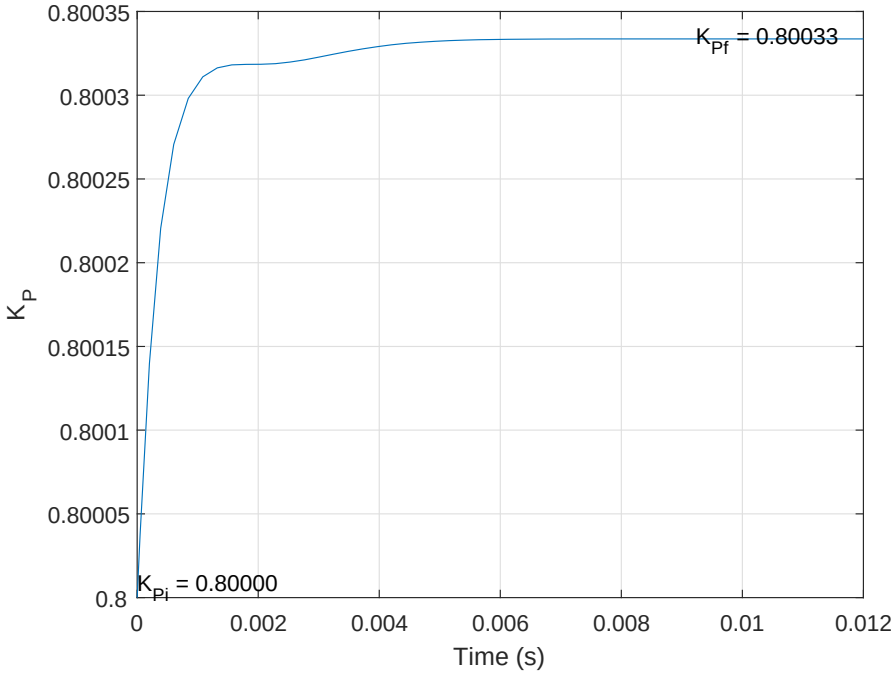

(a)

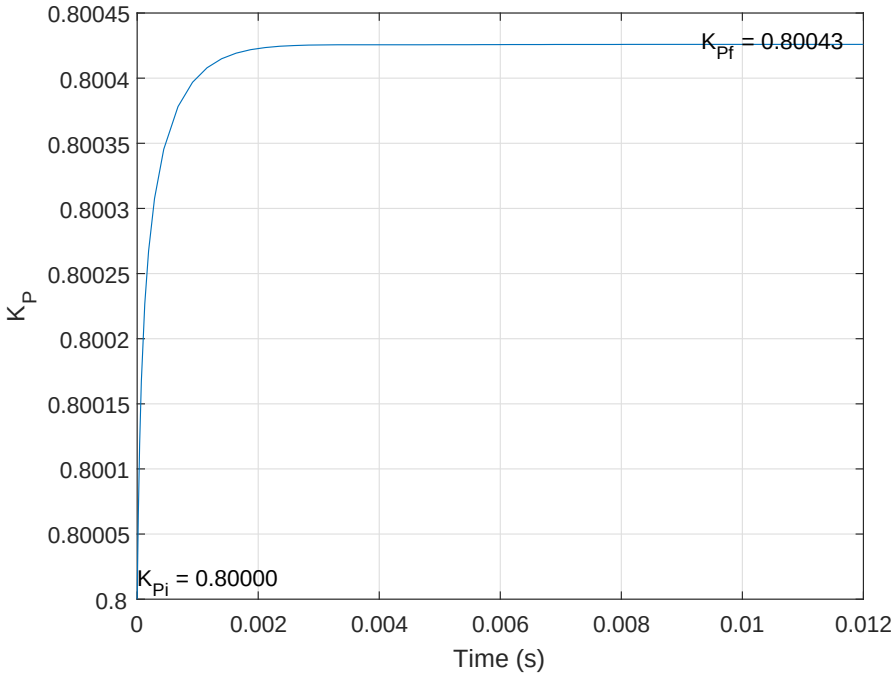

(b)

Figure 42: Adaptation of K_P for (a) $r = 16.34\ \mu m$ (b) $r = 35.97\ \mu m$.

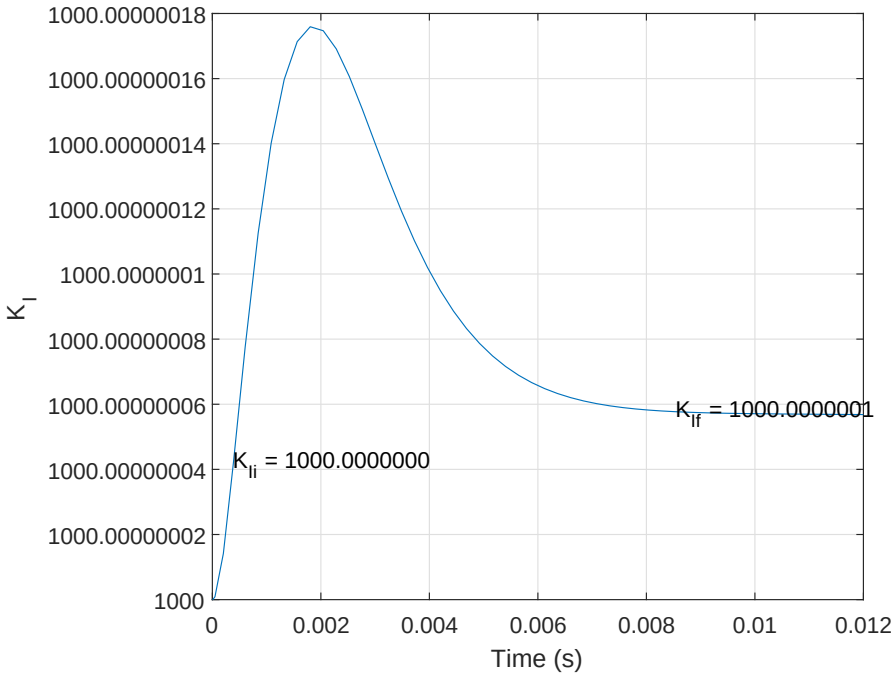

(a)

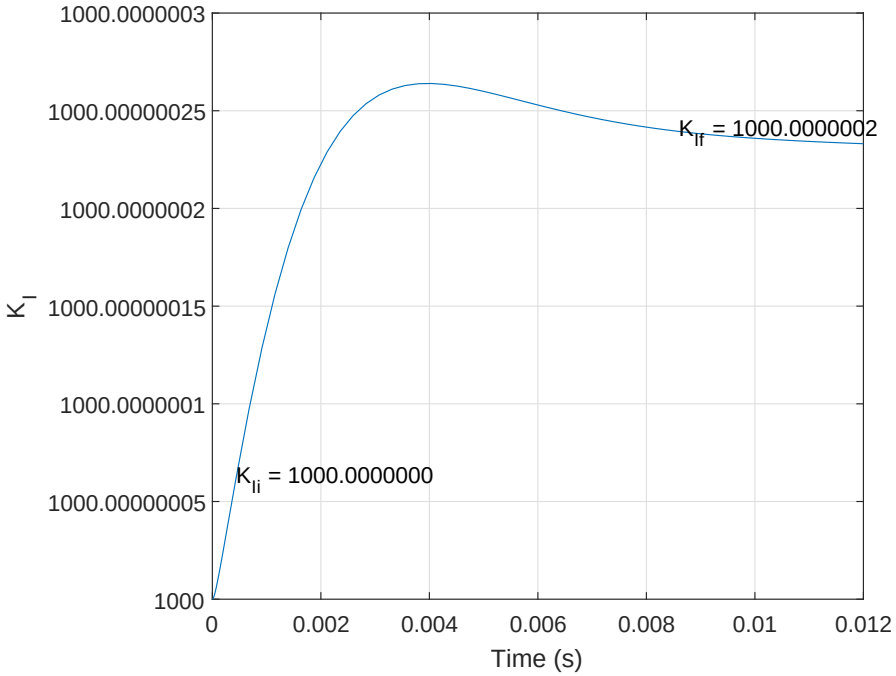

(b)

Figure 43: Adaptation of K_I for (a) $r = 16.34\ \mu m$ (b) $r = 35.97\ \mu m$.

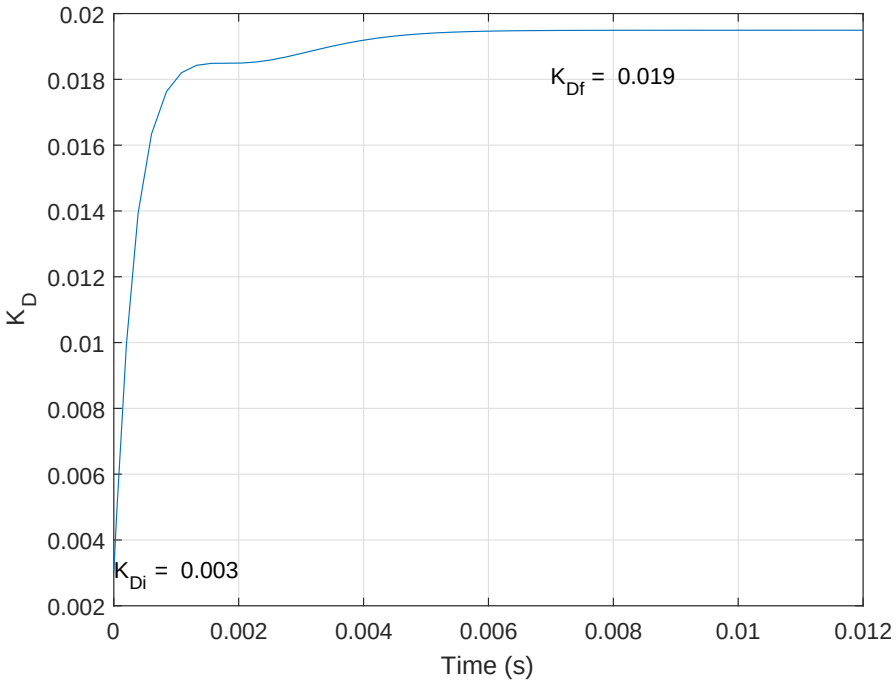

(a)

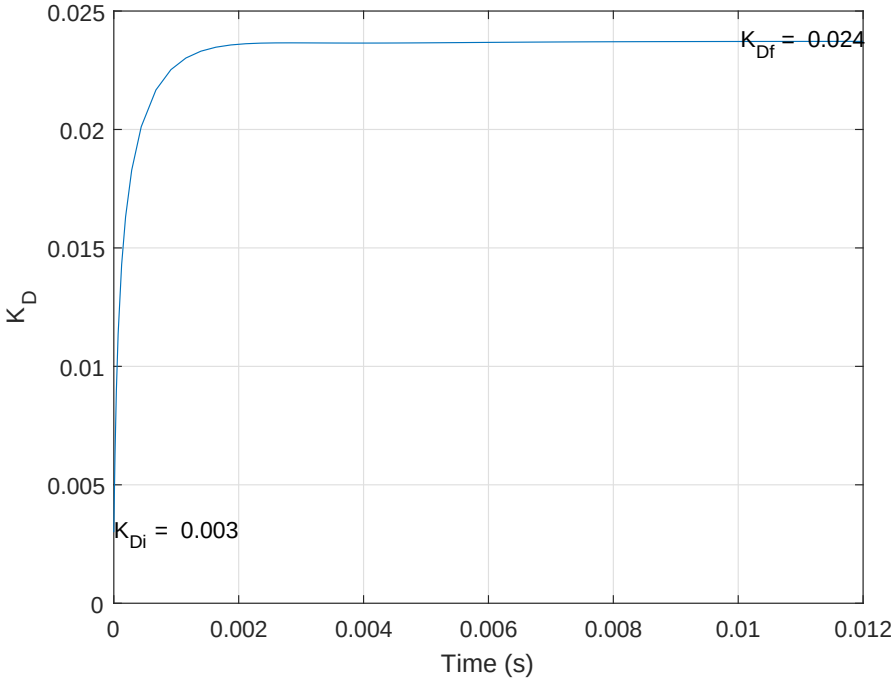

(b)

Figure 44: Adaptation of K_D for (a) $r = 16.34\ \mu m$ (b) $r = 35.97\ \mu m$.

9.4.5. Performance of the adaptive PID controller in response to square wave inputs. To further examine the performance of the closed-loop system composed of the first-order model and the adaptive PID controller, a square wave input with the amplitude of 35.97 μm was used as the reference to the control system. The obtained result is shown in Fig. (45).

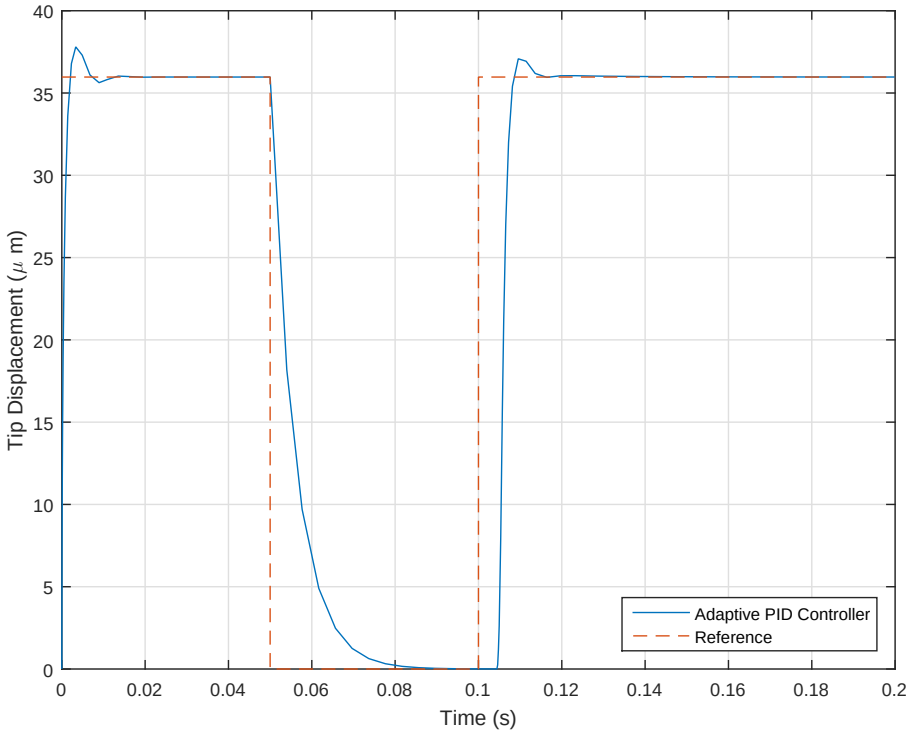

Figure 45: Simulated MEMS actuator's tip displacement in response to the square wave input. A 4.4 *ms* delay occurs in the response after $t = 0.1$ *s*.

As shown in the figure, after $t = 0.1$ *s*, a 4.4 *ms* delay appears in the response. We found out that the delay originates from the nonlinearity associated with the first-order model. In order to illustrate this, instead of using the first-order model, the transfer functions shown in Table 10 were used in the control system. For the adaptive control system with the transfer functions obtained from the voltage-displacement data corresponding to 6 *V* and 12 *V* actuation voltages, plots of the MEMS actuator's tip displacement and control signal are shown in Figs. (46a,47a) and (46b,47b), respectively. As can be seen in Figs. (46a) and (46b), there exists no delay in the response, and the exhibited overshoots decrease by time due to the adaptation of the gains.

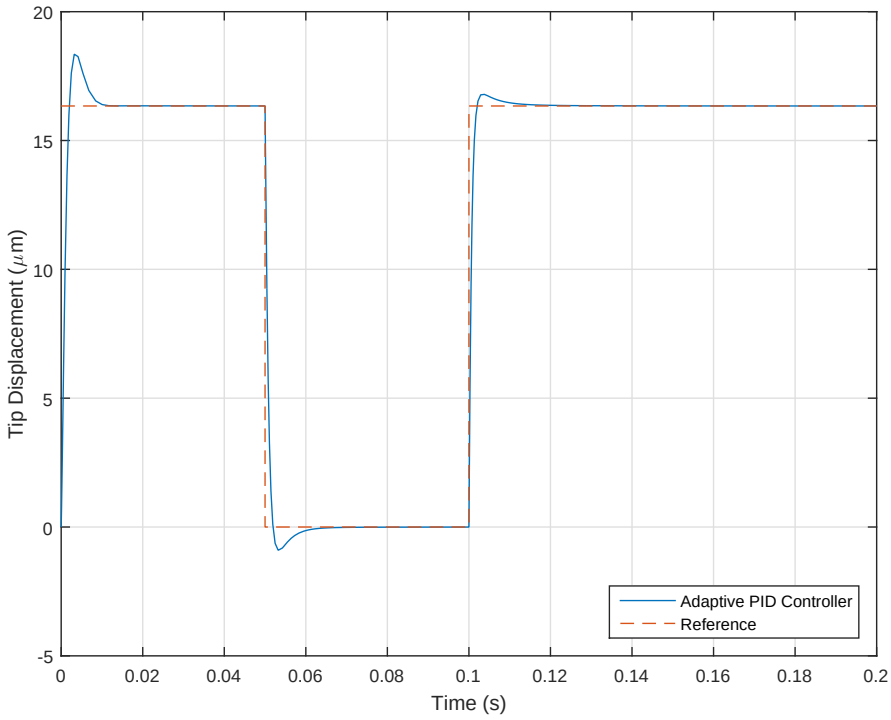

(a)

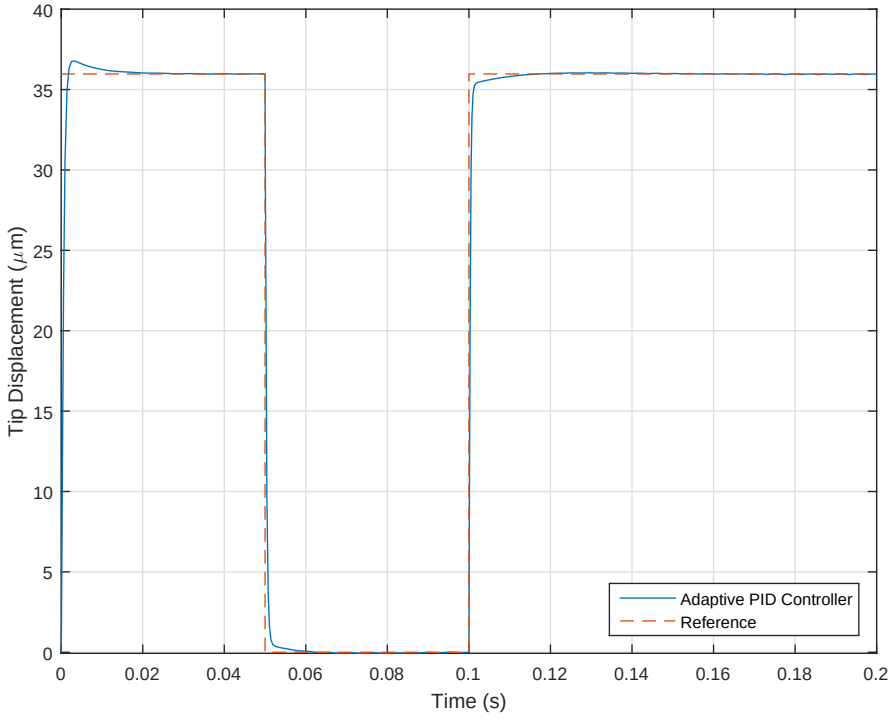

(b)

Figure 46: Closed-loop responses of the actuator's tip displacement obtained from the adaptive PID control systems composed of transfer functions and square wave inputs with the amplitudes of (a) 16.34 μm (b) 35.97 μm.

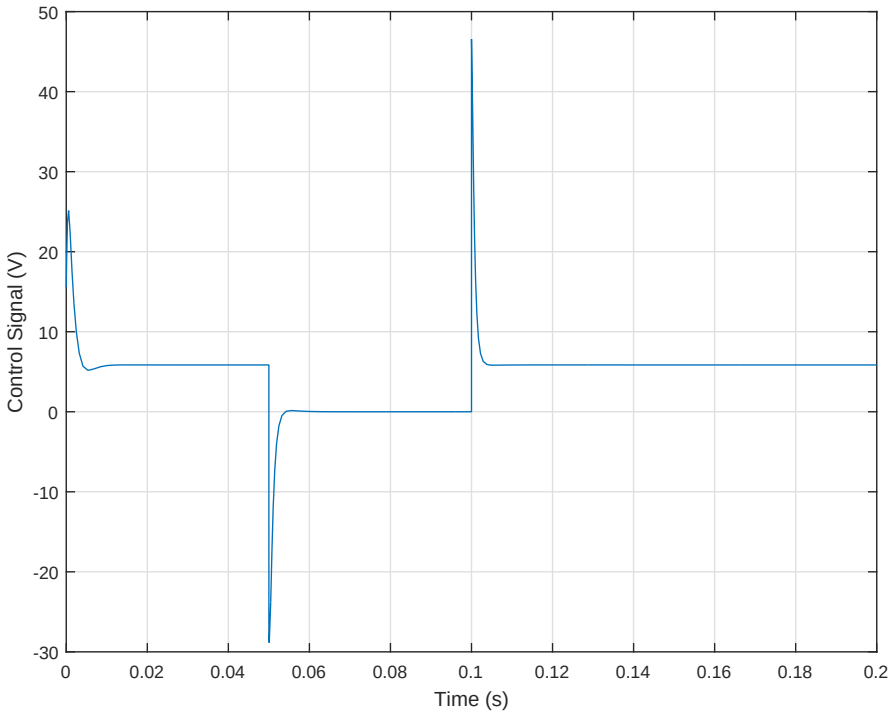

(a)

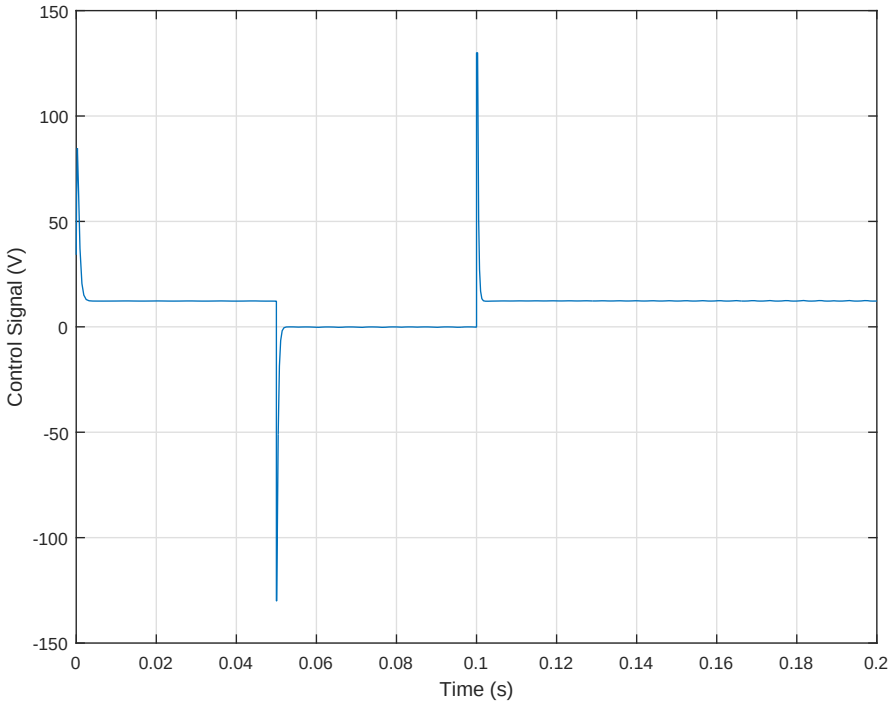

(b)

Figure 47: Control signals obtained from the adaptive PID control systems composed of transfer functions and square wave inputs with the amplitudes of (a) 16.34 μm (b) 35.97 μm.

9.5. Discussion

The following points summarize the observations made in the controller design process:

- Through different simulations, it was shown that the adaptive PID controllers yield better results in comparison with the conventional PID controllers.
- For the closed-loop system with the macromodel, the gains of the conventional PID controller and the adaptive PID controller were tuned in such a way that the control signals do not exceed 16 V. Therefore, only the results for $r = 15.77\ \mu m$ (corresponding to the open-loop voltage of 6 V) were shown, since for $r = 36.66\ \mu m$ (corresponding to the open-loop voltage of 12 V), the control signal is saturated at 16 V. In contrast, as this limitation did not apply to the closed-loop system with the first-order model, the controllers for the first-order model outperformed the controllers designed for the macromodel. As a result, two sets of simulations corresponding to two reference inputs were presented.
- If a temperature-dependent resistivity for the polysilicon layer is obtained through experimental determination of the temperature coefficient of the polysilicon resistance (TCR), the macromodel will be improved significantly and the controllers will be enhanced. This also enables the designer to quantify the energy at higher voltages, so that the actuator does not face plastic deformation. However, quantification of energy cannot be accomplished in the first-order model by using this method, as the first-order model deals with the voltage-displacement relation, while in the proposed method, temperature is required at each voltage to find the polysilicon resistance through which power/energy can be calculated.
- To further study the performance of the adaptive PID controller, a square wave input was used as the reference to the adaptive control system with the first-order model. Due to the nonlinearity associated with the first-order model, a delay appeared in the tip displacement response of the MEMS actuator. It was shown that by using the transfer functions instead of the first-order model, the delay did not occur in the response.

Chapter 10: Conclusion and Future Work

This research focused on developing a model that accurately describes the transient and steady-state response of thermally driven MEMS actuators. Having such a model leads to understanding the device dynamic behavior as well as improving the transient response of the MEMS actuator. This work has proposed a nonlinear electo-thermo-mechanical macromodel by cascading nonlinear electro-thermal and thermo-mechanical macromodels. The electro-thermal macromodel was developed to model the dynamic thermal behavior of V-shaped thermal MEMS actuators using lumped modeling with circuit elements. In addition, the thermo-mechanical macromodel for dynamic buckling of V-shaped thermal MEMS actuators was developed by applying the Galerkin method. Although an analytical static model has been reported in the literature, the dynamic model of V-shaped thermal MEMS actuators is presented for the first time. The developed dynamic thermo-mechanical and electro-thermal macromodels are in good agreement with ANSYS simulations considering the difference in the computational cost incurred. The electro-thermo-mechanical macromodel predicts the steady-state displacements of the actuator for different voltages with a maximum error of 9%. The error associated with the transient response exhibited by the electro-thermo-mechanical macromodel will decrease by increasing the number of segments in the electro-thermal macromodel.

Moreover, a first-order dynamic model, based on the ANSYS input voltage and output displacement data, was developed to find the displacement transient response of the MEMS actuator. The results obtained using the first-order model and the ANSYS model were in very good agreement.

In the last part of this thesis, conventional PID and adaptive PID controllers were designed and used with the macromodel and the first-order model to improve the displacement transient response of the MEMS actuator. Through simulations in SIMULINK, it was shown that the adaptive PID algorithm obtained by the theory of adaptive interaction outperforms the conventional PID controller.

10.1. Summary

The major contributions of this research work can be summarized as follows:

- The lumped modeling with circuit elements technique was used to model the thermal transient behavior of V-shaped thermal MEMS actuators. The lumped model presented includes temperature-dependent material properties leading to a nonlinear electro-thermal model. In addition, the new model accounts for convection and conduction losses to have a better representation of the thermal dissipation mechanism.
- The Galerkin method was applied to obtain a reduced order macromodel for the transversal displacement of V-shaped thermal MEMS actuators which are originally described by a nonlinear fourth order PDE. As a result, the PDE was reduced to a system of nonlinear second-order ordinary differential equations.
- The nonlinear electro-thermal and the nonlinear thermo-mechanical macromodels were combined to obtain a hybrid model for the transversal displacement of thermally driven MEMS actuators which accounts for electrical, thermal, and mechanical effects. The resulting dynamic model for the V-shaped thermal MEMS actuators is proposed for the first time to the author's best of knowledge.
- A first-order model, based on the dynamic voltage-displacement data obtained from ANSYS, was developed to obtain the displacement transient response of the MEMS actuator for different actuation voltages.
- Conventional and adaptive PID controllers were designed and the feedback control systems were simulated in SIMULINK for the purpose of improving the displacement transient response of the thermal MEMS actuator.

10.2. Future Work

It was shown that by using the first-order model in closed-loop form, the MEMS actuator's transient response was improved more in comparison with the transient response obtained from the macromodel in closed-loop. However, the proposed macromodel can be further improved by incorporating a temperature-dependent resistivity for the polysilicon layer. As a result, the controller design will be improved, and en-

ergy consumption can be calculated using the macromodel in contrast to the first-order model. Moreover, the macromodel paves the way for optimizing the MEMS actuator's geometry. In addition, the actual transient response of the actuator can be obtained using a high-speed camera for further validation. Finally, the designed adaptive PID controller can be tested on the actual thermal MEMS actuator, and its performance can be studied.

References

[1] E. T. Enikov, S. S. Kedar, and K. V. Lazarov, "Analytical model for analysis and design of V-shaped thermal microactuators," *J. Microelectromech. Syst.*, vol. 14, no. 4, pp. 788–798, Aug 2005.

[2] C. Lott, T. McLain, J. Harb, and L. Howell, "Modeling the thermal behavior of a surface-micromachined linear-displacement thermomechanical microactuator," *Sens. Actuators A, Phys.*, vol. 101, no. 12, pp. 239 – 250, Sep 2002.

[3] Z. Zhang, Y. Yu, X. Liu, and X. Zhang, "Dynamic modelling and analysis of V- and Z-shaped electrothermal microactuators," *Microsyst. Technol.*, pp. 1–15, Nov 2016.

[4] H. Hussein, A. Tahhan, P. L. Moal, G. Bourbon, Y. Haddab, and P. Lutz, "Dynamic electro-thermo-mechanical modelling of a U-shaped electro-thermal actuator," *J. Micromech. Microeng.*, vol. 26, no. 2, pp. 1–11, Jan 2016.

[5] B. Borovic, F. L. Lewis, D. Agonafer, E. S. Kolesar, M. M. Hossain, and D. O. Popa, "Method for determining a dynamical state-space model for control of thermal MEMS devices," *J. Microelectromech. Syst.*, vol. 14, no. 5, pp. 961–970, Oct 2005.

[6] E. S. Hung and S. D. Senturia, "Generating efficient dynamical models for micro-electromechanical systems from a few finite-element simulation runs," *J. Microelectromech. Syst.*, vol. 8, no. 3, pp. 280–289, Sep 1999.

[7] A. Ferreira and S. S. Aphale, "A survey of modeling and control techniques for micro- and nanoelectromechanical systems," *IEEE Trans. Syst. Man Cybern. C, Appl. Rev.*, vol. 41, no. 3, pp. 350–364, May 2011.

[8] Y.-J. Yang, S.-Y. Cheng, and K.-Y. Shen, "Macromodeling of coupled-domain MEMS devices with electrostatic and electrothermal effects," *J. Micromech. Microeng.*, vol. 14, no. 8, p. 1190, Jun 2004.

[9] S. Pal and H. Xie, "A parametric dynamic compact thermal model of an electrothermally actuated micromirror," *J. Micromech. Microeng.*, vol. 19, no. 6, pp. 1–10, May 2009.

[10] S. D. Senturia, *Microsystem Design*. Norwell, MA, USA: Kluwer Academic Publishers, 2001.

[11] S. T. Todd and H. Xie, "An electrothermomechanical lumped element model of an electrothermal bimorph actuator," *J. Microelectromech. Syst.*, vol. 17, no. 1, pp. 213–225, Feb 2008.

[12] R. K. Messenger, T. W. McLain, and L. L. Howell, "Piezoresistive feedback for improving transient response of MEMS thermal actuators," *Proc. SPIE*, vol. 6174, pp. 617 408–617 408–12, Feb 2006.

[13] S. Vamegh E., R. Dhaouadi, and M. Bakri-Kassem, "Hybrid dynamic modeling of V-shaped thermal micro-actuators," in *2016 17th International Conference on Thermal, Mechanical and Multi-Physics Simulation and Experiments in Microelectronics and Microsystems (EuroSimE)*, Montpellier, France, April 2016, pp. 1–4.

[14] R. K. Messenger, T. W. McLain, and L. L. Howell, "Improved nanopositioning resolution through piezoresistive feedback control of a MEMS thermal actuator," in *ASME 2005 International Mechanical Engineering Congress and Exposition*, Orlando, FL, USA, 2005, pp. 1327–1334.

[15] R. K. Messenger, Q. T. Aten, T. W. McLain, and L. L. Howell, "Piezoresistive feedback control of a MEMS thermal actuator," *J. Microelectromech. Syst.*, vol. 18, no. 6, pp. 1267–1278, Dec 2009.

[16] Y. Zhu, A. Bazaei, S. O. R. Moheimani, and M. R. Yuce, "Design, modeling, and control of a micromachined nanopositioner with integrated electrothermal actuation and sensing," *J. Microelectromech. Syst.*, vol. 20, no. 3, pp. 711–719, June 2011.

[17] P. A. Ioannou and J. Sun, *Robust Adaptive Control*. Prentice Hall, Inc, 1996. [Online]. Available: http://www-bcf.usc.edu/~ioannou/RobustAdaptiveBook95pdf/Robust_Adaptive_Control.pdf [Accessed: 2017-05-07].

[18] K. S. Narendra and J. Balakrishnan, "Adaptive control using multiple models," *IEEE Trans. Autom. Control*, vol. 42, no. 2, pp. 171–187, Feb 1997.

[19] K. S. Narendra and A. M. Annaswamy, *Stable Adaptive Systems*. Upper Saddle River, NJ: Prentice-Hall, Inc., 1989.

[20] K. S. Narendra and K. Parthasarathy, "Identification and control of dynamical systems using neural networks," *IEEE Trans. Neural Netw.*, vol. 1, no. 1, pp. 4–27, Mar 1990.

[21] M. M. Polycarpou, "Stable adaptive neural control scheme for nonlinear systems," *IEEE Trans. Autom. Control*, vol. 41, no. 3, pp. 447–451, Mar 1996.

[22] S. Omatu, M. B. Khalid, and R. Yusof, *Neuro-control and its applications*. Springer Science & Business Media, 2012.

[23] L. X. Wang, "Stable adaptive fuzzy control of nonlinear systems," *IEEE Trans. Fuzzy Syst.*, vol. 1, no. 2, pp. 146–155, May 1993.

[24] H.-X. Li and S. Tong, "A hybrid adaptive fuzzy control for a class of nonlinear mimo systems," *IEEE Trans. Fuzzy Syst.*, vol. 11, no. 1, pp. 24–34, Feb 2003.

[25] F. Lin, R. D. Brandt, and G. Saikalis, "Self-tuning of PID controllers by adaptive interaction," in *Proceedings of the 2000 American Control Conference*, vol. 5, 2000, pp. 3676–3681.

[26] B. M. Badreddine and F. Lin, "Adaptive PID controller for stable/unstable linear and non-linear systems," in *Proceedings of the 2001 IEEE International Conference on Control Applications, 2001. (CCA '01)*, 2001, pp. 1031–1036.

[27] V. Kaajakari, *Practical MEMS*. Small Gear Pub., 2009.

[28] J. M. Haake and M. W. Beranek, "In package micro-aligner for fiber-optic packaging," in *Electronic Components amp; Technology Conference, 1998. 48th IEEE*, Seattle, WA, USA, May 1998, pp. 1446–1449.

[29] M. Baltzer, T. Kraus, and E. Obermeier, "A linear stepping actuator in surface micromachining technology for low voltages and large displacements," in *Solid State Sensors and Actuators, 1997. TRANSDUCERS '97 Chicago., 1997 International Conference on*, vol. 2, Chicago, IL, USA, Jun 1997, pp. 781–784 vol.2.

[30] J. H. Comtois, M. A. Michalicek, and C. C. Barron, "Characterization of electrothermal actuators and arrays fabricated in a four-level, planarized surface-micromachined polycrystalline silicon process," in *Solid State Sensors and Actuators, 1997. TRANSDUCERS '97 Chicago., 1997 International Conference on*, vol. 2, Chicago, IL, USA, Jun 1997, pp. 769–772 vol.2.

[31] A. Lal, "Silicon-based ultrasonic surgical actuators," in *Engineering in Medicine and Biology Society, 1998. Proceedings of the 20th Annual International Conference of the IEEE*, vol. 6, Hong Kong, China, Oct 1998, pp. 2785–2790 vol.6.

[32] W. C. Tang, T.-C. H. Nguyen, and R. T. Howe, "Micromechanics laterally driven polysilicon resonant microstructures," *Sens. Actuators*, vol. 20, no. 1, pp. 25 – 32, Nov 1989.

[33] A. Cao, J. B. Kim, T. Tsao, and L. Lin, "A bi-directional electrothermal electromagnetic actuator," in *Micro Electro Mechanical Systems, 2004. 17th IEEE International Conference on. (MEMS)*, Maastricht, Netherlands, 2004, pp. 450–453.

[34] M. Bakri-Kassem and R. R. Mansour, "High power latching RF MEMS switches," *IEEE Trans. Microw. Theory Tech.*, vol. 63, no. 1, pp. 222–232, Jan 2015.

[35] L. Que, J. S. Park, and Y. B. Gianchandani, "Bent-beam electro-thermal actuators for high force applications," in *Micro Electro Mechanical Systems, 1999. MEMS '99. Twelfth IEEE International Conference on*, Orlando, FL, USA, Jan 1999, pp. 31–36.

[36] W. Riethmuller and W. Benecke, "Thermally excited silicon microactuators," *IEEE Trans. Electron Devices*, vol. 35, no. 6, pp. 758–763, Jun 1988.

[37] R. D. Brandt and F. Lin, "Adaptive interaction and its application to neural networks," *Inform. Sci.*, vol. 121, no. 34, pp. 201 – 215, 1999.

[38] P. Cominos and N. Munro, "PID controllers: recent tuning methods and design to specification," *IEE Proceedings - Control Theory and Applications*, vol. 149, no. 1, pp. 46–53, Jan 2002.

[39] M. Bakri-Kassem and R. R. Mansour, "A novel latching RF MEMS SPST switch," in *Microwave Integrated Circuits Conference (EuMIC), 2012 7th European*, Amsterdam, Netherlands, Oct 2012, pp. 28–31.

[40] S. Vamegh Estahbanati, M. Bakri-Kassem, and R. Dhaouadi, "Modeling and characterization of thin film polysilicon in thermally driven MEMS actuators," in *2016 IEEE 59th International Midwest Symposium on Circuits and Systems (MWSCAS) (MWSCAS2016)*, Abu Dhabi, United Arab Emirates (UAE), Oct. 2016.

[41] D. Lide, *CRC Handbook of Chemistry and Physics, 84th Edition*, ser. CRC Handbook of Chemistry and Physics. Boca Raton: Taylor & Francis, 2003.

[42] Y. Touloukian, P. Liley, and S. Saxena, *Thermophysical Properties of Matter - The TPRC Data Series. Volume 3. Thermal Conductivity - Nonmetallic Liquids and Gases*. Defense Technical Information Center, 1970.

[43] National Physical Laboratory. (1999) Kaye and Laby tables of physical and chemical constants. [Online]. Available: http://www.kayelaby.npl.co.uk/ [Accessed: 2016-09-14].

[44] A. Atre, "Analysis of out-of-plane thermal microactuators," *J. Micromech. Microeng.*, vol. 16, no. 2, p. 205, Dec 2006.

[45] B. Lopez-Walle, M. Gauthier, and N. Chaillet, "Dynamic modelling for thermal micro-actuators using thermal networks," *Int. J. Therm. Sci.*, vol. 49, no. 11, pp. 2108 – 2116, Nov 2010.

[46] S. V. Estahbanati, R. Dhaouadi, and M. Bakri-Kassem, "Macromodeling of thermally driven V-shaped MEMS actuators," *Mechatronics*, to be published.

[47] R. Hussey and J. Wilson, *Advanced Technical Ceramics Directory and Databook*. Springer US, 2012.

[48] Massachusetts Institute of Technology. Material property databases. [Online]. Available: http://www.mit.edu/~6.777/matprops/matprops.htm [Accessed: 2016-03-28].

[49] Y. W. Kwon and H. Bang, *The Finite Element Method Using MATLAB*, 2nd ed. Boca Raton, FL, USA: CRC Press, Inc., 2000.

[50] I. Guwahati, *Finite Element Formulation for Beams: Galerkin's Method*, 2010. [Online]. Available: https://youtu.be/LaxkM1B3Lm4 [Accessed: 2016-3-5].

[51] L. Meirovitch, *Elements of vibration analysis*, 2nd ed. New York : McGraw-Hill, 1986.

[52] J. Luo, A. Flewitt, S. Spearing, N. Fleck, and W. Milne, "Young's modulus of electroplated Ni thin film for MEMS applications," *Mater. Lett.*, vol. 58, no. 1718, pp. 2306 – 2309, Jul 2004.

Appendix A: Simulation Results

The following plots show the variation of the temperature-dependent thermal resistances as a function of time at 6 V and 12 V obtained by the open-loop macromodel:

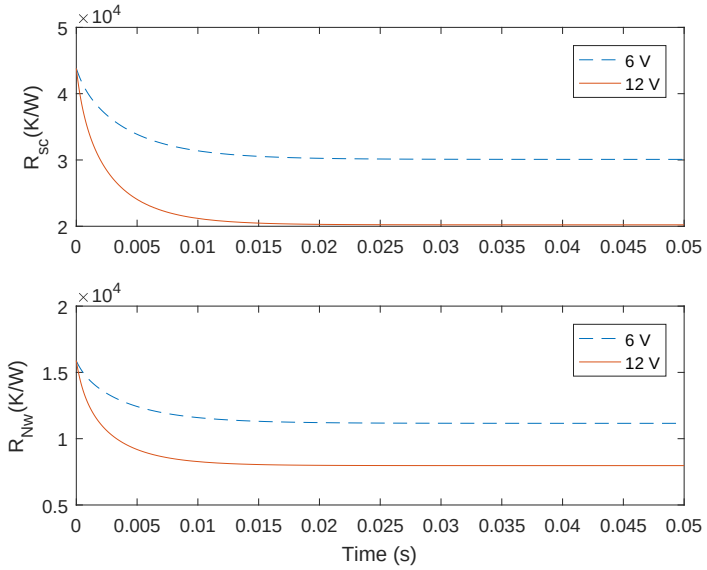

Figure 48: Variation of the temperature-dependent thermal resistances as a function of time in the shuttle and Nitride Volumes

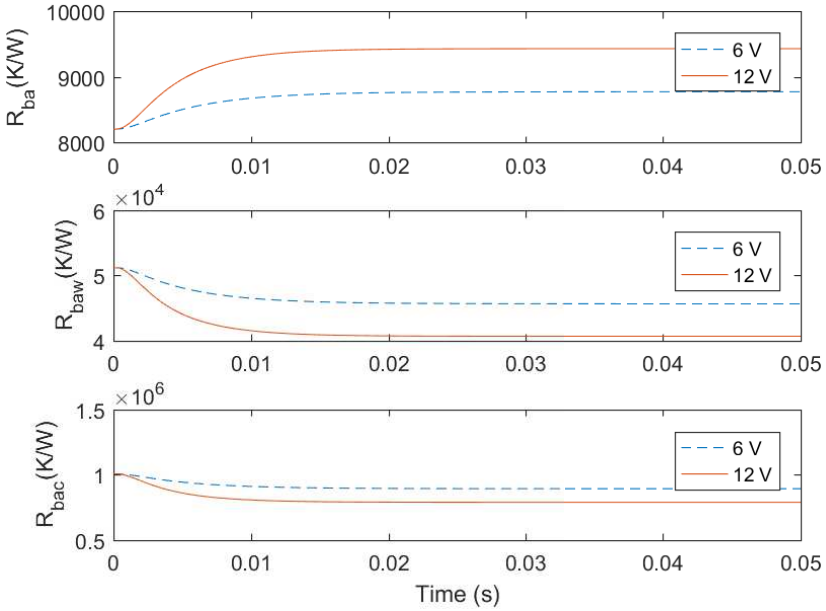

(a)

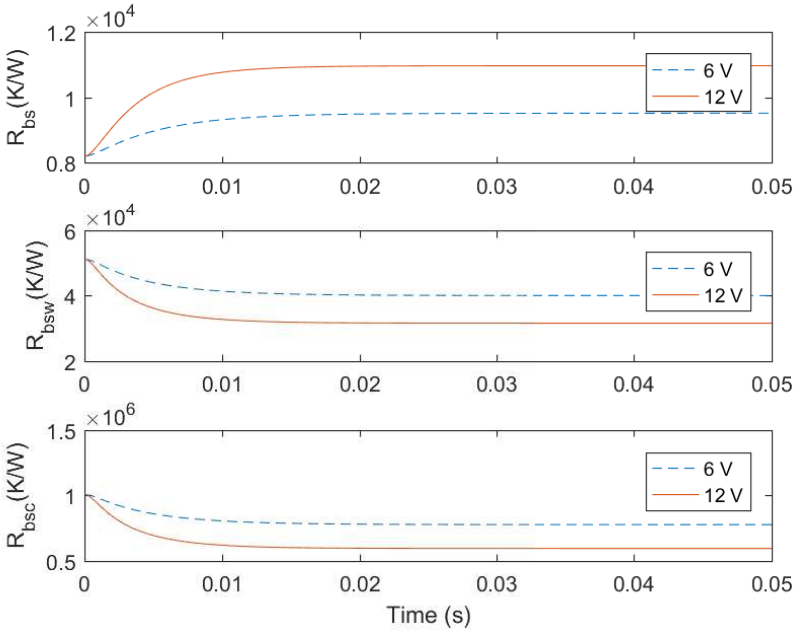

(b)

Figure 49: Variation of the temperature-dependent thermal resistances as a function of time in (a) Beam-Anchor volumes (b) Beam-Shuttle volumes

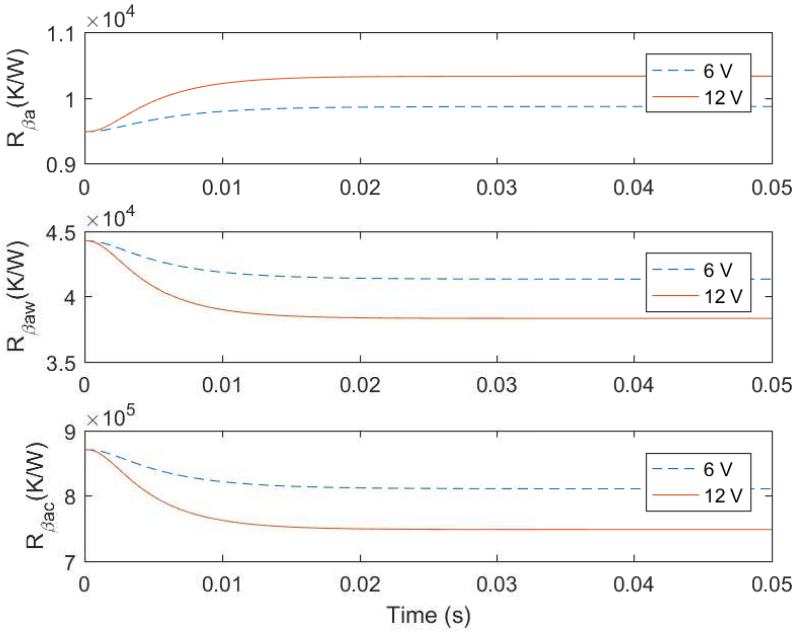

(a)

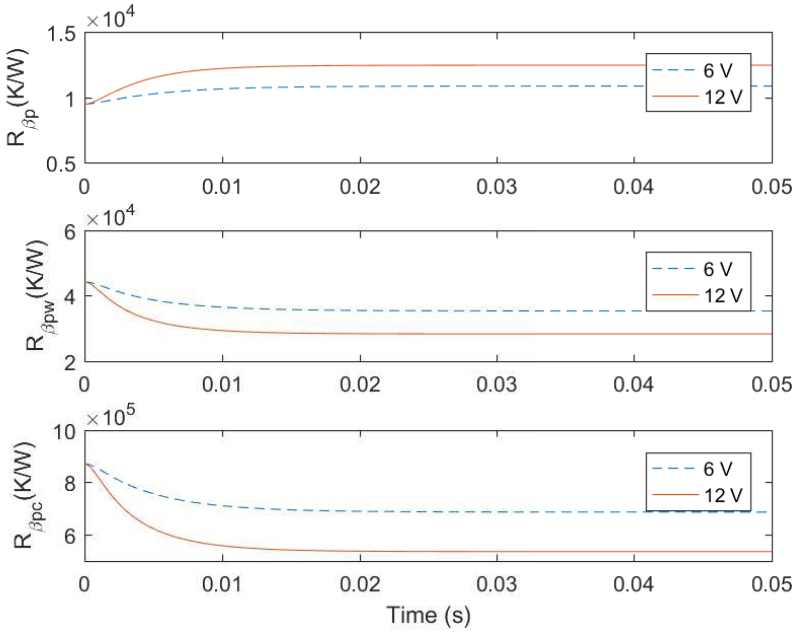

(b)

Figure 50: Variation of the temperature-dependent thermal resistances as a function of time in (a) DC Beam-Anchor volumes (b) DC Beam-Polysilicon volumes

Vita

Shahabeddin Vamegh Estahbanati was born in 1992, in Estahban, Iran. He received his B.Sc. degree in Electrical Engineering from the American University of Sharjah in 2014.

He joined the Electrical Engineering master's program in the American University of Sharjah as a graduate teaching assistant from February 2015 - May 2017. During his master's study, he published the following journal and conference papers:

- **S. Vamegh Estahbanati.**, R. Dhaouadi, and M. Bakri-Kassem, "Macromodeling of thermally driven V-shaped MEMS actuators," *Mechatronics*, to be published.
- **S. Vamegh Estahbanati**, M. Bakri-Kassem, and R. Dhaouadi, "Nonlinear modeling and characterization of a thermally driven MEMS actuator with a folded spring reference beam," *2017 18th International Conference on Thermal, Mechanical and Multi-Physics Simulation and Experiments in Microelectronics and Microsystems (EuroSimE)*, Dresden, Germany, Apr 2017.
- **S. Vamegh Estahbanati**, M. Bakri-Kassem, and R. Dhaouadi, "Modeling and characterization of thin film polysilicon in thermally driven MEMS actuators," *2016 IEEE 59th Midwest Symposium on Circuits and Systems (MWSCAS 2016), Abu Dhabi, United Arab Emirates, Oct 2016*.
- **S. Vamegh E.**, R. Dhaouadi, and M. Bakri-Kassem, "Hybrid dynamic modeling of V-shaped thermal micro-actuators," *2016 17th International Conference on Thermal, Mechanical and Multi-Physics Simulation and Experiments in Microelectronics and Microsystems (EuroSimE)*, Montpellier, France, Apr 2016.